University of Southampton

Faculty of Engineering & Physical Sciences

Optoelectronics Research Centre

All-Optical Signal Processes Enhanced by Multimode Nonlinearities

DOI: 10.5258/SOTON/T000

by

Omar Farooq Anjum

Thesis for the Degree of Doctor of Philosophy

October 8, 2020

University of Southampton

Abstract

Faculty of Engineering & Physical Sciences
Optoelectronics Research Centre

Doctor of Philosophy

All-Optical Signal Processes Enhanced by Multimode Nonlinearities

by Omar F. Anjum

Four-wave mixing (FWM) processes based on the third-order (Kerr) nonlinearity play a significant role in a range of classical and quantum optical phenomena, and in particular have been implemented in single mode waveguides for an array of applications. In these devices, FWM occurs between frequencies of light all of which propagate in the fundamental spatial mode. This thesis explores FWM in optical fibres when the interacting light fields are in different linearly polarized (LP) modes, and explores how this spatial degree of freedom can be used to advantage in the generation of particular FWM processes.

We initially restrict ourselves to linear propagation of the first higher-order mode (i.e. the LP_{11} mode) in a birefringent fibre, and use the state of polarization of input light to achieve control over the spatial intensity pattern at the fibre output.

Aspects relating to nonlinear inter-modal interactions come next. Polarization effects in inter-modal FWM are highly relevant in many applications. We will show that with two co-polarized pump waves in one spatial mode and the signal wave and the FWM generated idler field in another mode, FWM efficiency is independent of signal polarization. This polarization insensitivity is attributed to the fast evolution of random birefringence fluctuations of the fibre in combination with the input configuration employed. In FWM based parametric amplifiers, the bandwidth over which uniform gain is available is an important measure of performance. For broadband operation, our inter-modal FWM configuration relies on the frequency independence of differential group delay between the modes involved. We will report on the design, fabrication and experimental characterization of graded-index multimode fibres tailored to meet this requirement, and obtain a two-fold improvement in conversion efficiency bandwidth over previous results. Additionally, error-free and stable demodulation of an intensity modulated inter-modal FWM idler will be demonstrated. Finally, as an example of the flexibility of multimode operation, our scheme will be adapted to selectively enhance wavelength conversion of any one of multiple closely spaced signals. In the course of the above investigations, we will uncover important aspects governing the practicality of inter-modal FWM for a broad class of potential applications.

Contents

List of Figures

List of Tables

Declaration of Authorship

Omar Farooq Anjum.

All-Optical Signal Processes Enhanced by Multimode Nonlinearities.

I declare that this thesis and the work presented in it is my own and has been generated by me as the result of my own original research.

I confirm that:

1. This work was done wholly or mainly while in candidature for a research degree at this University;

2. Where any part of this thesis has previously been submitted for a degree or any other qualification at this University or any other institution, this has been clearly stated;

3. Where I have consulted the published work of others, this is always clearly attributed

4. Where I have quoted from the work of others, the source is always given. With the exception of such quotations, this thesis is entirely my own work;

5. I have acknowledged all main sources of help;

6. Where the thesis is based on work done by myself jointly with others, I have made clear exactly what was done by others and what I have contributed myself;

7. Parts of this work have been published, as cited in Section 1.2.

Acknowledgements

The proverb 'it takes a village to raise a child' can be easily adapted to the case of a graduate student, in whose development the supervisors play the role of the guardians and the rest of the 'village' comprises colleagues and collaborators. Hence, my first acknowledgements are due to my supervisors.

I must thank Francesca Parmigiani for first welcoming me to the ORC, for diligently providing the extensive support and training necessary for making a productive start on my doctoral program, for always being available to help, and for her courtesy. I must also thank Periklis Petropoulos for taking up primary supervision of my work after Francesca's departure from the ORC, and for his kindly and conscientious support of my work which led to the successful completion of my studies. I am also grateful to Yongmin Jung for his helpful attitude and expert guidance on experimental work.

Among my colleagues, I am especially obliged to Massimiliano Guasoni. Working with him has helped me tremendously in developing a better understanding of my work and this thesis has been enriched greatly by his insights and analyses. Peter Horak was a long-term collaborator and member of our weekly group meetings, and his input was also a source of learning for me.

Among my lab mates, I am very thankful to Kyle Bottrill for being a standby advisor on all lab related matters, for organising 'coffee hour' and for the pleasant table talk. I must also thank Iosif Demirtzioglou, Mohamed Ettabib, Hao Liu, Yang Hong, Elf and Cosimo Lacava for their colleagueship and company.

To the EPSRC and ORC, I am grateful for generous financial support.

Finally, I am afraid it will be impossible for me to convey my thanks adequately to my wife Rabia – or to repay her by kind words or actions – for the many good things her companionship has brought which I would struggle to capture in words here, and that is a debt I will carry forever.

List of Acronyms

AMF	advanced modulation format.
ASE	amplified spontaneous emission.
BER	bit error rate.
BERT	bit error rate test.
BS	Bragg scattering.
BSp	beamsplitter.
CE	conversion efficiency.
CW	continuous wave.
DMD	differential mode delay.
DSP	digital signal processing.
EC	elliptical core.
EDFA	erbium-doped fibre amplifier.
FMF	few-mode fibre.
FUT	fibre under test.
FWM	four-wave mixing.
GI	graded-index.
GVD	group velocity dispersion.
HNLF	highly nonlinear fibre.
HOM	higher-order mode.
IGV	inverse group velocity.
IM FWM	inter-modal four-wave mixing.
LCoS	liquid-crystal-on-silicon.
LP	linearly polarized.
MDM	mode division multiplexing.
MDMUX	mode demultiplexer.
MIMO	multiple-in multiple-out.
MMF	multimode fibre.

MZM	Mach-Zehnder modulator.
NLSE	nonlinear Schrödinger equation.
OOK	on/off keying.
OSNR	optical signal-to-noise ratio.
OSP	optical signal processing.
PBS	polarizing beamsplitter.
PC	phase conjugation.
PM	polarization maintaining.
PP	phase-plate.
RIGV	relative inverse group-velocity.
SBS	stimulated Brillouin scattering.
SDM	space division multiplexing.
SMF	single-mode fibre.
SOP	state of polarization.
SPM	self-phase modulation.
SRS	stimulated Raman scattering.
TOF	time-of-flight.
WDM	wavelength division multiplexing.
XPM	cross-phase modulation.
ZDW	zero dispersion wavelength.

Notation

Notation	Description	Units
$\beta_n^m(\omega_0)$	n-th derivative of the propagation constant of mode m evaluated at frequency ω_0	$\mathrm{ps}^n/\mathrm{km}$
$\alpha(z)$	Angle of randomly varying birefringence axes	rad
$L_{B(A_i,\,A_j)}$	Beat length for the mode pair $\{A_i,\, A_j\}$	m
$\omega_{\mathrm{BSb}}\,(\lambda_{\mathrm{BSb}})$	Blue-shifter Bragg scattering idler frequency (wavelength)	THz (nm)
n_{clad}	Cladding refractive index	
n_{core}	Core refractive index	
D	Dispersion parameter	$\mathrm{ps}/(\mathrm{nm\,km})$
A_{eff}	Effective area a, b, c, d	$\mu\mathrm{m}^2$
n_{eff}	Effective index	
Δn_{eff}	Effective index difference between x and y polarized waves	
$\Delta n_{A,B}$	Effective index difference between modes A and B	
f_{ab}	Equal to f_{aabb}	$1/\mu\mathrm{m}^2$
L_C	Fibre correlation length	m
L	Fibre length	m
k_0	Free-space wavenumber	$1/\mathrm{m}$
τ_{g}	Group delay	ns
β_2	Group velocity dispersion parameter	$\mathrm{ps}^2/\mathrm{km}$
$\mathrm{EH}_{\nu,\mu}, \mathrm{HE}_{\nu,\mu}$	Hybrid modes	
$\omega_i\,(\lambda_i)$	Idler frequency (wavelength)	THz (nm)
γ_{uv}	Intermodal nonlinear parameter	$1/(\mathrm{W\,km})$
β_1	Inverse group velocity	ps/km
n_2	Nonlinear index	m^2/W
γ	Nonlinear parameter	$1/(\mathrm{W\,km})$
$\mathbf{P}_{\mathrm{NL}}$	Nonlinear polarization	C/m^2

Notation	Description	Units
κ	Overall phase mismatch	1/m
f_{abcd}	Overlap integral over modes a, b, c, d	$1/\mu\text{m}^2$
$\omega_{\text{PC}}\,(\lambda_{\text{PC}})$	Phase conjugation idler frequency (wavelength)	THz (nm)
β	Propagation constant	1/m
$\omega_p\,(\lambda_p)$	Pump frequency (wavelength)	THz (nm)
$\Delta\omega_{pp}\,(\Delta\lambda_{pp})$	Pump-to-pump detuning	THz (nm)
$\Delta\omega_{ps}\,(\Delta\lambda_{ps})$	Pump-to-signal detuning	THz (nm)
$\omega_{\text{BSr}}\,(\lambda_{\text{BSr}})$	Red-shifter Bragg scattering idler frequency (wavelength)	THz (nm)
$\omega_s\,(\lambda_s)$	Signal frequency (wavelength)	THz (nm)
$\boldsymbol{\chi}^{(3)}$	Third-order optical nonlinearity	$(\text{m/V})^2$
$\text{TE}_{\nu,\mu}$	Transverse electric mode	
$\text{TM}_{\nu,\mu}$	Transverse magnetic mode	
$\Delta k, \Delta\beta$	Wavevector mismatch	1/m

Chapter 1

Introduction

1.1 Background and motivation

The primary motivation behind the development of optical fibres was to employ for telecommunications the high bandwidth made available by the laser, whose invention preceded closely. However, with the latter capable of producing high optical intensities and the former supporting tight confinement of light over long distances, the observation and study of a range of nonlinear optical effects in fibres occurred concurrently [1]–[3].

While their physical roots may differ, the term 'nonlinear' refers to the fact that the strength or efficiency with which they are generated varies nonlinearly with the amplitude of an applied optical field. For example, the phenomenon known as stimulated Brillouin scattering (SBS) is mediated by density fluctuations in a material, and the exponential growth factor of resulting backscattered light varies as the square of the amplitude of incident light. In contrast, the origin of the Kerr nonlinearity ($\boldsymbol{\chi}^{(3)}$) is electronic, and leads to an intensity dependent refractive index. Regardless of origin, from a telecommunications perspective, nonlinear effects are an impairment and can lead to limitations on the data carrying capacity of optical fibres [4], [5].

Historically, standards converged on the adoption of single-mode fibres (SMFs) for use in long-distance communications [6] because in SMFs, light propagation is supported on a single spatial channel (or *mode*), which is inherently more stable than propagation in multimode fibres (MMFs). Moreover, due to the unavailability of mature mode multiplexing technologies in the past, MMFs suffered from inter-modal dispersion which limited transmission

distance. Strides have been made in increasing the amount of information that can be sent through SMFs, which now comprise a significant proportion of installed fibre capacity. One of the means by which this has been done is the simultaneous transmission of multiple wavelength channels, or wavelength division multiplexing (WDM). Additionally, advanced modulation formats (AMFs) aim to utilize the available transmission spectrum as efficiently as possible by encoding multiple bits per symbol [7], [8]. In short, state of the art transmission systems today rely on advancements that harness the electromagnetic signal properties of wavelength, amplitude, phase and polarization.

Despite the above advancements, information theoretic arguments can be used to show that the (nonlinear) Kerr effect imposes fundamental limits on fibre transmission capacity, and that capacity gains from higher signal launch powers are ultimately diminished by nonlinear impairments [4], [5]. That is one reason why MMFs have caught the attention of the telecommunications community: with mature fibre fabrication capabilities and mode-multiplexing technologies now available, the potential for scaling up data-rates by utilizing the spatial dimension appears much more attractive than it was decades ago. This necessitates a thorough understanding of nonlinear effects in MMFs.

While fibre nonlinearities are a drawback in the context presented above, it was also recognized early on that they could be used to advantage in the accomplishment of a number of practical applications [9]–[11]. Nowadays for instance, the stimulated Raman effect is used to amplify the power of WDM signals which have been attenuated by propagation losses [12], understanding of the Kerr nonlinearity is used to realise compact and stable pulsed fibre lasers [13], and the interplay of nonlinear and dispersive effects is used to make broadband light sources for frequency combs [14]. The fast response of the $\boldsymbol{\chi}^{(3)}$ nonlinearity is also of particular interest in the area of optical signal processing (OSP). This refers to the ability to manipulate signals in the optical domain without the need for conversion of data to (and from) a digital format using electronic equipment. $\boldsymbol{\chi}^{(3)}$ mediated four-wave mixing (FWM) provides opportunities for wavelength conversion, amplification and phase-conjugation of signals all-optically [7]. In a FWM interaction, a set of input fields can physically conspire to exchange energy and produce a field at a different wavelength (typically called an idler) that can follow any rapid phase and amplitude fluctuations of an input signal. This attribute makes the idler transparent to the signal modulation format, and enables simultaneous

processing of multiple bits when AMFs are employed, thereby reducing latency. Consequently, much effort has gone into the study of FWM based OSP using optical fibres as well as silicon photonic chips [7], [15]–[22].

So far, the use of nonlinearities for the implementation of OSP functionalities has been largely focused on single-mode devices. The fact that MMFs could be used for independent spatial channel transmission (mode division multiplexing (MDM)) and for nonlinear applications was perceived and studied even decades ago [23], [24]. However, progress in this area was limited due to a couple of factors. To begin with, reliable and precise methods for the selective excitation of modes were not available. This problem was compounded by performance degradations imposed by significant inhomogeneities in the fibre structure. This meant that modes suffered from significant cross-talk, and could only remain uncoupled over short lengths of fibre. This hampered the practical implementation of MDM schemes. Early experiments utilizing multimode fibre nonlinearities such as in [1] were carried out using centimetre-length waveguides due to similar reasons. The above challenges have now been overcome to a significant degree due to technological advances. Low loss, low cross-talk fibres can now support propagation of individual spatial modes over lengths of the order of 100 km [25], and can be aided by digital signal processing (DSP) algorithms to further enhance their data carrying capacity [26]–[28]. A couple of efficient holographic methods have also become available for selective mode excitation. They are liquid-crystal-on-silicon (LCoS) spatial light modulators [29]–[33] and etched glass phase-plates [34]–[36]. More recently, 'multi-plane light conversion' mode (de)multiplexers based on these have also been demonstrated [37], [38]. Other methods such as photonic lanterns [39] and mode-selective waveguide couplers have also been considered [40].

Notwithstanding the above technological issues, modelling and experimenting with nonlinear effects in MMFs is inherently complex due to the combination of a multitude of nonlinear interactions, dispersive effects and sources of cross-talk that exist between modes in MMFs [41]–[44]. Consequently, much of the research in multi-mode nonlinear fibre optics continues to have an emphasis on the physical fundamentals of the interactions involved. However, the renewed interest in MDM stemming from reasons already mentioned, in conjunction with a better understanding of requirements for efficient FWM between various modes in MMFs (or inter-modal four-wave mixing (IM FWM)) have lent impetus to their study with an eye to their future use in OSP appli-

cations.

The fact that MMFs support multiple spatial modes over which data can be transmitted has already been stated. It turns out that this spatial degree of freedom can also provide flexibility over single-mode devices in the phase-matching of certain IM FWM interactions (phase-matching considerations govern the efficiency of FWM, as will be elaborated later). In addition to the OSP operations available in SMFs, IM FWM can also be used to transfer energy from one mode to another (i.e. mode conversion), which makes it a highly versatile tool for the manipulation of optical signals in higher-order fibre modes.

As examples of prior and ongoing work in this area, investigations of IM FWM have identified modal configurations which have the potential for broadband phase matching of waves with frequency separations greater than those typically observed in SMFs [45]–[49]. This motivates a deeper study of various input (mode and frequency) configurations for OSP applications in this thesis. The use of few-mode fibres (FMFs) for this purpose is of particular interest. FMFs support a relatively small number of modes (typically not much greater than ten, but a strict cutoff is not defined), and are thus a useful medium in the targeted exploration of nonlinear effects between specified modes.

1.2 Thesis structure

This thesis is organized as follows:

At the outset (Chapter 2), we investigate linear propagation of the first higher-order mode of a birefringent FMF. The choice of a birefringent fibre is significant, as it decouples both the spatial and the polarization components of the higher-order mode (HOM), thereby permitting individual access to all constituents of the *mode group*. Moreover, it allows greater robustness against physical disturbances to the fibre. We use this stability to study the spatial qualities of output light from this fibre. In the course of this investigation, we also establish the experimental scheme for efficient and selective excitation of the HOM(s) that will be used throughout the rest of the thesis. This is based on the use of holographic phase-plates (PPs) [35]. In addition to selective launching, we describe how to decompose the output in terms of the spatial modes. We observe that changing the polarization of the launch beam results in changes in spatial output, and the ability to affect maximum change in energy

from one spatial mode to the other is attained by having a specific orientation of the input PP. The manipulation of spatial output from MMFs has also been studied in non-birefringent fibres using multiple-in multiple-out (MIMO) measurements [50], [51], however, our method exploits the birefringence of the FMF to predict theoretically the nature of output observed. This chapter is based on a manuscript which is to be submitted for publication as a journal article [52].

In Chapter 3, we use the setup introduced above to study both intra- and inter-modal FWM interactions in a three-mode FMF. In intra-modal FWM, each mode is launched selectively and FWM occurs between light frequencies in that particular mode (this is qualitatively the same as FWM in a SMF). For IM FWM, our configuration involves three continuous wave (CW) inputs, with two of the input waves launched in the fundamental mode and one of them in a HOM. The efficiency of the resulting IM FWM, and its bandwidth is characterized. Here, FWM bandwidth refers to how far the input frequencies can be separated from each other until FWM efficiency is appreciably diminished. This is contrasted with a study of FWM in two different single-mode fibres, which serves as a prelude to IM FWM in this chapter. In particular, we discuss how phase matching differs between the two cases (intra- vs inter-modal FWM), and this involves a discussion of the dispersion properties of the modes involved. In intra-modal FWM, efficiency is found to depend on the absolute value of the dispersion parameter, whereas in the case of IM FWM it is the difference in dispersion between two modes that is significant. This means that the requirements for efficient nonlinear interaction in the two cases are fundamentally different.

In Chapter 4, a detailed look is taken at the role of polarization of the input waves on FWM efficiency and bandwidth. This is necessary because communications fibres in general do not preserve the polarization of electromagnetic signals. This is because there are fundamental reasons which prevent optical fibres from being perfectly isotropic, leading to residual birefringence, which in turn randomizes the state of polarization (SOP) of guided light even over short length scales. Therefore, any OSP that is performed midway through a communications link must not be sensitive to (signal) polarization. To this end, we demonstrate an IM FWM configuration that supports the polarization insensitive wavelength conversion of optical signals. An analysis of the IM FWM dynamics reveals that this polarization independence is the result of the

very residual birefringence that was mentioned earlier: the random nature of the fibre used in the wavelength converter blurs the distinction between idler gain for different SOPs of the signal. This chapter is based on our published work in [53].

It was mentioned that the phase matching condition for our IM FWM configuration differs fundamentally from that in conventional single-mode devices. In Chapter 5, we attempt to exploit this by experimenting with a set of MMFs that were fabricated for us by collaborators at Sumitomo Japan. The idea is to satisfy phase matching for a wide range of wavelengths by having different modes with the same dispersion. Consequently, a twofold improvement in bandwidth is achieved over previous results. However, closer analysis shows that the performance of devices based on this principle will be ultimately limited by fibre randomness, which results in fluctuations in dispersion characteristics (and hence phase matching) along the length of the fibre. This chapter is based on our journal publication in [54].

In Chapter 6, we demonstrate how to selectively enhance the wavelength conversion of (any) one signal out of a group of closely spaced signals such as might be encountered in a WDM link. This is an example where the inherent characteristics of phase matching in IM FWM help to attain functionality that would be significantly more cumbersome to implement in a single-mode device. In studying the dynamics of this method, we discover that mode-splitting between the spatial group of a HOM can complicate the analysis, and leads to polarization dependent gain profiles for the idler wave. Theoretical and experimental justification for our arguments is presented. In addition to presenting selective wavelength conversion, we demonstrate the performance of our wavelength converter when a data-modulated signal is used. Error free demodulation of the IM FWM idler corresponding to an intensity modulated signal is shown. This chapter is based on our published work in [55].

Chapter 2

Transverse field manipulation by polarization modulation in a birefringent few-mode fibre

We start this chapter with a section dedicated to the fundamentals of linear light propagation in (step-index) optical fibres. In it, we will first discuss some important background on the exact solutions to the propagation equations, and then describe a commonly used approximation of how light travels through an optical fibre: this is the weakly guiding approximation which results in the linearly polarized (LP) modes.

Moving on, we investigate the LP_{11} mode group in a birefringent FMF, and present some interesting results relating to the manipulation of its spatial output pattern. The orientation and polarization of the beam that is used to launch the LP_{11} mode are found to have a significant impact on the range of output intensity profiles that can be obtained. In particular we show how, by alternating the input polarization between two states, such a system can be used for all-optical switching of light between two receiving ports.

2.1 Fibre modes under the weakly guiding approximation

In this work, we will consider light propagation in multimode fibres in terms of their spatial mode groups under the weakly guiding approximation. We describe what that means in this section.

As in all areas of modern classical optics, the description of electromagnetic fields in waveguides depends on the solution of Maxwell's equations subject to some boundary conditions. In the case of a step-index fibre, the waveguide consists of a cylindrical core (typically made of silicate glasses for low-loss telecommunications) with refractive index n_{core} within a cladding of lower index n_{clad}. The index differential (Δn) enables guidance of light longitudinally along the fibre, a phenomenon that is known as total internal reflection.

Solving Maxwell's equations subject to the physical conditions imposed by the fibre parameters (such as refractive index profile, core diameter and geometry) results in expressions for the electric and magnetic field vectors $\mathbf{E} = (E_x, E_y, E_z)$ and $\mathbf{H} = (H_x, H_y, H_z)$ (respectively) that may be guided in the fibre core. For a given frequency of light ω, a mode can be specified by an expression of the form $\mathbf{E} = \mathbf{m}(\mathbf{r}_\perp) \exp i(\beta z - \omega t)$, where $\mathbf{r}_\perp = (x, y)$ and $\mathbf{m}$ is a three dimensional spatial vector [56]. Thus $\mathbf{E}$ consists of a z-propagating wave with transverse (or spatial) part $\mathbf{m}$ and a fast varying longitudinal oscillation characterized by the propagation constant β.[1] Modes with the same propagation constant are termed degenerate. The effective mode index is defined as $n_{\text{eff}} = \beta/k_0$ where k_0 is the (free-space) wavenumber corresponding to ω.

The exact calculation for the propagation constant(s) at a given frequency is done by solving the associated eigenvalue equation which results by solving Maxwell's equations [56]. For a mode to be guided, its propagation constant must be bounded by the relation $n_{\text{clad}} k_0 \leq \beta \leq n_{\text{core}} k_0$. This is due to physical considerations: values of β close to the lower bound (i.e. near cut-off) result in modes whose field energies travel mostly in the cladding region. The upper bound corresponds to modes whose energies are strongly confined in the core.

Detailed vectorial solutions for $\mathbf{E}$ (and $\mathbf{H}$) can be found. Among the modes are those that can be classified as $\text{TE}_{\nu,\mu}$ (transverse electric: $E_z = 0$) and $\text{TM}_{\nu,\mu}$ (transverse magnetic: $H_z = 0$), with ν, μ integers and $\nu = 0, \mu \geq 1$. The rest are classified as hybrid modes and are two-fold degenerate; they are abbreviated by $\text{EH}_{\nu,\mu}$ and $\text{HE}_{\nu,\mu}$ with $\nu, \mu \geq 1$ [56]. Therefore in general, all components of $\mathbf{E}$ may be non-zero. However, if the index difference Δn between the core and the cladding is assumed small (this is known as the weakly guiding approximation, and is generally realistic since $\Delta n \sim 10^{-4}$ to 10^{-3}

[1] An alternative way to visualise this is to think of a mode in the picture of ray optics, in which a mode is formed as a superposition of totally internally reflected plane waves inside the waveguide. See [57] for details.

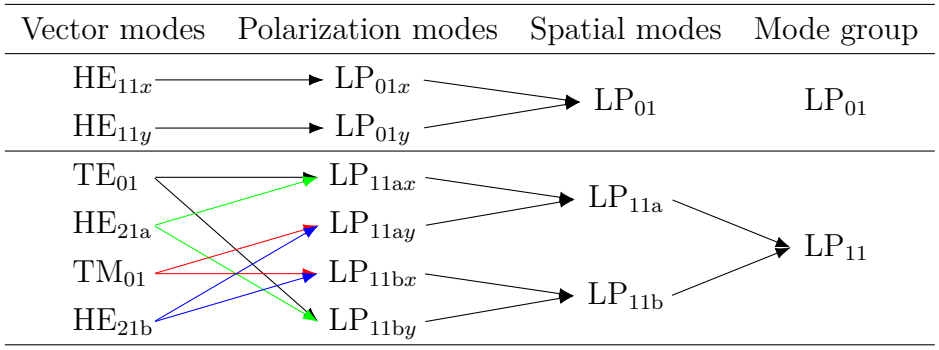

Table 2.1. Classification of modes in the exact case (first column) and under the weakly guiding approximation (second column onwards). The arrows in the first column indicate the interrelationships between the exact (vector) modes and the LP modes. For example, (in the weakly guiding approximation) the LP_{01x} mode is identical to HE_{11x}, whereas LP_{11ax} can be obtained as a sum of the TE_{01} and HE_{21a} modes.

in conventional fibres), modes can be represented by simpler expressions such that the transverse field is polarized in one direction only [56]. The resulting modes are known as the LP (linearly polarized) modes. In this case, we can classify modes in terms of linearly polarized mode groups LP_{rs}, with r and s integers and $r \geq 0$, $s > 0$. The LP modes may be represented by superpositions of exact (vector) modes, which are found to be degenerate under the weakly guiding approximation. The relationship between the exact modes (TE, TM, EH, HE) and the LP modes is summarized in Table 2.1 for the first two LP mode groups.

An LP_{rs} mode group in an isotropic fibre is degenerate. As an example, Fig. 2.1 shows the four degenerate modes of the LP_{11} mode group. The plots in Fig. 2.1 (top row of (a) and (b)) show the intensity profiles of the LP_{11a} and LP_{11b} modes respectively. Hence, the choice of numbers r and s specifies the overall form of the spatial intensity pattern of a given mode group, whereas a and b specify the orientation. The bottom row shows **E**-field vector plots for the linearly polarized modes corresponding to each spatial pattern. The spatial mode LP_{11a} is polarization degenerate, and we denote the two possible polarizations by LP_{11ax} and LP_{11ay} (similar notation applies to LP_{11b}). Superpositions of these may be used to obtain arbitrary SOPs.

Further, only modes with $r \neq 0$ possess spatial degeneracy, giving two orthogonally oriented intensity patterns as in the preceding example (super-

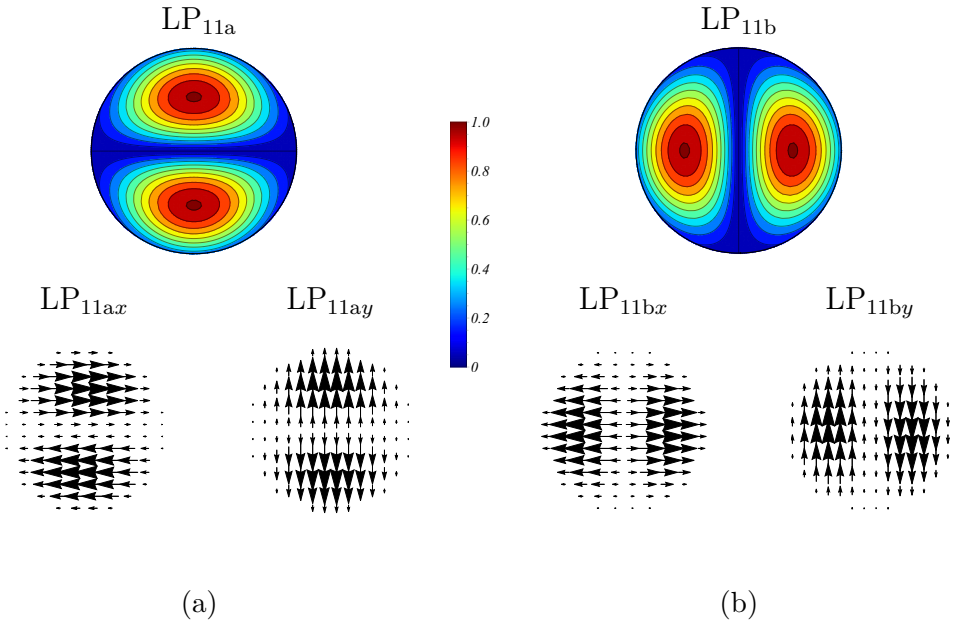

Figure 2.1. (a) Top: normalized intensity profile of the $\mathrm{LP}_{11\mathrm{a}}$ mode. Bottom: **E** field vector plots of the polarization degenerate modes of LP_{11}: the x-polarized $\mathrm{LP}_{11\mathrm{a}x}$ mode (left) and the y-polarized $\mathrm{LP}_{11\mathrm{a}y}$ mode (right). (b) The same plots as (a), but for the $\mathrm{LP}_{11\mathrm{b}}$ mode.

positions of these can be used to form arbitrarily oriented LP_{rs} profiles). Thus, LP modes with $r \neq 0$ are four-fold degenerate and those with $r = 0$ are two-fold degenerate (such as the fundamental mode LP_{01}).

2.2 Linear propagation of the LP_{11} group in a birefringent fibre

Linear (in addition to nonlinear) light propagation in multimode fibres has been the subject of detailed study especially over the past decade [28], [58]–[62]. Interest in this area stems from applications such as space-division multiplexing, astronomy and biomedical imaging. As we shall see later in this work, it also has implications for nonlinear processes in multimode fibres. As a result, efficient methods for the characterization of the modal properties of multimode fibres have been proposed and demonstrated [32], [38], [63].

In the previous section, we saw how light propagation in a multimode fibre is considered in terms of its spatial mode groups under the weakly guiding approximation. However, it is an idealized treatment and ignores a matter of

practical significance. This relates to the random coupling between the modes in each group occurring due to various perturbations (bends, twists, fibre imperfections etc.) to the ideal notion of a straight and circularly symmetric waveguide. As a result of these perturbations, these modes do not remain truly degenerate, and their propagation constants differ slightly and randomly along the fibre.[2] The random nature of propagation of these *quasi*-degenerate modes makes it very difficult to model deterministically the propagation of light in a multimode fibre. This is true even in relatively simple situations: for a fabricated (circular) two-mode fibre[3] of length ~1 m and supporting mode groups LP_{01} and LP_{11}, an LP_{11} beam will not retain its initial field composition due to coupling between the quasi-degenerate modes in this mode group [62]. Therefore, for any given mode group, the output beam profile (intensity pattern, orientation, polarization) in a fixed reference frame will in general be different from that at the input.

Despite the random nature of light propagation discussed above, researchers have demonstrated the ability to achieve control over the output state (polarization plus spatial) of light by computing the transfer matrix of a multimode fibre. This relies on experimental data gathered by carrying out multiple-input multiple output measurements as discussed in [64], [65]. Moreover, control of the polarization state of the total output field in a MMF (with random coupling) has been shown to be realized by shaping only the input spatial wavefront [66]. Other studies such as [67], [68] have used bimodal fibres in calculating the fibre input-output relations.

One of the ways in which greater predictability and control can be exercised over linear propagation is by the use of polarization maintaining (PM) fibres [56]. By introducing stress or geometrical asymmetry into the design of the waveguide, it is possible to increase the separation between the propagation constants of modes within a mode group. Depending on the strength of the induced birefringence, it can result in a considerable reduction in the coupling between these modes. This can simplify the characterization process and allow greater flexibility in designing systems that require more stability in harsh operating conditions.

Differently from the transfer-matrix approach, in the next two subsections,

[2] This is also discussed in more detail in Section 4.3 and Chapter 6.

[3] In this thesis, 'n-mode fibre' means a fibre that supports propagation of n non-degenerate spatial modes. Specifically which modes are involved will be mentioned on a case-by-case basis.

we will investigate the dependence of the LP_{11} output wavefront on input polarization in a linearly birefringent PM fibre in which the impact of random mode coupling is significantly limited by the non-degeneracy of its constituent modes. We will demonstrate the ability to switch between the odd and even modes of this mode group and identify the associated constraints on the input beam. This work was done in collaboration with Massimiliano Guasoni at the ORC.

Before diving into the above subject, some words on how LP_{11}-only propagation can be practically realized are in order. To launch a specific mode, the physical condition that needs to be satisfied is that the incident electromagnetic field must match exactly the intensity and phase profile (such as shown in Fig. 2.1 for LP_{11}) of that particular mode at the input facet of the waveguide. In practice, this is implemented by transmitting or reflecting a collimated laser beam from a mask that shapes it into the pattern of the desired mode, and the resulting field is then focused into the input facet of the fibre [30], [35].

For our purposes, the mask will take the form of a glass-based binary phase-plate (PP) divided into two half-planes, each with a different (constant) thickness. Such a PP can be fabricated by means of a photolithography and etching procedure [36]. For light in the C-band (1530 nm to 1565 nm) and L-band (1565 nm to 1625 nm), the phase acquired by propagation through one half-plane differs from that of the other by π to good approximation. An incident (collimated) beam from a SMF centred at the common boundary of these half-planes (the axis of the PP) provides a field distribution having the right phase profile and approximately the correct amplitude distribution for good coupling into the LP_{11} mode [34].

The method described above is shown conceptually in the left/upper portion of Fig. 2.2. Here, α denotes the angle between the reference frame defined by $x'y'$ aligned with the (fixed) fibre birefringence axes and the frame xy attached with the movable PP axes. Hence, α determines the orientation of the PP.

Within a given reference frame, say xy ($x'y'$), the LP_{11a} mode is defined as being aligned with the y (y') axis (aligned in the sense that in Fig. 2.2, the LP_{11a} profile is *parallel* to the y- and $y'-$axes). Therefore when $\alpha = 0$, the LP_{11} mode group is identical in both frames. In the nontrivial case $\alpha \neq 0$, this is no longer true. For instance, Fig. 2.3 illustrates the spatial modes in each reference frame when $\alpha = \pi/4$. The frames' orientations are shown in

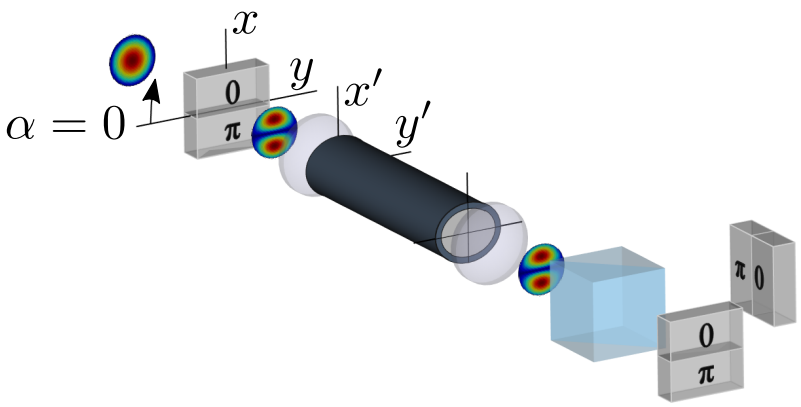

Figure 2.2. Conceptual illustration (also see text) showing a holographic phase plate (PP) being used to launch a HOM into a birefringent fibre. Frame xy depends on PP angle α. The birefringence-axes frame $(x'y')$ is the laboratory frame. The field pattern after the phase plate corresponds to the LP_{11a} mode in both frames because $\alpha = 0$.

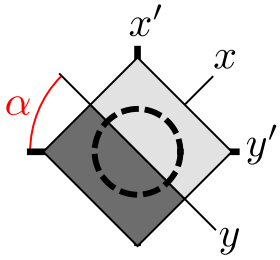

(a)

xy-frame		$x'y'$-frame	
LP_{11a}	LP_{11b}	LP_{11a}	LP_{11b}
			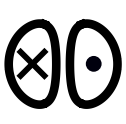

(b)

Figure 2.3. (a) Orientations of the reference systems xy and $x'y'$. The shaded portions are the half-planes of the PP. (b) LP_{11a} and LP_{11b} mode profiles in the xy and $x'y'$ reference systems (dotted lobe is in anti-phase with crossed lobe).

Fig. 2.3(a). Fig. 2.3(b) shows the LP_{11a} and LP_{11b} mode profiles when the chosen basis corresponds to either frame xy or $x'y'$. Note that LP_{11a} is parallel to the y-axis in the former frame and (parallel) to the y'-axis in the context of the latter frame.

2.2.1 Spatial rotation of LP_{11} intensity profile by polarization change

Now we address how the field may be represented at the input of the FMF. For propagation in the fibre, the $x'y'$ basis would be most convenient. Then, the general expression for the input electric field $\mathbf{E}_{\mathrm{IN}}$ can be written as a linear

combination of elliptically polarized $\mathrm{LP}_{11\mathrm{a}}$ and $\mathrm{LP}_{11\mathrm{b}}$ spatial modes aligned along the y' and the x' directions respectively:

$$\mathbf{E}_{\mathrm{IN}} = m'_{\mathrm{a}}(i'_{\mathrm{a}x} \cdot \mathbf{x}' + i'_{\mathrm{a}y} \cdot \mathbf{y}') + m'_{\mathrm{b}}(i'_{\mathrm{b}x} \cdot \mathbf{x}' + i'_{\mathrm{b}y} \cdot \mathbf{y}').$$

Here $m'_{\mathrm{a}}(x, y)$ ($m'_{\mathrm{b}}(x, y)$) represents the normalized transverse profile of the $\mathrm{LP}_{11\mathrm{a}}$ ($\mathrm{LP}_{11\mathrm{b}}$) mode (see also Fig. 2.1) and the coefficients $\{i'_{\mathrm{a}x}, i'_{\mathrm{a}y}\}$ ($\{i'_{\mathrm{b}x}, i'_{\mathrm{b}y}\}$) denote the input amplitudes of its x'- and y'-polarized components respectively (primes over x, y are dropped in expressions involving i' and m'). $\mathbf{x}'$ ($\mathbf{y}'$) is a unit vector along the x' (y') axis. Additionally, $\mathbf{A}'_{\mathrm{IN}} = [i'_{\mathrm{a}x} \quad i'_{\mathrm{a}y} \quad i'_{\mathrm{b}x} \quad i'_{\mathrm{b}y}]$ is the vector of input amplitudes, and depends on the polarization of the input beam.

The same notation above applies for the frame xy with the substitutions $x' \to x$, $y' \to y$, $i' \to i$, $m' \to m$. In this frame, the field representation at the fibre input is particularly simple. Because the PP axis is the y-axis, the field can be written as a combination of $\mathrm{LP}_{11\mathrm{a}}$-like modes only. Therefore $\mathbf{A}_{\mathrm{IN}} = [i_{\mathrm{a}x} \quad i_{\mathrm{a}y} \quad 0 \quad 0]$, regardless of the value of α.

While calculations can be made for obtaining the output pattern resulting from LP_{11} propagation through the fibre for arbitrary α by appropriate linear transformations [58], [69], we will illustrate in detail the instances $\alpha = 0$, $\pi/2$ and $\alpha = \pi/4$, as they are most useful in illustrating of the role of input polarization in the control of output spatial profile.

It has already been stated that in a highly birefringent PM fibre, the LP_{11} mode group is fully non-degenerate. If a mode such as $\mathrm{LP}_{11\mathrm{a}x}$ is launched selectively, it propagates without cross-talk with other modes in its group. Thus, we can say that whenever the PP is aligned with one of the fibre axes ($\alpha = 0$ or $\alpha = \pi/2$), the intensity profile is constant and independent of the input polarization. Fig. 2.4(a) shows the case $\alpha = 0$ in which the transverse profile at the fibre input is fully aligned with the y'-axis of the fibre, so that the output power remains fully coupled to the $\mathrm{LP}_{11\mathrm{a}}$ mode. Fig. 2.4(b) shows the complementary case $\alpha = \pi/2$. Here, conditions are ideal for a $\mathrm{LP}_{11\mathrm{b}}$ launch, and the output intensity profile is identical to that at the fibre input.

On the contrary, when $\alpha = \pi/4$ (see Fig. 2.5) the input power is equally split among the fibre axes, so that both the $\mathrm{LP}_{11\mathrm{a}}$ and $\mathrm{LP}_{11\mathrm{b}}$ modes of the fibre are excited. First consider the instance in which the input polarization is parallel to the x'-axis of the fibre. In this case, the input field can be

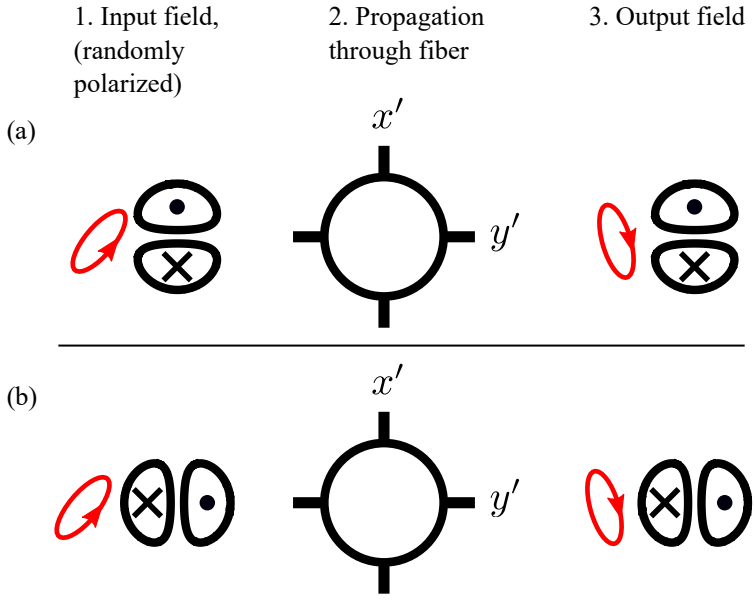

Figure 2.4. If $\alpha = 0$, spatial output is insensitive to input polarization (likewise for $\alpha = \pi/2$).

decomposed as the sum of two x'-polarized modes: $\mathbf{E}_{\mathrm{IN}} = \mathbf{x}' \cdot (i'_{\mathrm{a}x} m'_{\mathrm{a}} + i'_{\mathrm{b}x} m'_{\mathrm{b}})$. These two fibre modes have equal amplitudes and are in phase at the fibre input (Fig. 2.5(a)), nevertheless each of them accumulates a different phase delay in propagation. If their phase mismatch Δd_x is an even multiple of π, then the modes in $\mathbf{E}_{\mathrm{IN}}$ add in phase at the fibre output, so no difference is observed with respect to the input field (Fig. 2.5(b)).

Now consider the case in which the input polarization is parallel to the y'-axis so that $\mathbf{E}_{\mathrm{IN}} = \mathbf{y}' \cdot (i'_{\mathrm{a}y} m'_{\mathrm{a}} + i'_{\mathrm{b}y} m'_{\mathrm{b}})$ (Fig. 2.5(c)). Then, if the accumulated phase mismatch Δd_y is an odd multiple of π, the output modal amplitudes ($i'_{\mathrm{a}y}$ and $i'_{\mathrm{b}y}$) are in anti-phase so that a $\pi/2$ rotation is observed with respect to the input field (see Fig. 2.5(d)).

In summary, the example in Fig. 2.5 points out the polarization sensitivity of the system under analysis, which is in contrast to the case in Fig. 2.4. With $\alpha = \pi/4$, when the input polarization goes from linearly polarized along one fibre axis to the other (from x' to y' or vice versa), the output field undergoes a $\pi/2$ spatial rotation. In more detail, we switch from an output $\mathrm{LP}_{11\mathrm{a}}$ mode aligned with the x-axis of the phase plate (Fig. 2.5(b)) to an output $\mathrm{LP}_{11\mathrm{b}}$ mode aligned with the y-axis of the phase plate (Fig. 2.5(d)). On the contrary, when $\alpha = 0$ or $\pi/2$, the output field distribution is polarization insensitive and

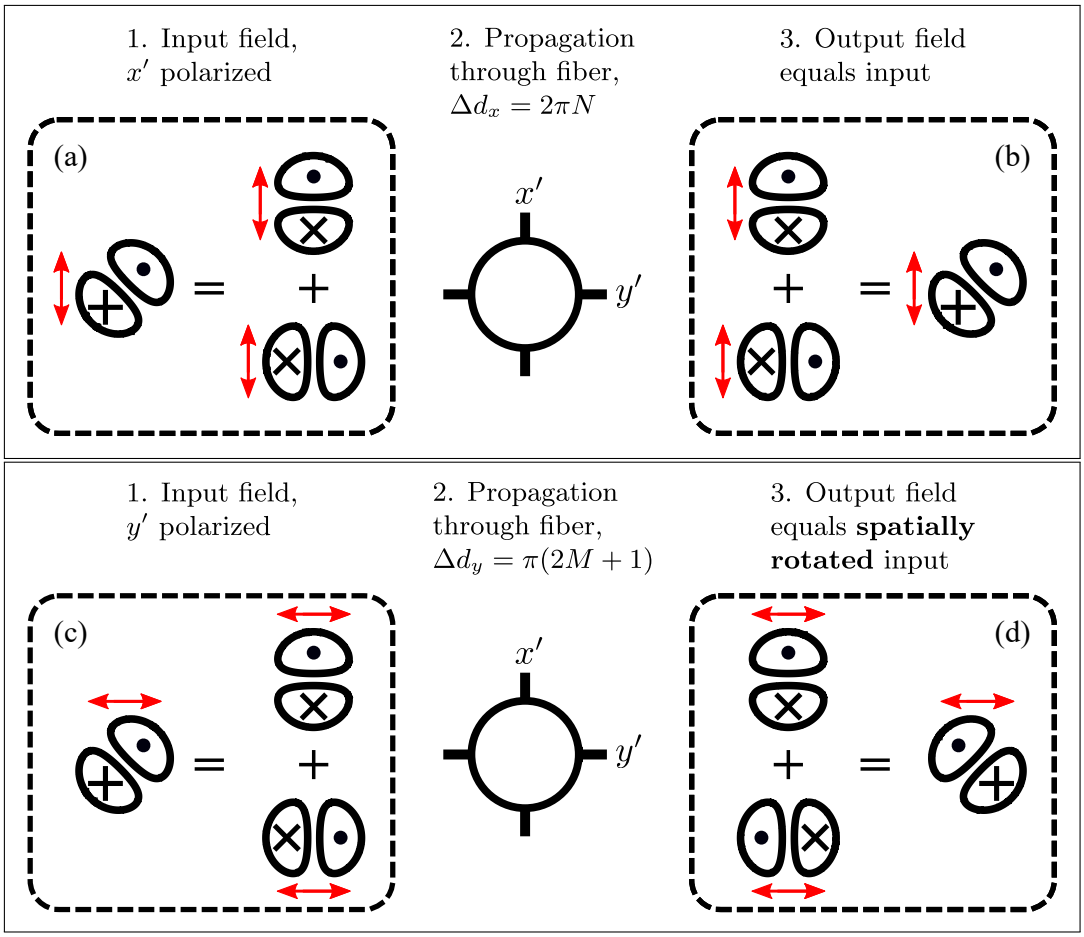

Figure 2.5. Polarization sensitive setup ($\alpha = \pi/4$). The fibre is such that $\Delta d_x = 2\pi N$, whereas $\Delta d_y = \pi(2M+1)$. (a) Decomposition of the x'-polarized input field as a linear superposition of m'_{a} and m'_{b}. (b) An in-phase superposition at the output ($\Delta d_x = 2\pi N$) results in an output LP_{11} mode profile having the same spatial orientation as the input. (c) Decomposition of the y'-polarized input field. (d) When $\Delta d_y = \pi(2M+1)$, the out of phase superposition results in output that is rotated by $\pi/2$ with respect to the input field.

is unchanged from its input configuration (Fig. 2.4).[4]

The remainder of this chapter provides an experimental demonstration of the ideas summarized in the previous paragraph.

[4]One may ask what the range of spatial rotation is for all values of θ such that $|\theta| < \pi/4$. It can be shown analytically that in this case, the achievable rotation is always less than $\pi/2$.

2.3 Experimental setup

Our experimental setup was a practical realization of the scheme illustrated in Fig. 2.2. A birefringent FMF was needed for this purpose. The fibre used for this experiment was a commercially available panda style PM fibre (Thorlabs Part Number PM2000). Having a core radius of 7 µm and a beat length of 5.2 mm at 1950 nm, it was specified for polarization-maintaining single-mode operation at wavelengths greater than 1850 nm. The second-mode cutoff wavelength of the fibre was 1720 nm; it could therefore be effectively used as a two-mode-group fibre (guiding the LP_{11a} and LP_{11b} modes) at the telecom C- or L-bands. The length of the fibre was 3 m.

The first step in the implementation of our main setup was finding the birefringence axes of the fibre. High precision fibre rotators were used to align the principal polarization axes of the fibre such that one of them was parallel to the plane of the optical bench and the other was perpendicular to it. This was done by means of a polarimetric technique [70] (sometimes referred to as the cross-polarizer method) using a broadband amplified spontaneous emission (ASE) source. The working principle of this method is schematically represented in Fig. 2.6.

To describe the operation of the setup shown in Fig. 2.6, we assume (in this paragraph) that light is guided in the LP_{01} mode only (this was realized in practice by inducing sufficient bend loss in the fibre). When light of a given wavelength is launched linearly polarized (with the help of a polarizing beamsplitter (PBS) in our case) along the x' (or y') axis of the fibre under test (FUT), it will emerge as linearly polarized along the same axis because it is PM. If the light is polarized at an acute angle to x', then it will couple to both polarization modes, and the output will in general be elliptical due to the out-of-phase x' and y' components. Any changes in frequency will precess the Stokes vector of output light about the slow (i.e. higher index)

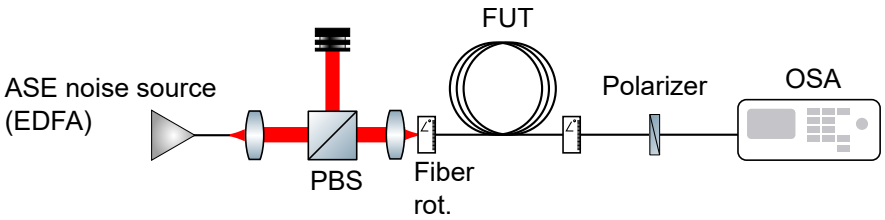

Figure 2.6. Setup for identification of fibre birefringence axes.

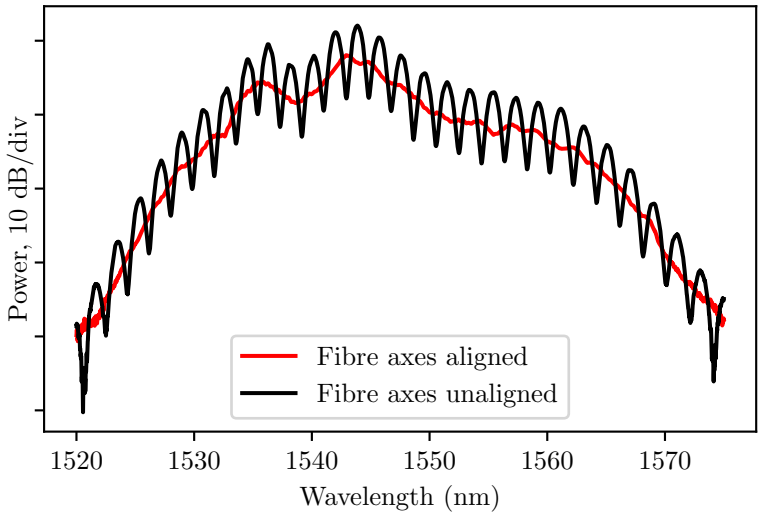

Figure 2.7. ASE spectrum for the case when the (linear) polarization of light launched into the fibre is aligned with one of its birefringence axes, versus when it is out of alignment.

fibre axis [71]. Therefore when a polarizer is placed at the output, a change in frequency leads to a change in measured output intensity. When linearly polarized broadband light is launched into the fibre, this will manifest as ripples in the light spectrum, as shown in Fig. 2.7 ('Fibre axes unaligned') for the FUT. However, by suitably rotating the fibre axes at both ends (input and output) we can reach a configuration in which the undulations of the spectrum are minimized, thereby finding the directions of the birefringence axes, as shown in Fig. 2.7 ('Fibre axes aligned').

Once the birefringence axes had been determined using the method above, the setup shown in Fig. 2.8 was used to experimentally test the ideas discussed in the previous section. A 1530 nm continuous wave (CW) diode laser was the light source and an (electronically) programmable liquid-crystal based polarization controller was used to control the polarization of light into the fibre.

As described earlier in this chapter, to excite the LP_{11} mode in the fibre, we used a binary free-space phase-plate to shape the input beam into the requisite phase profile [35]. The intensity profile of the collimated output beam was imaged on an infrared camera when required.

To analyse the output in terms of two orthogonal (spatial) modes and

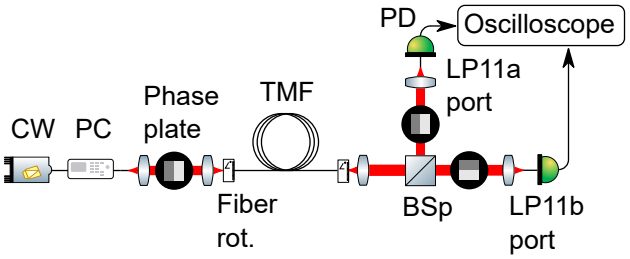

Figure 2.8. Experimental setup for mode launch and decomposition.

to demonstrate how polarization controlled mode modulation can result in optical switching between two ports, we used a beamsplitter (BSp) cube to divide the output to two paths with perpendicularly oriented PPs (see Fig. 2.8 and right/lower part of Fig. 2.2). The output PPs were rotated by the same angle α as the input PP. By reciprocity with the launch method illustrated in the left/upper part of the same figure, this decomposed the beam in the spatial basis along the PP axes. Each path terminated with the light being focused into a single-mode fibre (the output port(s)), whose power was monitored by means of a photo-detector (PD) and oscilloscope. Maximum (minimum) power was directed to an output port when the beam at the FMF output was composed of one of the LP_{11} spatial modes oriented along (perpendicular to) its PP axis. For example, the emerging output beam shown in Fig. 2.2 will couple very strongly (weakly) into the port that lies in its straight (perpendicular) path.

2.4 Experimental results

The polarization (in)sensitive configurations were tested experimentally. First, the PPs were aligned along either fibre axis ($\alpha = 0$ or $\pi/2$), thereby launching exclusively LP_{11a} or LP_{11b}. Fig. 2.9 shows the measured power at each LP_{11} port versus time when $\alpha = 0$ and the input polarization was scrambled randomly using the polarization controller. Typical examples of observed output are shown as insets in Fig. 2.9. As expected, the output profiles were strongly aligned with the input beam orientation, and remained fundamentally unaltered with changes in input polarization. For the LP_{11} mode, when the input polarization was linear and launched along one of the birefringence axes, polarization holding was measured to be in excess of 19 dB (the same figure

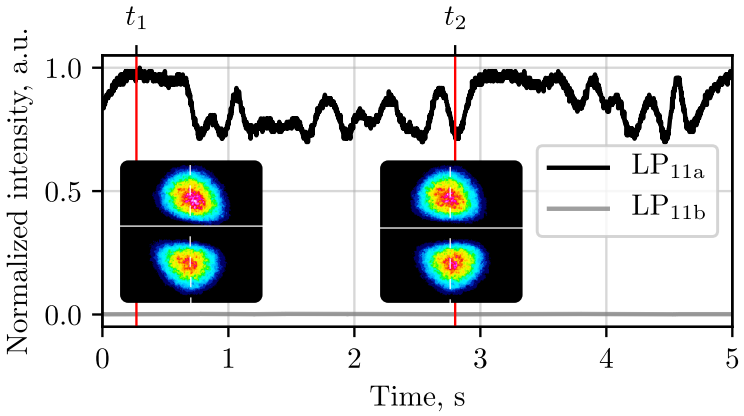

Figure 2.9. Power at ports LP_{11a} and LP_{11b} when polarization is changed randomly, with the PP aligned with one of the principle axes of the birefringent fibre.

for the LP_{01} mode was 35 dB). While the graph shows limited fluctuation in LP_{11a} power which can be ascribed to polarization dependent loss and imperfect alignment in the optical system, the difference in power between LP_{11a} and LP_{11b} exceeded 18 dB at all times. This agrees with the theoretical prediction that if $\alpha = 0$ (or $\pi/2$), the system is polarization insensitive.

Next, the input and output PPs were aligned diagonally with respect to the fibre axes, i.e. $\alpha = \pm\pi/4$ (the output PPs were rotated because we wish to compare the input/output powers in the same reference system). As expected, this configuration proved to be polarization sensitive. Fig. 2.10 shows the variation of power at each port versus time, as the polarization controller changes the input polarization from linear vertical (time t_1) to horizontal (time t_3) and then back. Also shown are images of the output beam shape at various stages of the power transition. The fact that the exchange of power between the two ports and the $\pi/2$ spatial rotation of the output beam were both achieved by switching between the aforementioned states of polarization provides strong validation of our theoretical model (see Fig. 2.5).

We can therefore infer that in the case shown, Δd_x (Δd_y) is nearly an even (odd) multiple of π. It should be noted that, for an ideal (straight) fibre, the phase mismatch terms Δd_x (Δd_y) are fixed. However, by spooling the fibre with different radii of curvature, or by stressing the fibre at one point, we can perturb the phase accumulated during propagation by each mode, and therefore change Δd_x (Δd_y). An optimum position which maximized the

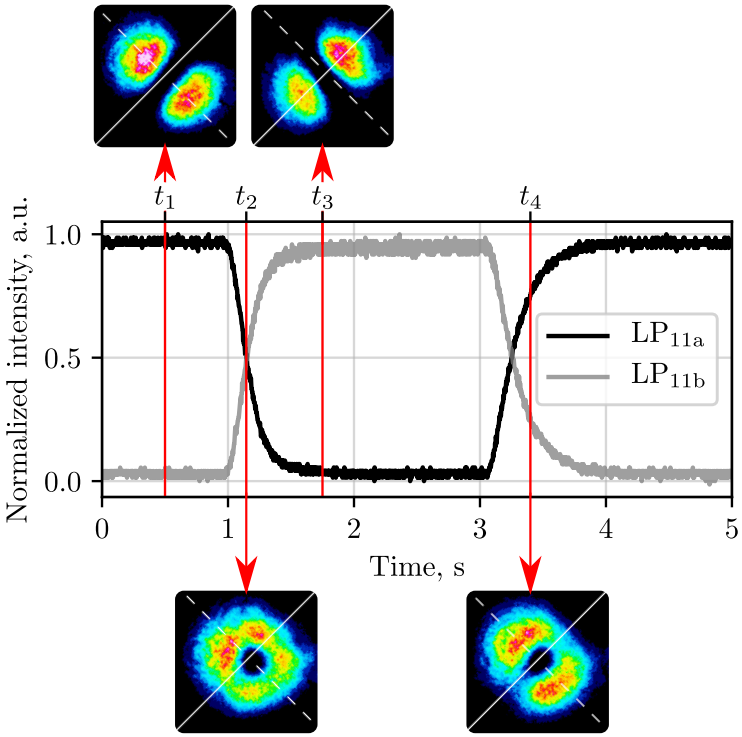

Figure 2.10. Transfer in power between ports LP_{11a} and LP_{11b} due to change in polarization when the PP is aligned at 45° to the principle axis of the birefringent fibre.

polarization sensitivity of the system could nevertheless be found easily; a maximum power extinction ratio of 13 dB was reached between the ports. In the intermediate cases represented at times t_2 and t_4 in Fig. 2.10, the beam resembled – in line with theory – superpositions of out-of-phase LP_{11a} and LP_{11b} modes.

2.5 Conclusions

We have introduced the description of fibre modes under the weakly guiding approximation. Subsequently, we used this description to study the propagation of the LP_{11} mode group in a birefringent fibre, and exploited the phase delay among its constituent modes to specify a scheme for polarization based all-optical control over output spatial intensity.

This control is exercised when the launch beam is oriented at an angle of $\pm\pi/4$ with respect to the fibre axes. In general, a superposition of LP_{11a}

and LP_{11b} modes which varies with input polarization is obtained. However, when input light is switched from being linearly polarized along one fibre axis to the other, $\pi/2$ rotation of the spatial field pattern is realized, and the output switches from a (pure) LP_{11a} profile to LP_{11b}. The speed of this transition is essentially determined by the speed of the polarization controller, and could therefore be on the order of picoseconds. Moreover, the scheme described here can also be applied to other higher-order modes, e.g. to switch from LP_{12a} to LP_{12b}, by using the appropriate phase mask. This may open new opportunities for all-optical, ultrafast modulation of higher-order-modes in space-division-multiplexing. Moreover, by launching any number of higher-order modes in addition to the LP_{11} group, one may obtain a variety of complex spatial intensity patterns controlled by input polarization only, which may find applications in areas such as near-field spectroscopy and sensing.

Chapter 3

Intra-modal and inter-modal Four-wave mixing

Most of the basic concepts relating to linear propagation that are relevant to this work were covered in the last chapter. In this chapter we move on to aspects of nonlinear light propagation in SMFs and MMFs. Central to the efficiency of FWM processes is the phenomenon of dispersion. This topic will be dealt with in the first section, in which a method for characterizing the dispersion properties of a FMF will be shown. The next section will briefly cover the rudiments of FWM in a SMF. Since this involves FWM in a single mode only, we refer to this as *intra*-modal FWM. Thereafter, we discuss IM FWM, which involves nonlinear interaction(s) between waves in different spatial modes, and will therefore utilize a FMF. The framework developed here will also be referred to in all later portions of this work.

3.1 Time-of-flight dispersion measurement of modes

3.1.1 Motivation

In the discussions so far, we have assumed modes to be travelling at discrete frequencies. It should be noted, however, that the continuous variation of β with frequency gives rise to dispersive effects which can be examined by expanding it in a Taylor series about a central frequency ω_0. Taking β_n to be the n-th derivative at ω_0, β_0 describes the longitudinal phase shift per unit

length. Further, β_1 can be shown to be the inverse group velocity (IGV) of a pulse with carrier frequency ω_0. Moreover β_2, referred to as the group velocity dispersion (GVD) parameter, describes the rate of change of β_1 with frequency and is related to the *dispersion parameter* D by $\beta_2 = -(\lambda^2/2\pi c)D$.

While the parameters mentioned above describe linear propagation characteristics of a fibre, we shall soon see that they have a significant role in the efficiency of nonlinear effects also. Given that a number of different fibres were used in this study, a method for experimentally obtaining their dispersion properties was required. To this end, we now specify a method used to characterise the dispersion properties of the modes supported by a FMF. In particular, we will apply this method to a 1 km-long three-mode fibre supporting low-loss propagation of modes LP_{01}, LP_{11a} and LP_{11b}. Before a discussion of the method used, we present briefly some details relating to the FUT.

3.1.2 The fibre under test

Our FMF, fabricated by OFS Denmark, was an elliptical core (EC) graded-index (GI) fibre with an index trench for improved bend loss performance (see [26], [72], [73] for details). The fibre loss was about 0.2 dB/km for all modes, and the computed effective area of mode LP_{01} (LP_{11a} or LP_{11b}) was 89 μm^2 (125 μm^2) [73].

The fact that the FUT was slightly elliptical (an ellipticity of 10% was specified) broke the spatial degeneracy of the LP_{11} mode group and allowed for its spatial modes (i.e. LP_{11a} and LP_{11b}) to propagate with low linear mode coupling. Due to the low cross-talk among spatial channels, the use of EC fibres has been proposed for space division multiplexing (SDM) in direct-detection based intra-datacenter network (short reach) applications in order to avoid the high equipment and operating costs associated with MIMO DSP [73].

Despite the independent propagation of the spatial modes of our FMF, their polarization degeneracy persisted [73]. These properties could be qualitatively tested by selectively launching one spatial mode and observing changes to the spatial and polarization characteristics of the output as the FUT was bent or twisted. When this was done, no change was observed in spatial output whereas polarization was scrambled randomly. On the other hand, if the same were done to an ideal circular-core two-mode fibre in which the LP_{11} group was (quasi) degenerate, a physical disturbance to the fibre would result in a

random distortion of the intensity profile.

3.1.3 Experimental method and results

Our method was based on measurements of the impulse response of a fibre at different wavelengths [74]. Given that the LP_{11} mode group of the fibre was spatially non-degenerate, LP_{11a} and LP_{11b} could have different group velocities. Therefore, in our three-mode fibre, a short pulse launched at the input of the fibre would emerge as three distinct pulses at the output, whose relative time-of-flight (TOF) (or group delay(s) τ_g) could be quantified. Then, the dispersion of each mode could be computed by using the relation $\tau_g = L\,\mathrm{d}\beta/\mathrm{d}\omega$, where L is the length of the fibre. This is applicable as long as the output pulse widths are shorter than the group delay(s). In our case, a low repetition-rate tunable laser producing few-picosecond pulses was the input source and the output was measured using a fast oscilloscope, using which pulse-widths of more than 50 ps could be resolved.

A setup diagram for implementing the method above is shown in Fig. 3.1(a). A free-space PP (same as the one introduced in the previous chapter) was used for selective excitation of the modes when required. Fibre rotators were used at the input and output facets of the FUT to align the principal axes of the elliptical fibre core with the PP axes, enabling excitation of the HOMs with high purity.

Generally, when an impulse such as the one whose oscilloscope trace is shown in Fig. 3.1(b) was launched into our FMF, it resulted in traces typified by the one shown in Fig. 3.1(c). Due to the differences in the effective indices of the HOMs induced by the core ellipticity, three distinct peaks corresponding to modes LP_{01}, LP_{11a} and LP_{11b} are visible, indicating different arrival times for each mode. The temporal separation between any two peaks is the relative group delay (or equivalently relative inverse group-velocity (RIGV)) between the corresponding modes. A complete set of measurements were made to determine the modal group delays for the FUT for a range of wavelengths in the C-band. The final results are graphed in Fig. 3.1(d). It can be seen that while the group delays increase with wavelength (hence all modes exhibit anomalous dispersion), the differential mode delay (DMD) for any pair of modes is largely wavelength independent.

Fig. 3.1(e) shows the time-domain traces when each mode was launched

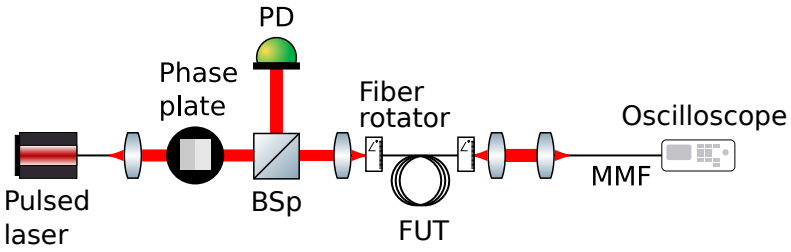

(a) Setup for time-domain dispersion measurement of modes. The phase plate is only used when a mode is to be launched selectively, as in (e) below.

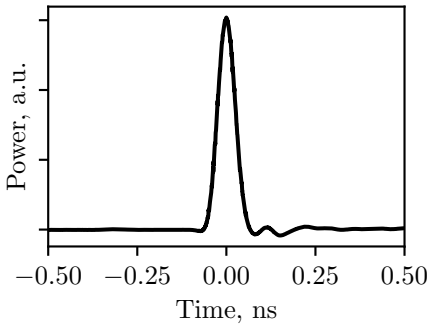

(b) Oscilloscope trace of impulse at the input end of the FMF.

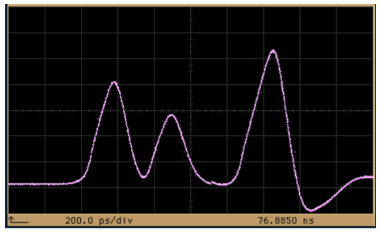

(c) Example time-domain output (oscilloscope screenshot) at output of the three-mode elliptical core fibre.

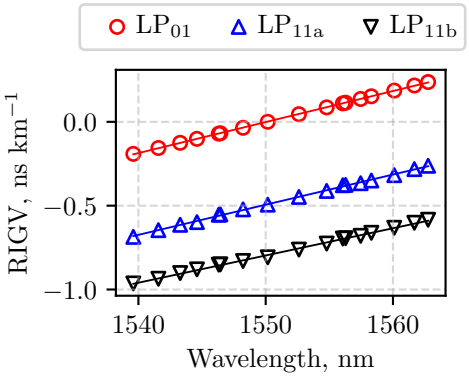

(d) Measured group delays (or relative inverse group velocities (RIGVs)) for the modes of the three-mode fibre.

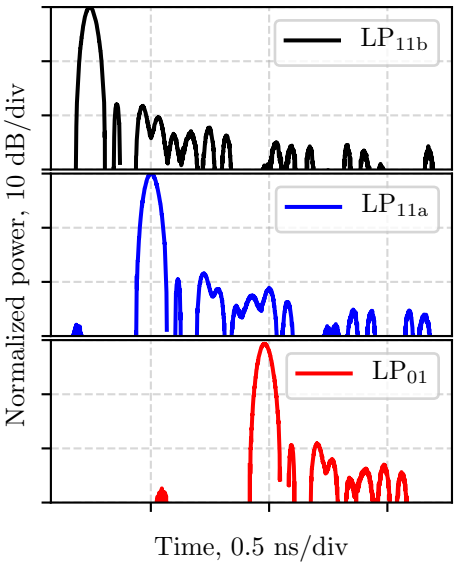

(e) Time-domain output at end of FUT when each mode was launched selectively.

Figure 3.1. Time domain dispersion measurement by the time-of-flight method.

selectively with an effort to minimize the transmission of the other modes. Since each trace is plotted when power in one mode is maximized at the expense of the other modes, it also gives the extent of modal coupling. By comparing the relative differences in peak powers under selective excitation, it was possible to compute the ratios for modal purity. A modal purity of approximately 27 dB for the fundamental mode can inferred from the figure. Modal purities of the HOMs exceeded 20 dB.

In addition, the dispersion parameters for each mode could be evaluated as the slopes of the RIGV curves and are listed in Table 3.1.

Mode	Dispersion parameter, ps/(nm km)
LP_{01}	18.5
LP_{11a}	18.0
LP_{11b}	16.3

Table 3.1. Measured dispersion for each mode of the elliptical core few-mode fibre.

3.2 Four-wave mixing in a single-mode fibre

In the previous chapter, it was mentioned that light propagation in a fibre could be analysed by solving Maxwell's equations subject to certain parameters such as core radius and refractive indices of the core and cladding. While their solutions in terms of the linearly polarized (LP) modes were also presented, not much was said about how the solutions were arrived at. Now that we are considering nonlinear propagation, it will be useful to briefly describe certain aspects of the equations that lead to solutions which are different from the linear regime, and which give rise to phenomena that are not observed in the latter.

3.2.1 Theory

In the process of solving Maxwell's equations, one specifies the form of polarization $\mathbf{P}$ (not to be confused with the state of polarization or SOP of $\mathbf{E}$) of the chosen material. This is a variable which relates to how the material

responds macroscopically to an applied field (more specifically, the polarization $\mathbf{P}$ is the dipole moment per unit volume). When the field intensity is sufficiently low, the dielectric response can be treated as linear: $\mathbf{P}$ is proportional to $\mathbf{E}$ such that $\mathbf{P} = \mathbf{P}_{\mathrm{L}} \equiv \epsilon_0 \boldsymbol{\chi}^{(1)} \cdot \mathbf{E}$, where ϵ_0 is the permittivity of free space and $\boldsymbol{\chi}^{(1)}$ is the electric susceptibility tensor. The expression for $\mathbf{E}$ assumes that the polarization response is instantaneous, which requires $\boldsymbol{\chi}^{(n)}$ to be independent of time and frequency, and implies a neglect of certain effects such as stimulated Raman scattering (SRS) and SBS [75]. Given that the settings for our experiments will not be optimum for the generation of these effects, this is a valid assumption to make. At higher intensities, the linear approximation loses validity, and one must take into account nonlinear contributions to $\mathbf{P}$. This is done by considering higher order polarization terms so that $\mathbf{P} = \epsilon_0 \left(\boldsymbol{\chi}^{(1)} \cdot \mathbf{E} + \boldsymbol{\chi}^{(2)} \cdot \mathbf{E} \cdot \mathbf{E} + \boldsymbol{\chi}^{(3)} \cdot \mathbf{E} \cdot \mathbf{E} \cdot \mathbf{E} \right)$, where each $\boldsymbol{\chi}$ is a tensor quantity of appropriate order. The material polarization then becomes the driving term in the differential equation relating to the electric field inside the medium [76]. For the silica based fibres to be considered in this work, $\boldsymbol{\chi}^{(2)} = \mathbf{0}$, and the term involving $\boldsymbol{\chi}^{(3)}$ will be the most significant source of nonlinearity. It can be shown that due to various symmetries occurring in an isotropic medium, the components of the $\boldsymbol{\chi}^{(3)}$ tensor may be reduced from a maximum of 81 to just three elements [77]. Moreover, for silica (and also in general for many materials) the nonlinear polarization, i.e. the nonlinear part of $\mathbf{P}$ which we denote $\mathbf{P}_{\mathrm{NL}}$, is significantly smaller than the linear part (by about six orders of magnitude) [77], and this fact enables treating $\mathbf{P}_{\mathrm{NL}}$ as a perturbation in a number of calculations. For instance, the LP fibre modes are solved for in the approximation of linear dielectric response.

In this section we will assume linearly polarized CW input fields whose amplitudes change slowly with propagation distance (this is known as the slowly varying envelope approximation). Further we assume isotropy, which in the scalar case gives $\boldsymbol{\chi}^{(3)} \to \chi^{(3)}$ [77], and we ignore propagation losses. Then, by using perturbation theory to first order in $\mathbf{P}_{\mathrm{NL}}$, the electric field in the fibre may be represented as [77]

$$\mathbf{E}_n(\mathbf{r}, t) = A_n(z) m_n(\mathbf{r}_\perp) \exp i(\beta_n z - \omega_n t) \hat{\mathbf{x}} + \text{c.c.} \tag{3.1}$$

where c.c stands for complex conjugate. The above form for $\mathbf{E}_n$ should be familiar because it resembles the one already presented in the previous chapter.

It represents a mode with propagation constant β_n at (angular) frequency ω_n, slowly varying amplitude A_n and transverse profile m_n. The wave dynamics are therefore described by the (complex) amplitude A_n whose solution, as we shall see, can be obtained by methods of calculus.

The above paragraph summarizes the case of a single wave with a given frequency ω_n. Now, we present a summary treatment of FWM (see e.g. [77], [78] for details), which is a $\boldsymbol{\chi}^{(3)}$ mediated nonlinear interaction between two or more waves. A major consequence of FWM is that it results in a number of frequency conversion processes as well as self-induced effects in dielectric media. To show how FWM results in energy transfer between waves at different frequencies, we will consider an example in which two CW input waves are launched in an optical fibre, with one strong input at frequency ω_p (referred to hereby as the *pump*) and one weak input (termed the *signal*) at ω_s.

In the configuration above, the total electric field at the fibre input will now be the sum of two expressions of the form specified in eq. (3.1):

$$\mathbf{E} = \frac{1}{2}\hat{\mathbf{x}}\left[E_p \exp i(\beta_p z - \omega_p t) + E_s \exp i(\beta_s z - \omega_s t)\right] + \text{c.c.}, \tag{3.2}$$

where $E_j = A_j(z)m_j(\mathbf{r}_\perp)$. Since $\mathbf{P}_{\text{NL}}$ involves the cube of the total field, this will result in a number of polarization terms with a time variation described by the exponential factor $e^{-i\omega_m t}$, where $\omega_m \in \left\{\sum_{j\in\{s,p,q\}} \pm\omega_j > 0\right\}$. A chosen ω_m can therefore equal sums and/or differences of the input frequencies.

It is these new polarization terms that can drive the creation of new frequencies. For example, by interacting nonlinearly inside a fibre, the two CW inputs above can produce a wave at frequency $\omega_i = 2\omega_p - \omega_s$. We refer to this newly created wave as the *idler*. Since frequency is directly proportional to photon energy, the previous relation is also a statement regarding energy conservation: this process involves the simultaneous creation of the idler and signal photons at the expense of two pump photons. This quantum-mechanical analog is represented schematically in the energy-level diagram in Fig. 3.2.

By the above reasoning, we may write the total electric field and polarization waves in the fibre as

$$\mathbf{E} = \frac{1}{2}\hat{\mathbf{x}} \sum_{j=p,s,i} E_j \exp i(\beta_j z - \omega_j t) + \text{c.c.} \tag{3.3}$$

$$\mathbf{P}_{\text{NL}} = \frac{1}{2}\hat{\mathbf{x}} \sum_{j=p,s,i} P_j \exp i(\beta_j z - \omega_j t) + \text{c.c.}, \tag{3.4}$$

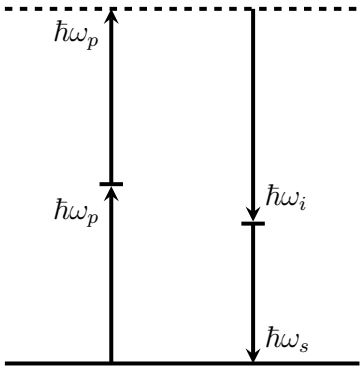

Figure 3.2. Energy level diagram for the FWM process with idler at ω_i.

where each P_j consists of terms with time varying frequency components $\{\omega_m\}$. Only a mixing process whose field spatially varies in sync with the induced polarization will be efficient (i.e. phase matched). Thus, for our purposes, we have ignored terms other than those relating to the pump, signal and the idler (which we anticipate to be efficiently generated) at $\omega_i = 2\omega_p - \omega_s$. With this restriction, substituting the above expressions for $\mathbf{P}_{\mathrm{NL}}$ and $\mathbf{E}$ into the electromagnetic wave equation results in a set of coupled nonlinear differential equations describing the evolution of the wave amplitudes [77]. If A_i, A_s and A_p are normalized field amplitudes of the idler, signal and pump so that $|A(z)|^2$ represents total power at a given longitudinal position, these coupled equations can be written as [77]:

$$\frac{\mathrm{d}A_i}{\mathrm{d}z} = i\gamma_i \left[\left(|A_i|^2 + 2|A_s|^2 + 2|A_p|^2 \right) A_i + A_p^2 A_s^* e^{i\Delta k z} \right] \tag{3.5a}$$

$$\frac{\mathrm{d}A_s}{\mathrm{d}z} = i\gamma_s \left[\left(|A_s|^2 + 2|A_i|^2 + 2|A_p|^2 \right) A_s + A_p^2 A_i^* e^{i\Delta k z} \right] \tag{3.5b}$$

$$\frac{\mathrm{d}A_p}{\mathrm{d}z} = i\gamma_p \left[\left(|A_p|^2 + 2|A_s|^2 + 2|A_i|^2 \right) A_p + 2A_i A_s A_p^* e^{-i\Delta k z} \right] \tag{3.5c}$$

where

$$\Delta k \equiv 2\beta_p - \beta_s - \beta_i \tag{3.6}$$

$$\gamma_j \equiv \frac{\omega_j n_2}{c A_{\mathrm{eff}}}, \quad j \in i, s, p. \qquad n_2 \equiv \frac{3\chi^{(3)}}{4\varepsilon_0 n^2 c}. \tag{3.7}$$

Δk is referred to as the phase mismatch for the process considered above. A_{eff} is the effective mode area defined as $\left(\iint \mathrm{d}\mathbf{r}_\perp |m(x,y)|^2\right)^2 / \iint \mathrm{d}\mathbf{r}_\perp |m(x,y)|^4$, and its definition assumes that the intensity pattern at all frequencies is approximately

the same. γ_j is referred to as the *nonlinear parameter* corresponding to wave j.

The terms in round brackets are responsible for self-phase modulation (SPM) and cross-phase modulation (XPM). As the name suggests, SPM is a self-induced effect that results in an intensity-dependent phase shift. Correspondingly, XPM results in a phase-shift also, but the magnitude of this shift depends on the intensity of a co-propagating wave. The above equations may be solved analytically (this requires elliptic functions), however it is possible to further simplify and decouple them if the following approximations are made:

- the input pump power is much higher than signal power,
- the pump is undepleted so that $|A_p|$ is approximately constant.

Further an average value for γ is assumed, and its frequency dependence is ignored. Then, with some algebra, the idler power can be obtained as [77]

$$P_i(z) = (\gamma P_{p0}/g)^2 P_{s0} \sinh^2(gz) \tag{3.8}$$

where

$$g^2 \equiv (\gamma P_{p0})^2 - (\kappa/2)^2 \tag{3.9}$$

$$\kappa \equiv \Delta k - 2\gamma P_{p0} \tag{3.10}$$

and P_{p0}, P_{s0} are the input pump and signal powers respectively. It can also be shown with some algebra that the gain reaches a maximum value of γP_{p0} when $\Delta k = 2\gamma P_{p0}$, and $g \geq 0 \quad \text{if} \quad 0 \leq \Delta k \leq 4\gamma P_{p0}$.

The idler experiences exponential gain with z if $\kappa = 0$, and sufficiently long interaction lengths can then be used to amplify idler power (the same is true for signal power). In the realistic case when pump depletion is taken into account, numerical computation shows that there is periodic exchange of power between the waves [77].

3.2.2 Experiment

We now compare the basic theory developed previously with an experimental investigation of the FWM characteristics of two different fibres. The effect of CW FWM will be studied on two different single-mode highly nonlinear fibres (HNLFs) with some of their properties (at 1550 nm) shown in Table 3.2.

Based on these figures, the dispersion profile of the N10 fibre is essentially flat, and lies entirely in the normal dispersion region ($D < 0$). On the other hand, the P1 profile keeps to the anomalous dispersion regime ($D > 0$) for $\lambda \gtrsim 1533\,\text{nm}$.

In the parametric interaction to be considered here, the pump wavelength was kept constant at $\lambda_p = 1550\,\text{nm}$. Then the effect on idler generation was observed with respect to:

1. variation of signal frequency ω_s ($\omega_s < \omega_p$). The pump (signal) input power was fixed at 12.06 dBm (−7.89 dBm). The signal frequency was detuned from the pump incrementally towards lower frequencies (longer wavelengths). The spectra of light at the end of the fibre was then measured;

2. variation of pump (signal) power. The signal (pump) was kept fixed and pump (signal) energy was changed.

The setup for this purpose is shown in Fig. 3.3. CW output from two lasers was coupled together in a 90/10 ratio. A circulator was used to monitor any back-reflected power resulting from stimulated Brillouin scattering (SBS). SBS is a nonlinear process which arises due to backward light-scattering from a (longitudinal, forward-propagating) acoustic wave that is generated inside the fibre by a sufficiently strong electromagnetic wave [78]. Hence SBS is a self-

	N10	**P1**
Dispersion parameter, ps/(nm km)	−0.87	0.06
Dispersion slope, ps/(nm^2 km)	−0.0006	0.0035
Length, km	0.5	0.5
γ, 1/(W km)	20	20

Table 3.2. Dispersion properties for the N10 and P1 fibres at 1550 nm.

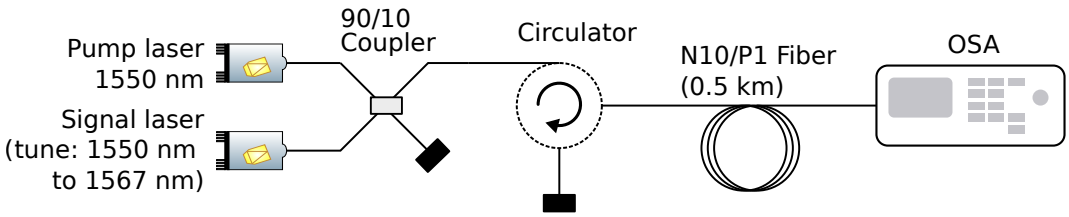

Figure 3.3. Setup for CW FWM in a single-mode fibre.

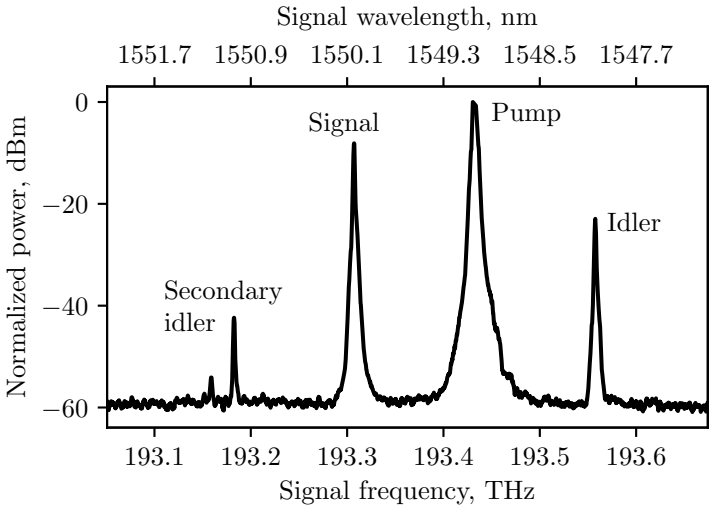

Figure 3.4. A typical measured trace of the spectrum at the output of the N10 fibre.

induced effect, and is automatically phase-matched such that the backscattered light is red-shifted by about 11 GHz in silica fibres [6]. For given input power, the intensity of SBS light increases exponentially with fibre length, and its strength is inversely related with effective area [77]. However, its onset can be suppressed by increasing the linewidth of input light, such as by frequency dithering or amplitude modulation [6], [78]. No SBS was observed in this experiment due to the low powers used.

Fig. 3.4 shows a typical spectral trace taken in order to study the FWM interaction. All four waves are evenly spaced in frequency and show varying levels of power. The global peak belongs to the pump wave, and the next highest is the signal. The power difference between them is $\approx 10\,\mathrm{dB}$ because of the 90/10 coupler being used. The ω_i idler is marked 'Idler'. The 'Secondary idler' also results from the same (pump-signal) inputs; this interaction is described by the exchange $\omega_s + \omega_s \rightarrow \omega_i + \omega_p$ and can be studied by similar methods (a more complete model would treat all processes simultaneously), but has been excluded from our study to focus analytically on the process at ω_i.

An important parameter that characterizes the strength of idler generation is conversion efficiency (CE), and is defined as the ratio of idler to input signal

power:

$$\text{Conversion efficiency (CE)} \equiv \eta = \frac{P_i(L)}{P_{s0}} = (\gamma P_{p0}/g)^2 \sinh^2(gz). \qquad (3.11)$$

The experimentally measured and calculated (via eq. (3.11)) variation of idler CE (at ω_i) with signal frequency is shown in Fig. 3.5(a) for both fibres. The 3 dB bandwidth of CE, defined as the detuning at which CE has dropped by 3 dB, is approximately 315 GHz and 1.37 THz for the N10 and P1 fibres respectively. The difference between these can be understood by closer examination of the role of the effective phase mismatch κ. Since $\kappa = \Delta k - 2\gamma P_{p0}$, an opposite (positive) contribution from Δk is required over a relatively large

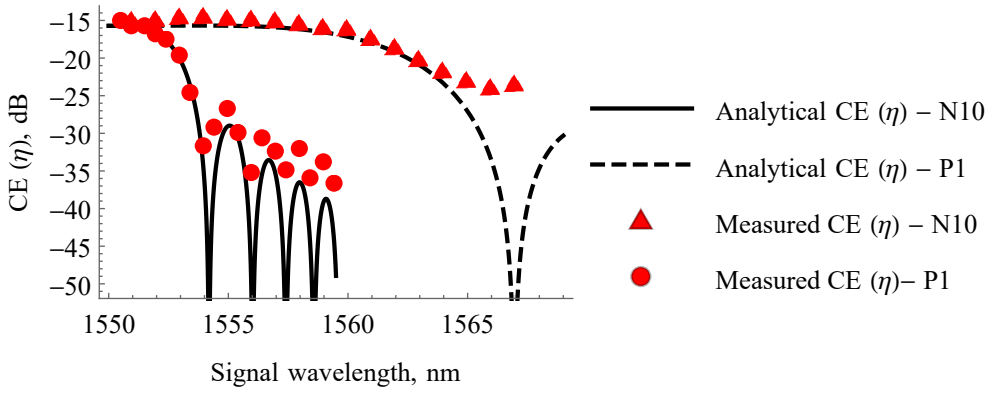

(a)

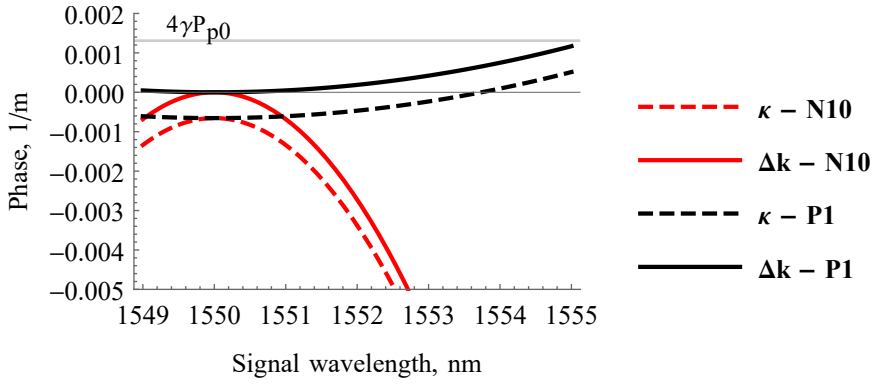

(b)

Figure 3.5. (a) Comparison of theoretical and measured conversion efficiency (η) for the N10 and the P1 fibre. (b) Phase mismatch parameters of the parametric interaction for both fibres.

range of signal wavelengths to compensate for the nonlinear phase mismatch $2\gamma P_{p0}$ in order to satisfy $\kappa = 0$. This is true for the case of the P1 fibre, as seen in Fig. 3.5(b), which shows plots for κ and Δk for both fibres using parameters listed in Table 3.2.[1] In general, lower (absolute) values of dispersion are associated with broader CE bandwidths [77].

For both fibres, the variation of idler power with signal and pump powers is shown in Fig. 3.6(a)-(b) and (c)-(d) respectively. The signal and pump wavelengths were fixed at 1551 nm and 1550 nm respectively. The slopes of the first two graphs (with a logarithmic-scale y-axis) under linear regression are both approximately 1, implying direct proportionality between idler power and input signal power. This behaviour can also be predicted by inspection of eq. (3.8), which implies that P_i should vary linearly with P_{s0} if other variables are held constant. For the case of pump power variation (graphs (c)-(d)), the slope is close to 2, implying that idler power varies as the square of pump

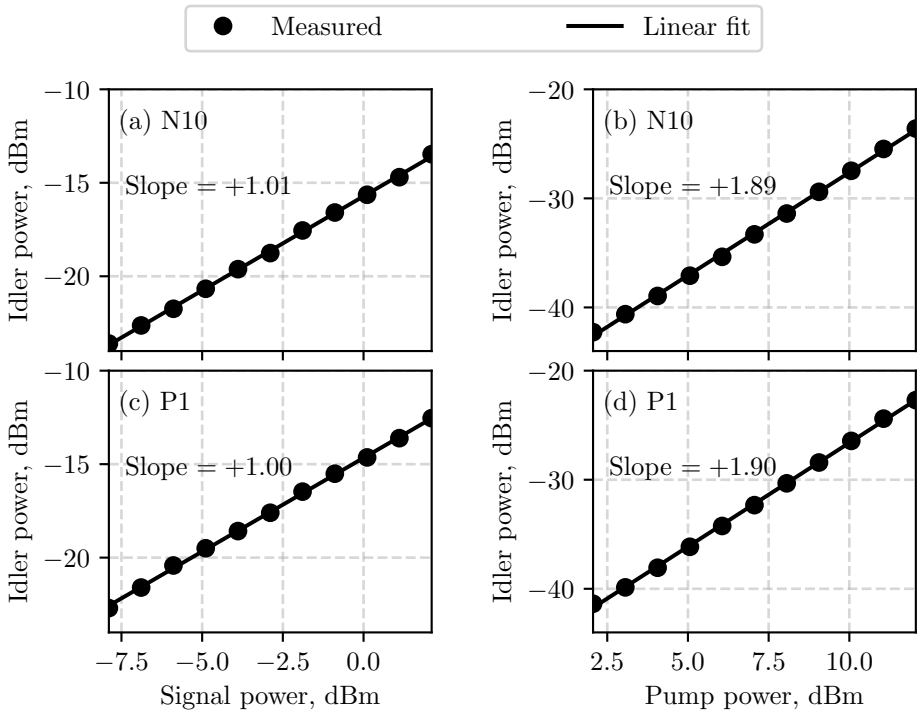

Figure 3.6. Dependence of the ω_i idler on (a) signal power and (b) pump power for the N10 fibre. (c)-(d): The same results for the P1 fibre.

[1]Only dispersion terms up to β_2 were taken into account in this calculation. This is accurate as long as we are away from the zero dispersion wavelength and signal to pump detuning is small [18].

power, which is not surprising given the degenerate role of the pump in the FWM process (see Fig 3.2). This also agrees with eq. (3.8), which can be used to verify the aforementioned quadratic relationship (see also [16]).

3.3 Intra-modal and inter-modal four-wave mixing in a few mode fibre

3.3.1 Theory

IM FWM refers to the case where the nonlinear interaction is between waves in two (or more) different non-degenerate modes. In so far as a basic theoretical treatment of inter-modal FWM is concerned, the procedure for obtaining the coupled differential equations involving modal amplitudes is identical [77]. Moreover, solutions that result from such a treatment are very similar in nature [79].

The example we shall be experimentally studying involves three (CW) input waves at distinct frequencies (in contrast to two inputs in the previous section) mixing to produce a fourth wave. Another difference is that these waves may have transverse profiles different from one another. To see how this affects the treatment of this subject, we now write the total electric field as the sum of four waves

$$\mathbf{E} = \frac{1}{2}\hat{\mathbf{x}} \sum_{j=p,q,s,i} E_j \exp i(\beta_j z - \omega_j t) + \text{c.c.}, \tag{3.12}$$

$$\mathbf{P}_{\text{NL}} = \frac{1}{2}\hat{\mathbf{x}} \sum_{j=p,q,s,i} P_j \exp i(\beta_j z - \omega_j t) + \text{c.c.}, \tag{3.13}$$

where p, q denote the pumps and s, i denote the signal and idler respectively.

Since each input may have a different intensity pattern, the E_j's (and P_j's) are now allowed to be different from one another. In this case, if we assume the frequency mixing relation $\omega_i = \omega_p + \omega_q - \omega_s$ the coupled equations describing

the evolution of the waves may be written as [77], [79], [80]:

$$\frac{\mathrm{d}A_p}{\mathrm{d}z} = i\frac{n_2\omega_p}{c}\left[\left(f_{pp}\left|A_p\right| + 2\sum_{j=q,s,i} f_{jp}\left|A_j\right|^2\right)A_p + 2f_{pqsi}A_q^* A_s A_i e^{-i\Delta kz}\right], \quad (3.13a)$$

$$\frac{\mathrm{d}A_q}{\mathrm{d}z} = i\frac{n_2\omega_q}{c}\left[\left(f_{qq}\left|A_q\right| + 2\sum_{j=p,s,i} f_{jq}\left|A_j\right|^2\right)A_q + 2f_{qpsi}A_p^* A_s A_i e^{-i\Delta kz}\right], \quad (3.13b)$$

$$\frac{\mathrm{d}A_s}{\mathrm{d}z} = i\frac{n_2\omega_s}{c}\left[\left(f_{ss}\left|A_s\right| + 2\sum_{j=p,q,i} f_{js}\left|A_j\right|^2\right)A_s + 2f_{sipq}A_p A_q A_i^* e^{i\Delta kz}\right], \quad (3.13c)$$

$$\frac{\mathrm{d}A_i}{\mathrm{d}z} = i\frac{n_2\omega_i}{c}\left[\left(f_{ii}\left|A_i\right| + 2\sum_{j=p,q,i} f_{ji}\left|A_j\right|^2\right)A_i + 2f_{ispq}A_p A_q A_s^* e^{i\Delta kz}\right], \quad (3.13d)$$

where the phase mismatch parameter $\Delta k = \beta_p^{\mathrm{Mode}(p)} + \beta_q^{\mathrm{Mode}(q)} - \beta_s^{\mathrm{Mode}(s)} - \beta_i^{\mathrm{Mode}(i)}$.

The resemblance of the above equations with eqs. (3.5) is clear; however, there are two main differences. One is that the dispersion properties of the modes can differ: this is reflected in the superscripts in the expression for Δk, which indicate the mode whose propagation constant is being considered. For example $\beta_p^{\mathrm{Mode}(p)}$ is the propagation constant of the mode in which pump p is launched at angular frequency ω_p. The other difference is that each term is now multiplied by factor given by the coefficient f whose subscript depends on the associated effect (intra- or inter-modal SPM/XPM/FWM). Specifically, these coefficients are calculated as

$$f_{abcd} \equiv \frac{\iint \mathrm{d}\mathbf{r}_\perp m_a m_b m_c^* m_d^*}{\left(\prod_{j=a,b,c,d}\iint \mathrm{d}\mathbf{r}_\perp \left|m_j\right|^2\right)^{1/2}},$$

with $f_{ab} = f_{aabb}$ [77]. Therefore, the magnitude of each of the aforementioned effects depends on the spatial overlap integral (f_{abcd}) of the participating modes.

Subject to the same basic assumptions used for eqs. (3.5), we can also find expressions for signal and idler power for the above case that are similar to those presented in Section 3.2.1 [79], [80]. The shortcoming here is that in practice, the analytical expressions for *inter-modal* interactions do not match the experimental data as well as we have previously shown in the case of

intra-modal FWM in Fig. 3.5(a) (see for instance [48]). The reasons for this mismatch will become clear as we study IM FWM effects in more detail in the following chapters.

One can in fact go further and derive more complex equations for the above case, depending on the physical features one wishes to incorporate. For example, a number of theoretical and computational efforts have been made in this area covering aspects such as random linear coupling, ultrashort pulse dynamics, mode profile dispersion and dispersion fluctuations [17], [44], [47], [81]–[84].

3.3.2 Inter-modal phase-matching with parallel IGV curves

To see how phase-matching may be achieved in the case of IM FWM, we make the theoretical case outlined above more concrete by specifying the input modes and their dispersion properties, and take the EC FMF characterized at the beginning of this chapter as our choice of waveguide. Specifically, we consider the case of IM FWM between the LP_{01} mode and the spatial modes of the LP_{11} mode group.

The wave configuration to be studied here is illustrated in Fig. 3.7. The pumps (namely Pump 1 and Pump 2) at frequencies ω_{p1} and ω_{p2} are in the LP_{01} and LP_{11a} modes respectively. The signal with frequency ω_s is in the same mode as Pump 1, i.e. LP_{01}. Given the inputs in this configuration, in general a number of FWM processes are possible, both intra- and inter-modal. For reasons that will become clear shortly, we choose to focus on the inter-modal processes at frequencies ω_{BS} and ω_{PC}. The former process is named Bragg scattering (BS). This terminology is taken from the spatial interpretation of the

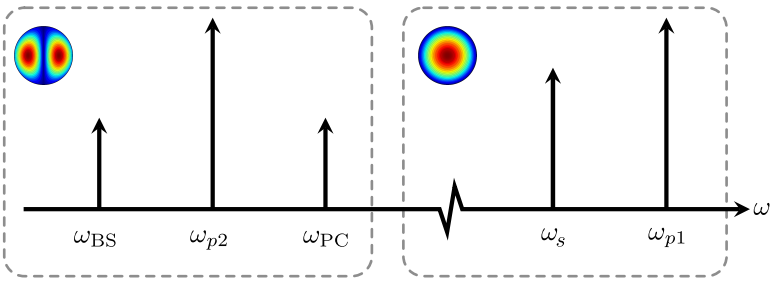

Figure 3.7. Wave configuration for the processes defined as Bragg scattering (BS) and phase conjugation (PC).

FWM process: two strong inputs, i.e. the pumps, form a (moving) refractive index grating and the (weaker) signal scatters/diffracts to produce a fourth wave, namely the idler [85]. BS is described by the interaction given by the relation $\omega_{p2}+\omega_s = \omega_{\mathrm{BS}}+\omega_{p1}$, in which an idler photon is created for every signal photon destroyed. The process at ω_{PC} is termed phase conjugation (PC). It involves the interaction with $\omega_{p1}+\omega_{p2} = \omega_{\mathrm{PC}}+\omega_s$, in which pump (signal and idler) photons are annihilated (created) in pairs.

The phase mismatch parameter for the BS process may be written by Taylor expanding the propagation constants around a nearby frequency ω_0 as

$$\begin{aligned}\Delta k &= \beta^{(11\mathrm{a})}\left(\omega_{\mathrm{p2}}\right)+\beta^{(01)}\left(\omega_{\mathrm{s}}\right)-\beta^{(11\mathrm{a})}\left(\omega_{\mathrm{BS}}\right)-\beta^{(01)}\left(\omega_{\mathrm{P1}}\right)\\ &\approx\Bigg[-\beta_2^{(11\mathrm{a})}\left(\frac{\omega_{\mathrm{BS}}+\omega_{\mathrm{p2}}}{2}-\omega_0\right)-\beta_1^{(11\mathrm{a})}(\omega_0)\\ &\quad+\beta_2^{(01)}\left(\frac{\omega_{\mathrm{p1}}+\omega_{\mathrm{s}}}{2}-\omega_0\right)+\beta_1^{(01)}(\omega_0)\Bigg]\times\left(\omega_{\mathrm{s}}-\omega_{\mathrm{p1}}\right), \qquad (3.14)\end{aligned}$$

where $\beta_n^{(m)}(\omega_0)$ is the n-th derivative of the propagation constant of mode m evaluated at frequency ω_0.

By inspection of eq. (3.14), it can be observed that the sum of the first (last) two terms in square brackets equals the negative (positive) IGV evaluated at the average of the idler and Pump 2 (signal and Pump 1) frequencies. $\Delta k = 0$ when the magnitude of these IGVs is equal. Hence, it is expected that the interaction for the BS process will be 'automatically' phase-matched to the extent that the RIGV curves of the interacting modes are parallel. This can be seen from Fig. 3.8, which shows that when the signal is tuned, the mismatch is still zero. This is because when the idler frequency shifts to satisfy energy conservation, so does the condition for optimum idler generation: phase matching is satisfied for conversion of the new (tuned) signal *as well* because the IGVs at the new average frequencies are also equal.

If the IGV curves are not parallel, the CE will degrade with signal detuning from pump. Note also that the condition for automatic phase matching is not satisfied for the phase conjugation (PC) process.

By comparing Fig. 3.1(d) with Fig. 3.8, it can be seen that for the FUT, the IM FWM BS process involving modes LP_{01} and $\mathrm{LP}_{11\mathrm{a}}$ ($\mathrm{LP}_{11\mathrm{b}}$) will be phase-matched when Pump 1 is detuned from Pump 2 by about 25 nm (40.6 nm). This detuning is simply the horizontal separation between the relevant IGV curves.

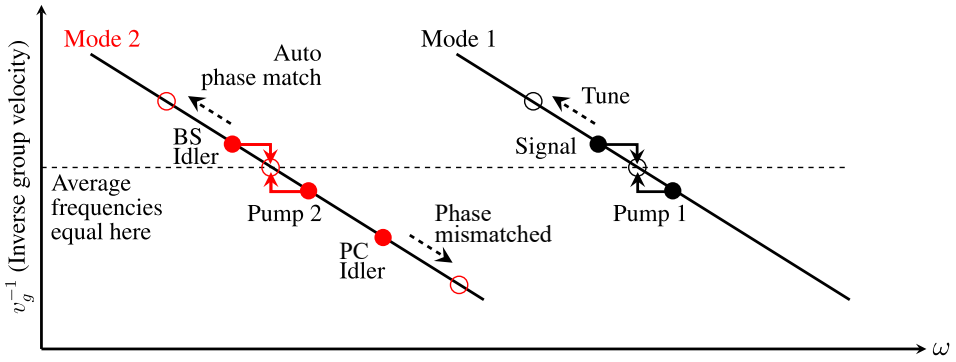

Figure 3.8. Phase matching for the Bragg scattering and phase conjugation processes. For the Bragg scattering process, changing the signal wavelength preserves phase matching. The phase conjugation process remains non phase matched.

Section 3.3.4 is devoted to an experimental validation of the scheme considered above. Before that, we will briefly take a look at intra-modal FWM in our EC FMF.

3.3.3 Experiment: intra-modal FWM

Intra-modal FWM for the modes of the EC FMF was individually characterized first. The experimental setup employed for this purpose is shown in Fig. 3.9. Input light was amplified by using a (fixed output power) erbium-doped fibre amplifier (EDFA). To suppress SBS and to increase peak power

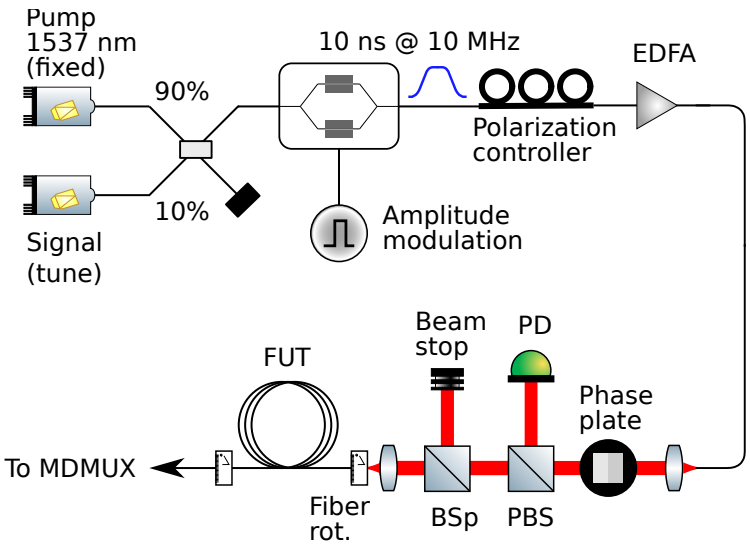

Figure 3.9. Setup for intra-modal FWM measurements.

after amplification, the input was time gated using a Mach-Zehnder modulator (MZM) for amplitude modulation to produce a train of 10 ns pulses at 10 MHz. The average power at the input to the FUT was set to 20.5 dBm. All modes had the same polarization at the input facet of the fibre. Since the LP_{11a} and LP_{11b} modes have spatial profiles orthogonal to each other, a mode demultiplexer (MDMUX) based on the same principles discussed in the previous chapter was used (see Fig. 2.8 and associated text).

By using the dispersion for each mode measured by the time-of-flight method (see Table 3.1), it was also possible to analytically compute the intra-modal FWM behaviour of the FUT. The combined results for all three modes, experimental and analytical, are shown in Fig. 3.10, and the measurements shown follow closely the pattern predicted by scalar single-mode FWM theory. In analytical calculations, input power was normalized to take into account the 10% duty cycle, and for LP_{01}, a value of $\gamma_{LP_{01}} = 0.73/(\mathrm{W\,km})$ was used.[2]

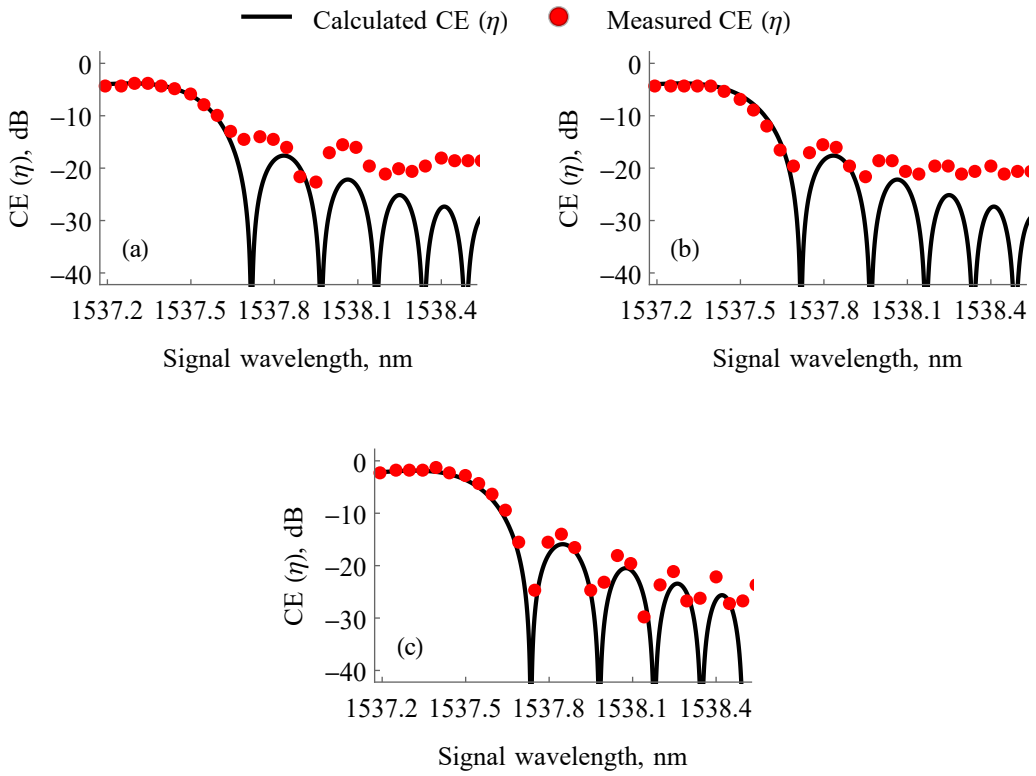

Figure 3.10. Measured and calculated intra-modal FWM conversion efficiency versus signal-pump detuning for the modes of the elliptical core few-mode fibre: (a) LP_{11a} (b) LP_{11b} and (c) LP_{01}.

[2]This is very close to the simulated value of $0.7/(\mathrm{W\,km})$, which is based on computational

$\gamma_{\mathrm{LP11}} = 0.6/(\mathrm{W\,km})$ for both HOMs, which is lower than γ_{LP01} as expected, because the effective areas of the HOMs are generally larger than that of the fundamental mode.

3.3.4 Experiment: IM FWM with pumps in different modes

First, we describe the setup used for achieving IM FWM between modes LP_{01} and LP_{11a}. Multiplexing of the modes was achieved using the setup in Fig. 3.11. Three continuous-wave tunable lasers were used to generate the two pumps and the signal. Pump 1 was kept at 1537.4 nm and Pump 2 at 1562.4 nm (hence a detuning of 25 nm, as discussed above). The signal was tuned away from Pump 1 and CE measurements were taken. As before, to obtain high peak power (after amplification) and to avoid SBS, all three sources were gated with a 10% duty cycle at a repetition rate of 10 MHz, following which they were adjusted for temporal overlapping at the fibre input. As per the configuration in Fig. 3.7, Pump 1 and the signal were launched in the fundamental mode while Pump 2 was launched in the LP_{11a} mode by use of a PP. A PBS and polarization controllers were used to ensure that all inputs were co-polarized. The average input power of each pump was 20.5 dBm, with signal power about 10 dB lower.

The MDMUX consisted of three ports,[3] each one optimized for gathering

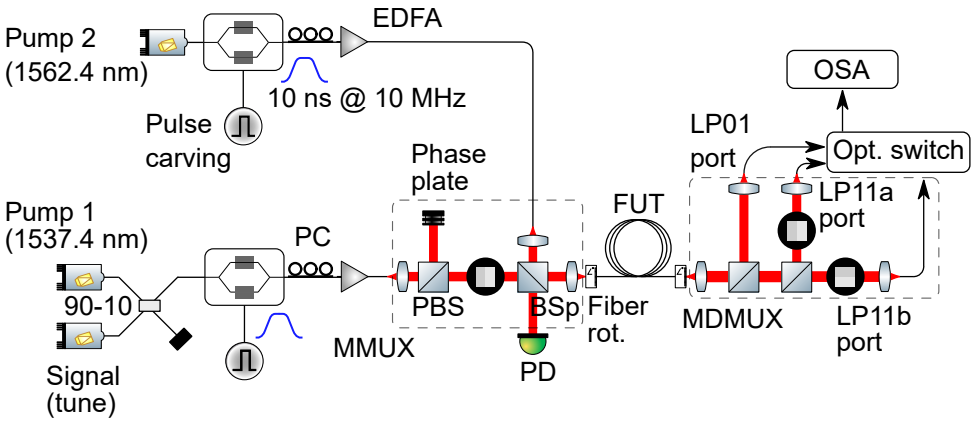

Figure 3.11. Setup for the multiple-mode pumps configuration.

work by Prof. Peter Horak in [81].

[3]The results reported in this chapter only cover the interaction between modes LP_{01}

light in a given spatial mode. The first beam-splitter (see Fig. 3.11) was used to direct the output of the FMF to a SMF, which automatically filtered out the HOMs and efficiently coupled LP_{01} light. For the HOMs, a second beam-splitter directed the remainder of the output light through two perpendicularly oriented PPs, which by the principles presented in Chapter 2 allowed efficient collection of light in either LP_{11a} or LP_{11b}. All three ports were fed to an optical switch whose output was directed to an OSA. The switch was then used to select the mode/port whose spectrum was to be measured.

Results obtained using the setup above will be discussed in the remainder of this section. Fig. 3.12 shows typical spectral traces of the LP_{01} and LP_{11a} MDMUX ports that were measured using the setup above. The spectrum for each port is normalized to pump power in that mode (assumed equal for both ports), and the pumps are separated by 25 nm (other values of pump separation yielded lower IM FWM efficiency). It can be observed that the LP_{01} port accepts inputs launched in the LP_{01} mode (i.e. Pump 1 and the signal) and suppresses light from the other mode (Pump 2 was in LP_{11a}). A similar statement can be made regarding the LP_{11a} port. Any stray light belonging to the other mode at a given port is labelled as 'leakage' in Fig. 3.12.

The signal to Pump 1 detuning in the spectra shown in Fig. 3.12(a) is 0.5 nm, whereas in Fig. 3.12(b) it is increased to 1.5 nm. At the LP_{01} port, the line labelled MI (short for modulation instability) was the result of an intra-modal interaction between Pump 1 and the signal. For the LP_{11a} port, the BS and PC idlers were located symmetrically around Pump 2. The additional tones surrounding them were generated by a combination of the intra-modal and IM FWM processes resulting from the primary input waves.

As the signal was detuned away from the pump, the efficiency of the observed nonlinear interactions diminished. The CEs of the PC and BS interactions for a range of signal wavelengths are shown in Fig. 3.13. CE was calculated as $\left(P_{BS}^{LP11}/P_{Pump2}^{LP11}\right) / \left(P_{S}^{LP01}/P_{Pump1}^{LP01}\right)$ where P_{a}^{b} is the power of wave 'a' in mode 'b' (this uses the fact that both pump powers are equal). The maximum CE was observed to be −2.55 dB and −3.77 dB for the BS and PC processes respectively and occurred at a signal wavelength of approximately 1538.1 nm for both processes. CE bandwidths (at the −6 dB point) of about

and LP_{11a}, therefore only two ports are really needed. However, we also include the LP_{11b} port here for completeness.

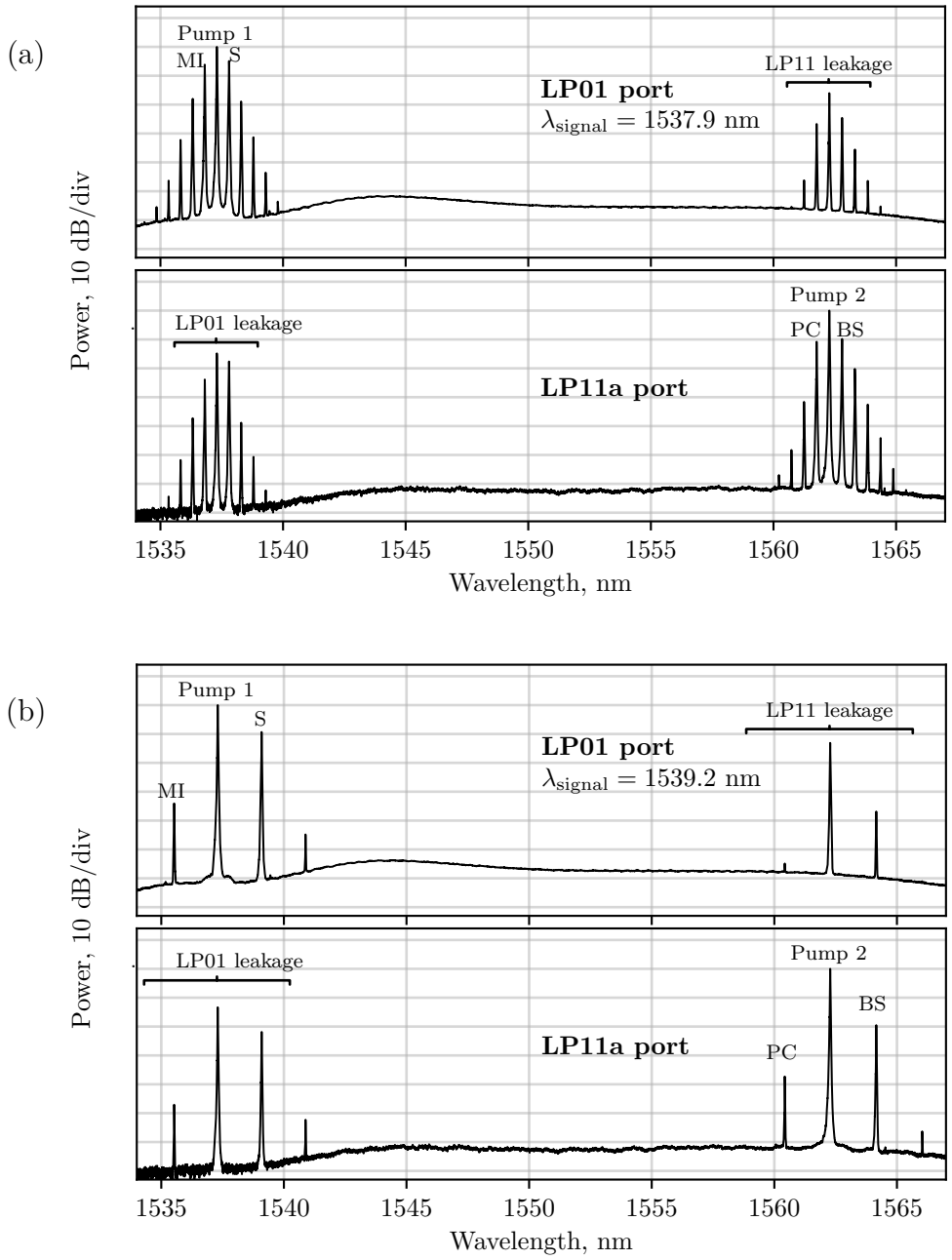

Figure 3.12. (a). An OSA trace for each MDMUX port for signal to Pump 1 detuning of 0.5 nm. (b) An OSA trace for each MDMUX port for signal to Pump 1 detuning of 1.8 nm.

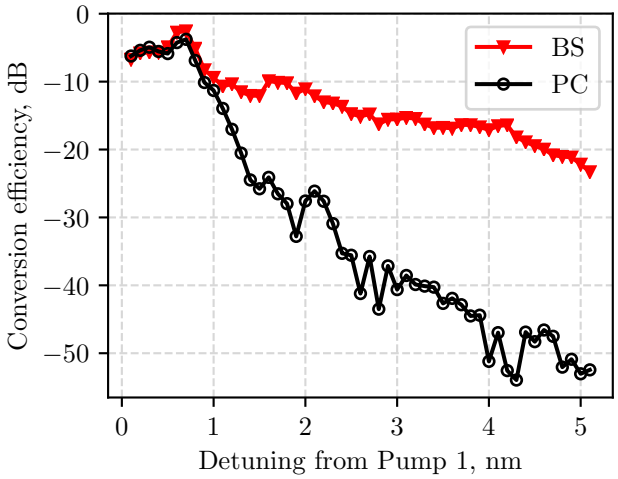

Figure 3.13. Conversion efficiency of BS and PC processes versus signal to Pump 1 detuning.

2 nm and 0.9 nm were observed for the BS and PC processes respectively.[4] This is consistent with the discussion relating to phase-matching earlier, according to which only the BS process should be 'automatically' phase matched for larger values of detuning.

3.4 Conclusions

Intra- and inter-modal FWM are both potential means for the implementation of signal processing functionalities in optical communications. We have investigated the use of each of these for performing wavelength conversion, and have characterized their CE bandwidths. We also pointed out the role played by the dispersion parameter in the FWM process, and at the outset of this chapter discussed an experimental method for determining the dispersion of the modes of a FMF.

In the case of intra-modal FWM, the configuration was that of a single-pump parametric amplifier [77]. For single mode FWM, we showed that a lower value of dispersion is required for broadband operation.

In contrast to the above, phase-matching for IM FWM (in the specific configuration presented) did not require a particular value of dispersion. Rather,

[4] As will be discussed in Chapter 5 in detail, low CE bandwidths arise primarily from fibre non-uniformity and the resulting dispersion fluctuations.

the phase-matching condition placed a constraint on the *relative* rate of change of inverse group velocity between the two interacting modes: dispersion has to be equal for the two modes regardless of its absolute value. However, significantly higher powers had to be used to achieve comparable idler generation, and this also necessitated the use of an SBS suppression scheme. In addition, the CE bandwidths obtained for IM FWM were much lower compared to the single mode case, despite the promise of 'automatic' phase matching. We discuss the reasons for these shortcomings as we study IM FWM in more detail in the following chapters. We will also discuss the extent to which they may be overcome, and how IM FWM could be used to provide functionality that would otherwise be exceedingly difficult to implement in single mode waveguides.

Chapter 4

Polarization effects in intermodal four-wave mixing Bragg scattering

One aspect of IM FWM that has not received attention so far in this work has been the role of the SOPs of the interacting waves. The simple analytical treatment given in Chapter 3 treats the fields as scalar quantities, and the experimental studies ensure linearly co-polarized inputs by use of either PM components or a combination of polarization controllers and a PBS. Further, a matter that has been taken for granted so far has been the assumption of a fibre as a perfectly uniform waveguide along its length. It turns out that this assumption is not entirely valid in reality [58]. Indeed, these issues have been the subject of detailed theoretical and experimental study in the context of FWM in SMFs, and may have important implications for devices utilizing IM FWM for signal processing applications. This chapter looks at these previously unconsidered but practical aspects of the IM FWM interaction.

In relation to the above, we firstly investigate the dependence of IM FWM on signal polarization. We demonstrate that, if the pumps are co-polarized, the idler power is largely independent of the input signal polarization in both a 1 km and a 50 m long fibre. We attribute this polarization insensitivity to the non-uniformity (whose nature we elaborate on later) of the fibre under investigation. Secondly, the influence of the relative polarization state between the pumps (i.e. pumps with the same or orthogonal SOPs) on signal wavelength conversion is investigated, and is found to be significant.

4.1 Input scheme

In Chapter 3, it was demonstrated that the generation of new frequencies via FWM could be achieved by excitation in two different spatial fibre modes at the phase-matched frequencies. A three mode elliptical core fibre was used for that purpose, with a pump and a signal in the fundamental mode and the second pump in the LP_{11a} mode. The configuration also resulted in mode conversion: IM FWM resulted in idler generation in the LP_{11a} mode.

In this chapter, we employ the same fibre with a different input configuration: both pumps will now be in the fundamental mode and the signal will be in a higher-order mode. We will see that idler generation in this case occurs in the same mode as the signal, a property useful in cases where mode conversion is not desired.

In the new configuration, the frequencies of the interacting waves are detailed in Fig. 4.1. In order to facilitate the discussion afterwards relating to polarization, both the x and y components of the field are shown. For example, p_{x1} (p_{y2}) denotes the x (y) component of Pump 1 (Pump 2). Similarly, s and i denote the signal and the idler. As indicated by the spatial mode profile within each dashed box in Fig. 4.1, the two pumps now excite the same spatial mode (LP_{01}) while the signal and the generated idlers propagate in a different mode (either LP_{11a} or LP_{11b}).

ω_{BSr} and ω_{BSb} denote the red-shifted and blue-shifted idlers respectively.[1]

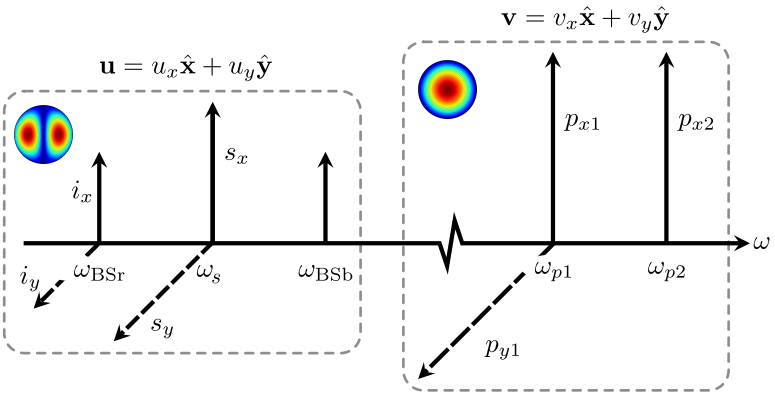

Figure 4.1. Schematic of the wave configuration and wavelength allocation of the IM FWM processes.

[1] In the text, ω may be replaced with λ when specifying wavelength instead of frequency.

Momentum conservation dictates that

$$\omega_{\mathrm{BSr}} = \omega_s - (\omega_{p2} - \omega_{p1}) \tag{4.1}$$

$$\omega_{\mathrm{BSb}} = \omega_s + (\omega_{p2} - \omega_{p1}), \tag{4.2}$$

so the idlers will be equally spaced around the signal in frequency. Note that both idlers are now of the Bragg scattering type. This is because both interactions involve photon exchange in which $\omega_s + \omega_{p_i} \rightarrow \omega_{\mathrm{BS}} + \omega_{pj}$, implying that an idler photon is created for each signal photon that is destroyed, a characteristic feature of Bragg scattering frequency translation [85].

It should be noted that this scheme does not require the zero dispersion wavelength to take a specific value, as is needed for phase-matching in single-mode systems. Waveguide designs incorporating high dispersion could therefore be used to suppress FWM induced signal-to-signal crosstalk. Moreover, by engineering the IGV curves of HOMs and their relative frequency separations, the signal could be placed far away from the pumps, thereby preventing contamination by undesired amplified spontaneous emission (ASE) noise associated with high pump powers or by Raman effects.

4.2 Experimental setup and results

The experimental setup used to explore IM FWM in the input configuration of the pumps and the signal (see Fig. 4.1) is shown in Fig. 4.2. This Figure shares many similarities with Fig. 3.11, but there are two exceptions: i) the signal and Pump 2 positions are exchanged and ii) the phase plate is moved to the path of the signal. Therefore, the pumps (now in the same mode) were coupled together before being launched into the pulse carver. All three sources were similarly gated as before. The amplifier output was set to provide 20.5 dBm of average power per pump, as measured at the input to the fibre. The signal was typically kept 15 dB lower. The PBS was used to ensure that the pumps were co-polarized.

Based on earlier characterization of this fibre (see Chapter 3), it is known that when λ_{p2} is set to 1537.4 nm, phase-matching for the BSr idler occurs when:

A: $\lambda_s = 1562.4$ nm for a signal in the $\mathrm{LP}_{11\mathrm{a}}$ mode.

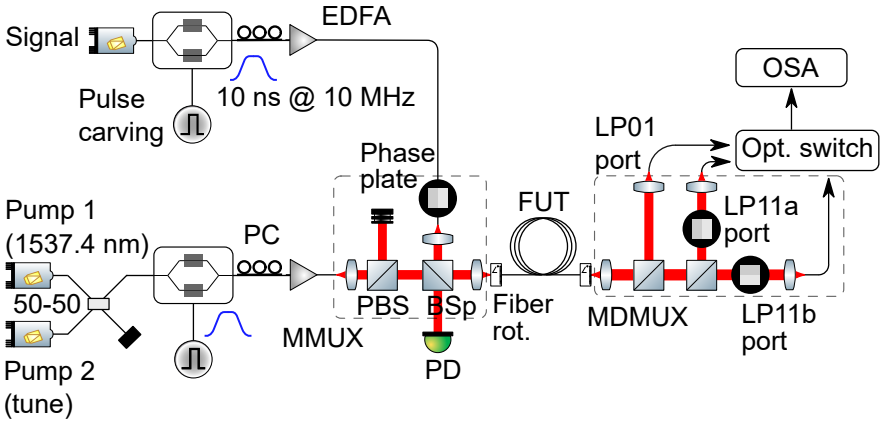

Figure 4.2. Experimental set-up of inter-modal FWM in the three-mode EC FMF under the SMPC.

B: $\lambda_s = 1578\,\text{nm}$ for a signal in the $\text{LP}_{11\text{b}}$ mode.

Using these input specifications, output spectra were obtained at the corresponding MDMUX LP_{11} ports to measure conversion efficiency. A typical spectrum for case A (B) above is shown in the top (bottom) part of Fig. 4.3. Pump to pump detuning here is 0.2 nm, i.e. $\lambda_{p1} = 1537.6\,\text{nm}$. If the pumps are off, only a single line (red) belonging to the signal is visible. With the pumps on, the spectra show the signal and the corresponding cascaded IM FWM idlers that appear in the $\text{LP}_{11\text{a}}$ or $\text{LP}_{11\text{b}}$ mode, producing a comb of lines around the input signal in the C or L-band (respectively). Additionally, intra-modal FWM associated with the two higher power pumps results in the generation of idlers in the fundamental mode, and leaks into the MDMUX ports (labelled as 'LP_{01} leakage' in Fig. 4.3).

4.2.1 Signal polarization and conversion efficiency bandwidth

Fig. 4.4 gives a closer look at the comb of tones that is generated around the signal in the $\text{LP}_{11\text{b}}$ mode, when pump to pump detuning is 0.5 nm. The comb spans a bandwidth of approximately 5 nm, with idler optical signal-to-noise ratio (OSNR) up to 40 dB. Two spectra are presented: the 'Co-pol' spectrum refers to the case when signal SOP was aligned (using a PBS) with that of the already co-polarized pumps at the fibre input facet. With reference to

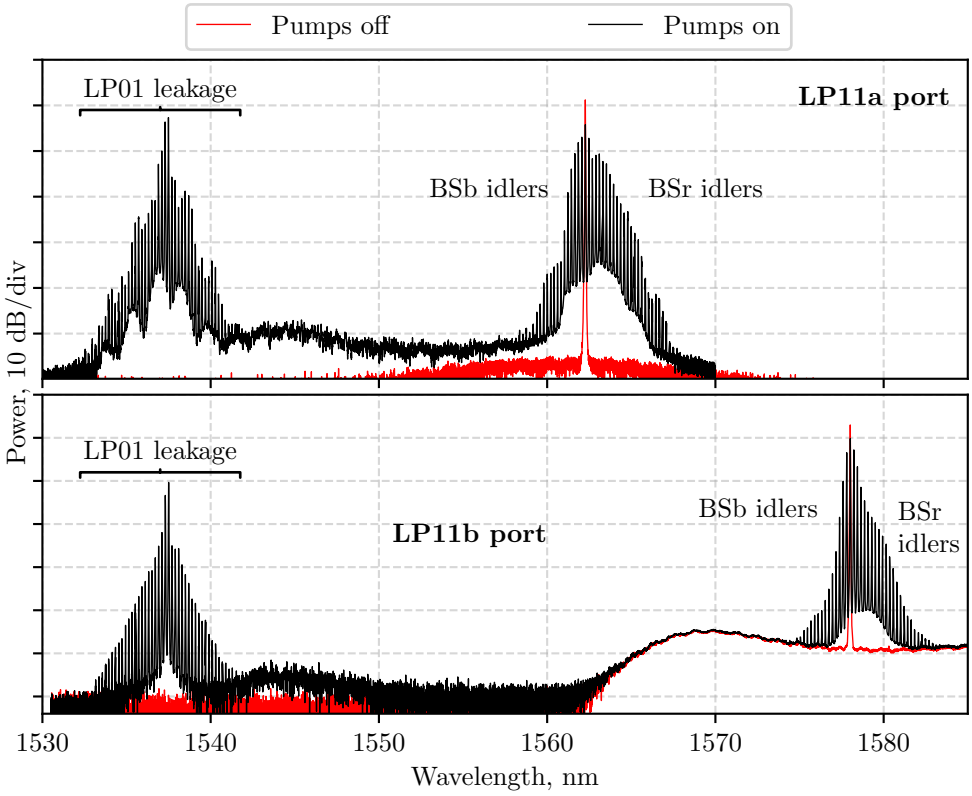

Figure 4.3. Spectral traces obtained using the SMPC.

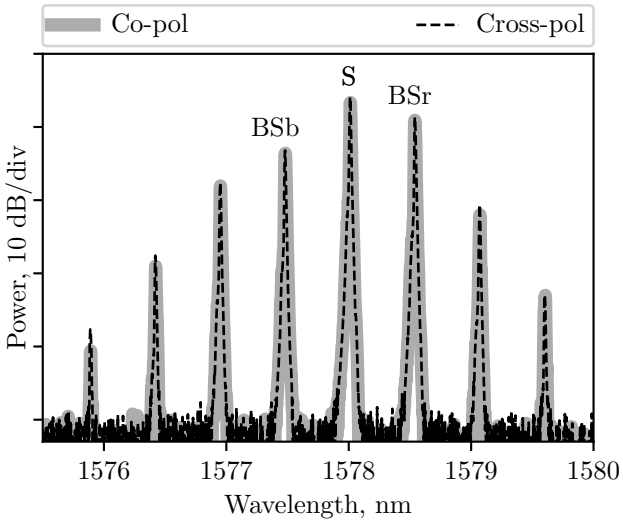

Figure 4.4. IMFWM induced lines are generated around the signal. Shown above is the LP_{11b} mode, with a pump to pump detuning of 0.5 nm.

Fig. 4.1, the input configuration would consist of waves $\{s_x\,, p_{1x}\,, p_{2x}\}$ and the idler would therefore be i_x. On the other hand, 'Cross-pol' shows the $\mathrm{LP}_{11\mathrm{b}}$ spectrum in the case when the signal was orthogonally polarized with respect to the pumps (with input waves $\{s_y\,, p_{1x}\,, p_{2x}\}$ and idler being i_y).

Negligible difference was observed in idler CE between the two cases of signal polarization shown, which implies polarization insensitive Bragg scattering. Qualitatively similar behaviour was observed in $\mathrm{LP}_{11\mathrm{a}}$ spectra as well.

The fact that idler generation is independent of signal polarization can be advantageous. This is because in a fibre based communications network it is not in general possible to control the polarization of an incoming signal, which varies with time. A polarization dependent wavelength converter would therefore randomly modulate the intensity of the converted signals, which would be undesirable.

At larger pump to pump detuning, BSr idler generation dominated. Fig. 4.5 shows (normalized) spectra at each of the MDMUX ports for the case of 2.5 nm detuning. The phase-matched BSr idlers in both LP_{11} modes are about 20 dB stronger than the non-phase-matched BSb, implying that this wavelength conversion scheme can allow efficient and controlled conversion between specified

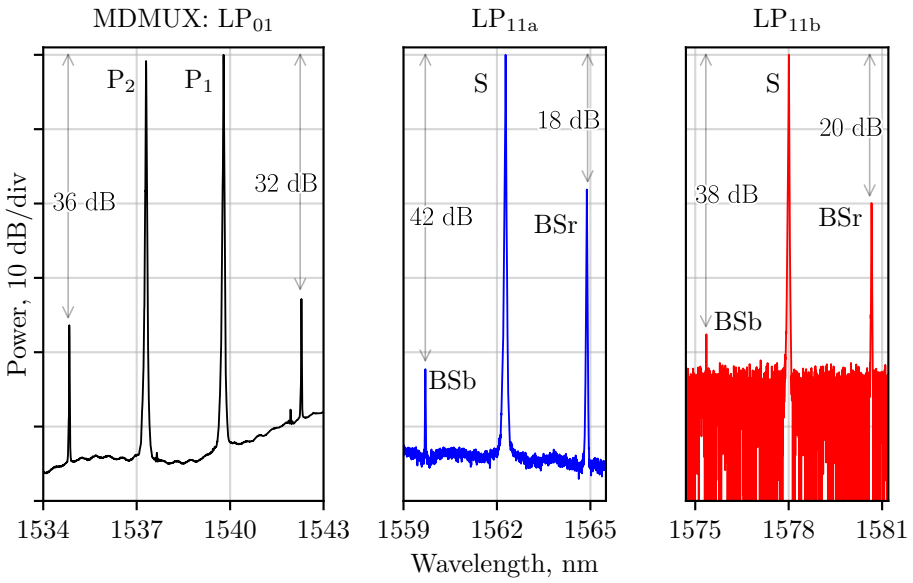

Figure 4.5. A composite of normalized spectra after 1 km of FUT, collected at the LP_{01}, $\mathrm{LP}_{11\mathrm{a}}$ and $\mathrm{LP}_{11\mathrm{b}}$ MDMUX output ports with signal wavelengths of 1562.4 nm and 1578 nm and pump-to-pump detuning of 2.5 nm.

wavelength channels. This could have a clear benefit in terms of avoiding contamination of the signal with undesired generated idlers that may eventually overlap with other signals (usually referred to as nonlinear cross-talk), if wavelength division multiplexed signals were to be considered.

Next, the conversion efficiency (CE) as a function of pump-to-pump wavelength detuning was measured for both the LP_{11a} and LP_{11b} modes. This would give the bandwidth of the CE, i.e. how far in wavelength the signal can be converted until a given amount of CE is lost due to the phase-mismatch of the nonlinear process. CE was calculated as the power difference (in dB) between the generated idlers at the output of the FUT and the input signal.

The combined results for the 1 km fibre are presented in Fig. 4.6. The top (bottom) figures (a)-(b) ((c)-(d)) show the graphs of CE versus pump-to-pump detuning for the red-shifted (blue-shifted) Bragg scattering idler for the LP_{11a} and LP_{11b} modes respectively. As expected, for both modes the phase-matched BSr process showed a broader bandwidth (almost 2 nm at −6 dB for the LP_{11a} mode) than the BSb process (about 1 nm at −6 dB for the LP_{11a} mode) with

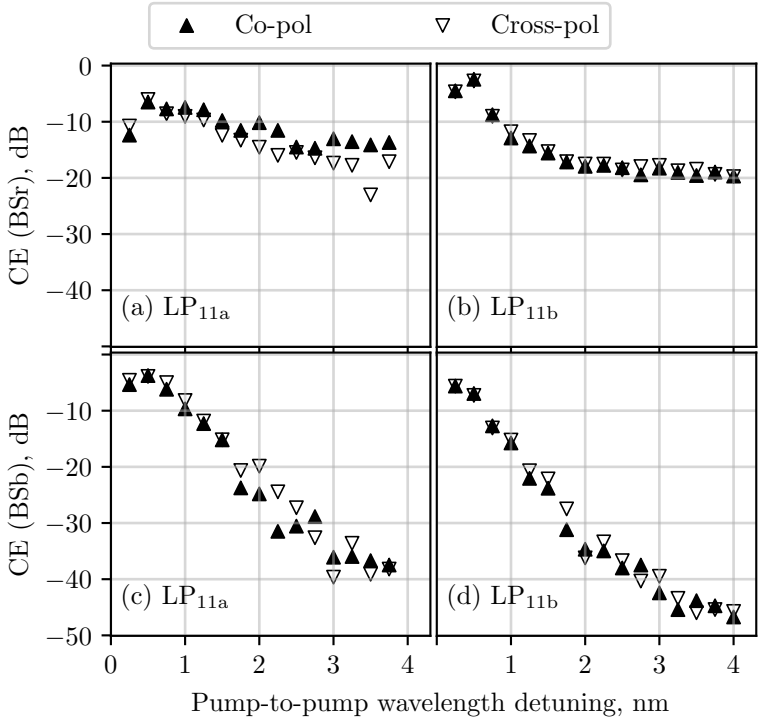

Figure 4.6. (a) and (b) show the CEs of the BSr process in the 1 km fibre for the LP_{11a} and LP_{11b} modes, respectively. (c) and (d) show CEs of the BSb process in the 1 km fibre for the LP_{11a} and LP_{11b} modes, respectively.

a maximum CE of about −2.5 dB for both cases.

Importantly, the CEs for both processes were found experimentally to be largely independent of the signal polarization. Apart from a couple of outliers, the largest difference in CE between the co- and cross-polarized cases was 2 dB, further reduced to 0.7 dB when lower pump powers (15 dBm per pump) were used (not shown here). The CE variation between the co/cross cases was lowest near phase matching and deteriorated as pump to pump detuning increased. This small CE difference and its power dependence may be due to drifts of the polarization between the pumps and the modal purity during the experiment, which are more severe at higher pump powers. Note that the experimental results were obtained in a stable and repeatable manner over time, in contrast to the observations in [86], where power fluctuations of the idlers generated by these processes were noted.

Similar CE measurements were carried out using a shorter length (50 m) of the same fibre and using the same launch powers for the pumps and signal. The corresponding results for the LP_{11a} and LP_{11b} modes are reported in Fig. 4.7.

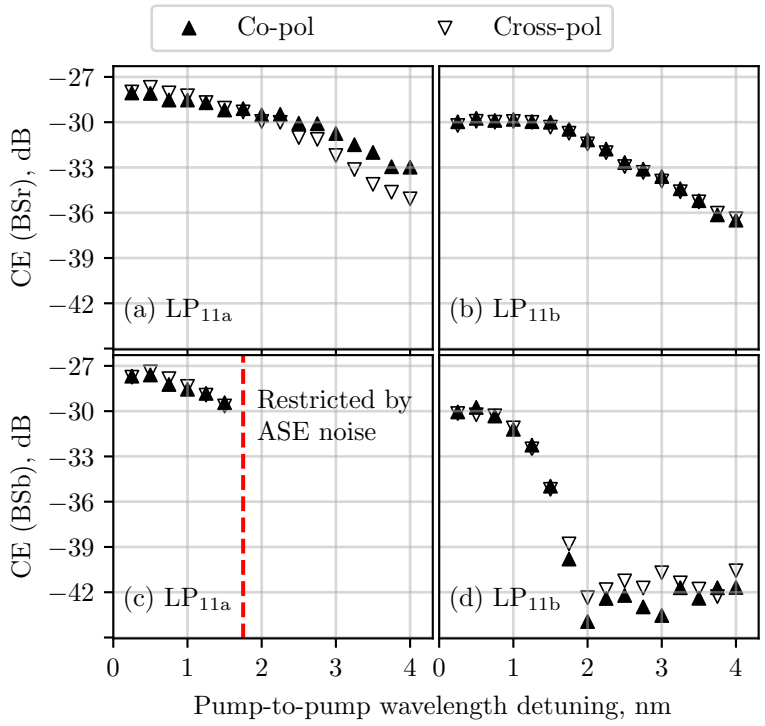

Figure 4.7. (a) and (b) show CEs of the BSr process for the 50 m fibre modes LP_{11a} and LP_{11b}. (c) and (d) show CEs for the BSb processes for these modes.

The maximum CE drops to about −28 dB in this case because of the shorter interaction length available, but the −6 dB bandwidth of the BSr increases to about 3 nm. These results highlight that when fibre length is varied, this multi-mode wavelength converter experiences a trade-off between gain (CE) and gain bandwidth similar to single-mode devices, where bandwidth varies inversely with length while CE scales exponentially with it [77].

Fig. 4.7 also makes it clear that even in this shorter length fibre, the independence of CE with respect to signal polarization is maintained. The maximum CE variation with the SOP of the signal is about 1 dB.

4.2.2 Conversion efficiency for co- and cross-polarized pumps

Finally, we studied the influence of the SOP of the pumps with respect to each other on the IM-FWM process using the 1 km long fibre. Specifically, the pumps were set to be either (linearly) co-polarized or orthogonally polarized to one another at the input of the fibre. For this part of the experiment, the pump pulse-carvers and the PBS were removed and a third polarization controller was added in one of the pump arms. This represented the simplest modification of the set-up for this purpose.

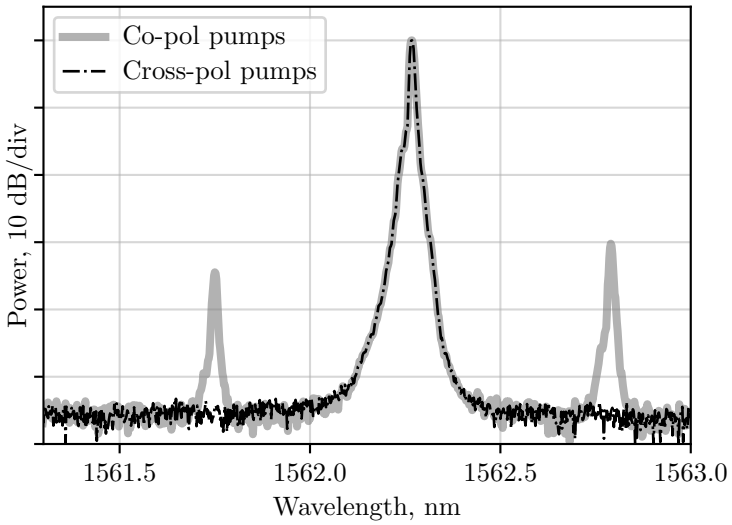

Figure 4.8. IM FWM spectra at the LP_{11a} MDMUX output port for co-polarized and cross-polarized pumps.

With reference to Fig. 4.1, now the inputs to the fibre are the waves $\{s_x + s_y,\, p_{x1} \text{ or } p_{y1}\,, p_{x2}\}$. The corresponding IM FWM output spectra for these inputs are reported in Fig. 4.8, when the signal excites the $\mathrm{LP}_{11\mathrm{a}}$ mode and the pump-to-pump wavelength detuning was set to 0.5 nm. If the pumps were orthogonally polarized ('cross-pol pumps'), no observable IM-FWM idlers were generated, regardless of the state of the signal polarization. This was not the case for co-polarized pumps, where a CE of about −30 dB was observed with an optical signal to noise ratio better than 20 dB.

4.3 Analysis

This section presents an analysis of the polarization insensitive nature of IM FWM observed earlier and summarized graphically in Figs. 4.6 and 4.7. The description of a fibre as a 'uniform' waveguide was called into question at the introduction of this chapter; we start by elaborating on this topic below and specify its role in linear mode coupling. Then, we define the two length scales necessary for our analysis: these are the fibre correlation length and (birefringence) beat length. Finally, we present a condensed theoretical treatment that relies on these concepts and agrees well with the measured results.

As mentioned in Chapter 2, even circularly designed (and fabricated) fibres cannot be treated as isotropic waveguides. A basic reason for this is fabrication imperfections: even in highly controlled production settings it is difficult to avoid very small deviations from a perfectly cylindrical geometry of constant radius. Besides that, environmental factors encountered in the majority of practical situations induce (time varying) mechanical perturbations such as temperature variation and stress randomly distributed along the length of the fibre.

While we cannot calculate deterministically the exact field along a fibre that exhibits such random axial asymmetry, it is possible to capture qualitative and quantitative aspects of linear and nonlinear propagation by considering the physical effects of these perturbations. One fundamental effect is the occurrence of a small *residual* birefringence in the fibre. This breaks the (complete) degeneracy of the polarization modes of the fibre so that two axes, fast and slow, with nearly equal but not identical propagation constants can be presumed. Since the polarization modes along these two axes are nominally distinct, we refer to these as quasi-degenerate modes. For example, LP_{01x} and

LP_{01y}, representing the x and y polarizations of the fundamental mode, are quasi-degenerate.

The random nature of optical fibres described above results in the occurrence of linear mode coupling among the quasi-degenerate modes within the fibre's mode groups (these may be two- or four-fold degenerate as discussed in Chapter 2). Mode coupling refers to the exchange of power between these modes, and linear refers to the fact that this (coupling) phenomenon can be explained by assuming a linear dielectric response to an applied electromagnetic field [78]. We refer to this type of energy exchange as *intra-group* coupling. Intra-group coupling may be significant even in the presence of small perturbations. In fact, the efficiency with which power transfers from one mode to another over a fixed perturbation length is strongly connected to two factors [56]:

1. the difference in the propagation constants of the two modes (denoted by $\Delta\beta$ for this discussion) having dimensions of 1/length, and

2. the spatial frequency components of the perturbation (with same dimension as $\Delta\beta$). So, if the perturbation results from an irregular fibre-core radius, these would be the components of the Fourier transform (denoted $R(k)$ where k is the frequency variable) over length (z) of the axially varying radius $r(z)$.

Specifically, mode coupling occurs when components of those spatial frequencies of $r(z)$ that are equal (or close) to $\Delta\beta$ exist, i.e. $|R(\Delta\beta)| > 0$ [56]. In other words, this is a perturbation with a grating structure whose period makes up the difference in propagation constants. Moreover, the coupling strength varies proportionally with $|R(\Delta\beta)|$. The actual power distribution of modes after the fluctuation depends on where the perturbation terminates, i.e. it depends on the coupling length, which is random. It is due to this reason that the SOP of light as it propagates through non-PM fibres evolves randomly and cannot be precisely determined.

Polarization is not the only randomly varying factor. The strength of birefringence (described by $\Delta\beta$) may also vary stochastically along the length of the fibre. The same goes for inverse group velocity (β_1) and GVD (β_2). This makes modelling propagation in fibres a complex task and requires treating a number of parameters (such the ones just mentioned) as random variables. The random nature of these parameters is already known to place considerable

limitations over the performance of single mode devices [17]. For example, the operating bandwidth for FWM-based fiber amplifiers/wavelength converters is impaired by dispersion fluctuations: while broadband gain is possible using dual pump configurations utilizing large pump-pump detuning around the zero dispersion wavelength (ZDW), the gain spectrum is not flat and gain uniformity is only achieved at the expense of gain bandwidth (i.e. lower pump-pump detuning). Similar impairments can be expected in the context of IM FWM, and will be discussed in Chapter 5.

Keeping the above description of fibre randomness in mind, we now return to the polarization insensitive nature of IM FWM observed in Section 4.2. In this regard, intra-group linear coupling plays an important role. Intra-group linear coupling, and hence randomness-induced polarization effects, can be taken into consideration by computationally modelling the fibre as a concatenation of short birefringent segments, with the orientation of the birefringence axes varying randomly from one segment to another [87], [88]. The orientation of the fast axis with reference to a fixed frame may be defined by the angle $\alpha(z)$, that varies stochastically from $-\pi$ to π with fibre length z.

While $\alpha(z)$ does not have a fixed pattern of variation, it is possible to define a length scale that characterizes it. This is called the fibre correlation length L_C, and for a given $\alpha(z)$, may be calculated by means of its autocorrelation function [87]. Physically speaking, L_C can be thought of as the typical spatial period of a longitudinal fluctuation: smaller values of L_C indicate faster (random) changes along fibre length as a result of random perturbations. Actual values of L_C can therefore vary depending on the environmental circumstances and conditions during fibre fabrication, and can be on the order of 1 m or greater [89].

Another important length scale is one that relates to the residual birefringence strength of the fibre: this is the fibre beat length. In fact, in a multimode fibre there will be a set of beat lengths, each one corresponding to a pair of (quasi) degenerate modes within a mode group. For the pair of modes $\{A_i, A_j\}$, the beat length would be given by $L_{B(A_i, A_j)} = 2\pi/(\beta_{A_i} - \beta_{A_j}) = 2\pi/\Delta\beta_{A_i, A_j}$. For the fundamental mode, standard communications fibres exhibit a beat length on the order of 10 m.

Light propagation dynamics in non-PM type fibres that exhibit random fluctuations, like the one used in our experiment, is strongly dependent on the ratio between L_C and the set of beat-lengths $\{L_B\}$ related to the pairs of quasi-

degenerate modes [87]. In the fibre being investigated, we have three distinct and independent spatial modes, namely LP_{01}, LP_{11a} and LP_{11b}, each with two-fold degeneracy due to the two orthogonal polarizations. Whenever $L_C \gg \max\{L_B\}$, the random spatial fluctuations in the fibre are slow enough not to induce any appreciable coupling between the polarizations within each mode. In this regime light propagates as in a fibre with fixed axes of birefringence (this would be referred to as a birefringent fibre). The same is true whenever the fibre length L is much shorter than L_C. On the contrary, when L_C is of the same order as or shorter than $\min\{L_B\}$, and in addition $L_C \ll L$, then the randomness plays an important role [87] (we refer to this as a 'randomly birefringent fibre').

In both types of fibres, birefringent and randomly birefringent, light propagation is described by a set of coupled nonlinear Schrödinger equations (NLSEs) [69], [84] not very dissimilar in form to those presented in Chapter 3. However, in order to take polarization into account, a vectorial approach is taken in deriving them, and the influence of randomly varying birefringence is included by adopting a reference frame that follows the fluctuations in $\alpha(z)$ along fibre length. Here, I summarize a theoretical treatment of our experiment taking this approach, which was originally developed by Dr Guasoni and presented in [53].

In view of the configuration illustrated in Fig. 4.1, we state the following definitions:

- v_x (u_x) is the (slowly varying) envelope of the x-polarized component for mode LP_{01} (LP_{11a}).
- β_{1ux} (β_{1vx}) is the IGV of the x-polarization of mode LP_{01} (LP_{11a}).
- β_{2ux} (β_{2vx}) is the GVD of the x-polarization of mode LP_{01} (LP_{11a}).
- γ is the Kerr-nonlinear coefficient related to mode LP_{01}
- γ_{uv} is the coefficient related to the inter-modal nonlinear interaction between v and u [90], and its magnitude depends on the transverse spatial overlap between the corresponding modes.

Now, x can be replaced with y in the above definitions to give the corresponding variables and parameters for the y polarization.

The set of NLSEs describing evolution of the LP_{01} and LP_{11a} modes (LP_{11b} can be treated in an identical manner) then take the following simplified form [53]:

$$i\frac{\partial v_x}{\partial z} + i\beta_{1vx}\frac{\partial v_x}{\partial t} + \beta_{2vx}\frac{\partial^2 v_x}{\partial t^2} - \gamma\left(a\left|v_x\right|^2 + b\left|v_y\right|^2\right)v_x = 0 \tag{4.3a}$$

$$i\frac{\partial u_x}{\partial z} + i\beta_{1ux}\frac{\partial u_x}{\partial t} + \beta_{2ux}\frac{\partial^2 u_x}{\partial t^2} - \gamma_{uv}\left(c\left|v_x\right|^2 + d\left|v_y\right|^2\right)u_x = 0 \tag{4.3b}$$

Two similar equations can be written for the y-polarization modes by making the exchange $x \leftrightarrow y$. In deriving these equations, it was assumed that the input signal and the generated idler waves propagating in the LP_{11} mode group are much weaker than the pump waves in LP_{01}, i.e. $|v_j| \gg |u_j|$, $j \in x, y$. Therefore, only the dominant nonlinear phase terms were retained (just as in Chapter 3) and terms containing $|u_j|^2$ were ignored.

The constants a, b, c and d take different values depending on the type of fibre. In a birefringent fibre $a = c = 1$ and $b = d = 2/3$ [87]. The y component of the pump field induces a nonlinear phase shift (XPM) on its x component (and vice versa), and is lower than the self-induced phase shift (SPM) by 2/3 for equal intensities ($|v_x| = |v_y|$). The influence of the pump fields on the signal and idler is evident from the presence of terms involving v in the second equation above, and also depends on the intermodal nonlinear parameter γ_{uv}. In general, this results in a complex evolution of the field SOPs. Moreover, because the XPM and SPM components are different, the relative orientation between the pump and signal polarization is still significant.

In the case of a randomly birefringent fibre, $a = b = 8/9$ and $c = d = 4/3$ [69]. This is valid in the regime $L \gg L_C$, where L is fibre length. There are two things to note here. Firstly, the strength of the XPM and SPM components are equalized. Because of the rapid (random) reorientation of the birefringence axes, the SOPs of all waves sample uniformly over all possible SOPs [91], and these equalized components are a result of averaging over these rapid fluctuations which have characteristic length L_C. Secondly, the averaging results in a reduction of the intra-modal nonlinear parameter by 8/9.

The above equations (also referred to as Manakov equations in the random-fibre case) can be solved analytically [92]. Choosing the reference frequency to be located at the average of the pump frequencies, the electric field $v_j(z,t)$,

consisting of the pump waves can be written as

$$v_j(z,t) = p_{j1}(z)\exp(-i\omega_p t) + p_{j2}(z)\exp(i\omega_p t) \tag{4.4}$$

where p_{j1} and p_{j2} are the field amplitudes of the pumps centred at $-\omega_p$ and $+\omega_p$, respectively.

The field $u_j(z,t)$ can be written as a linear combination of the signal $s_j(z)$ at ω_s, and the phase-matched idler, $i_j(z)$ at the red-shifted frequency ω_{BSr}:

$$\omega_{\mathrm{BSr}} = \omega_s - 2\omega_p \tag{4.5}$$

$$u_j(z,t) = s_j(z)\exp(i\omega_s t) + i_j(z)\exp(i\omega_{\mathrm{BSr}} t) \tag{4.6}$$

Assuming that the input pump components have the same power ($|p_{j1}(0)|^2 = |p_{j2}(0)|^2 = P$) and are linearly co-polarized along the x-axis, inserting the fields above into the vectorial equations yields the magnitudes of $i_x(z)$ and $i_y(z)$ to give [53]:

$$|i_x(z)| = c|s_{x0}|\gamma_{uv}Pz\,\mathrm{sinc}(k_x z) \tag{4.7a}$$

$$|i_y(z)| = d|s_{y0}|\gamma_{uv}Pz\,\mathrm{sinc}(k_y z) \tag{4.7b}$$

where

$$k_x^2 = \Delta\beta_x^2 + (c\gamma_{uv}P)^2 \tag{4.8a}$$

$$k_y^2 = \Delta\beta_y^2 + (d\gamma_{uv}P)^2 \tag{4.8b}$$

$$\Delta\beta_j = -\beta_{vx}(-\omega_p) + \beta_{vx}(\omega_p) + \beta_{uj}(\omega_{\mathrm{BSr}}) - \beta_{uj}(\omega_s) \tag{4.9}$$

$\Delta\beta_j$ is the phase mismatch term related to the BSr process, whereas $\beta_{uj}(\omega)$ and $\beta_{vj}(\omega)$ are the wave-vectors of the LP_{01} and LP_{11a} mode group computed at the frequency ω. Note that for the pump we only employ wave-vectors $\beta_{vx}(\pm\omega_p)$, as both pumps are assumed to be x-polarized.

We now define the ratio $R = P_{I\parallel}/P_{I\perp}$ where $P_{I\parallel}$ ($P_{I\perp}$) is the idler power when the input signal and the pumps are co-polarized (cross-polarized), as a function of length for two different types of fibers: random and birefringent. $P_{I\parallel}$ and $P_{I\perp}$ were obtained using the same parameters and values used in the actual experiment reported above. Fig. 4.9 plots the ratio R for two different

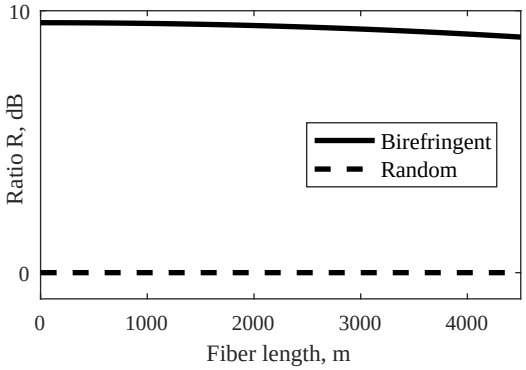

Figure 4.9. Ratio R as a function of the fibre length in a birefringent or randomly birefringent fibre. Per pump input power was set to 20.5 dBm [53].

cases: a birefringent fibre and a randomly birefringent fibre.

A variation of up to 9.5 dB between the co-and cross-polarized instances for the birefringent fibre can be seen, confirming the strong dependence of the idler growth on the signal polarization. On the contrary, in the case of a randomly birefringent fibre, the idler growth is independent of the signal polarization, with $R \approx 1$, irrespective of the fibre length.

Going back to the experimental results, in both the fibre lengths tested (50 m and 1 km), the measured values for CE are compatible with the theoretical estimate for randomly birefringent fibres ($R = 0\,\text{dB}$) rather than for birefringent fibers ($R = 9.5\,\text{dB}$). We therefore conjecture that the length scale L_C of random fluctuations is much shorter than 50 m in the fibre under investigation. It would have been interesting to test polarization dependence for even shorter fibre lengths where one might have reached $L \leq L_C$. However, such short fibre lengths would give FWM idlers much below the experimental noise floor, and any idler generation would therefore be unmeasurable.

4.4 Conclusions

The dependence of output idler generation on the relative SOPs between the input waves is an important consideration in the design of a wavelength converter or parametric amplifier. The configuration of IM FWM that has been experimentally characterized in this chapter provides some fundamental rules relating to this topic.

Firstly, we experimentally demonstrated polarization insensitive wavelength

conversion based on IM FWM in both a 1 km and a 50 m long three-mode fibre. By launching two co-polarized pumps in the LP_{01} mode and the signal in either the LP_{11a} or LP_{11b} modes at the phase-matched wavelengths, conversion of signals in the C- or the L-band (respectively) was achieved with a signal polarization sensitivity of less than 2 dB. Additionally, idler generation was strongly suppressed when the pumps were orthogonally polarized.

The theory describing randomly birefringent fibres, i.e. fibres where the length scale of longitudinal fluctuations is shorter than the birefringence beat lengths of the relevant modes, predicts polarization independent idler generation in the configuration we have tested. This prediction is borne out in our experiments.

Conversion bandwidths of up to 3 nm at −6 dB were demonstrated, which is meagre compared to what can be achieved with the best single mode devices. How much of an improvement can be made over these results with simple modifications to fibre design will be the subject of the next chapter.

Chapter 5

Bandwidth enhancement of inter-modal four-wave mixing by dispersion engineering

The previous chapter investigated IM FWM in an elliptical-core few-mode fibre. A configuration was used in which both pumps resided in the fundamental mode and the signal (and idler) were in the LP_{11} mode group. Among the measurements presented for that fibre were those relating to CE bandwidth.

Achieving a broad CE bandwidth is relevant in the context of optical amplifiers and wavelength converters in general because it allows a larger number of optical channels to be processed simultaneously; this is a situation typically encountered in WDM systems which are in widespread use today. It is therefore important to find ways of increasing the bandwidth of CE in IM FWM, regardless of the input configuration employed. Another related aspect that has received much attention in the context of single mode devices is the sensitivity of CE to signal wavelength. This relates to the flatness of the CE curve, and will determine the extent of discrepancy in OSNR between the converted (amplified) channels.

This chapter delves into the above in more detail by characterizing a new set of fibres tailored for the purpose of obtaining an improvement in CE bandwidth. It was found that these fibres, fabricated by our collaborators at Sumitomo Japan, were able to provide an enhancement of this important parameter.

5.1 Inverse group velocity and conversion efficiency bandwidth

We begin with a review of the definitions of some key variables which will be used in the rest of this chapter. In this regard, Fig. 5.1 shows the configuration being used. This is the now familiar 'asymmetric' configuration used previously: the pair of pumps excite one propagation mode (LP_{01}) while the signal excites a different one (LP_{11}).

Inputs $p1$ and $p2$ at frequencies ω_{p1} and ω_{p2} respectively are the high intensity applied fields (pumps). The input signal s at ω_s is separated from the pumps by $\Delta\omega_{ps} = \omega_{p2} - \omega_s$ (note that below we will occasionally refer to $\Delta\lambda$ as the wavelength separation corresponding to $\Delta\omega$). The energy conservation relation to generate the red-shifted idler i_{BSr} at ω_{BSr} is given by $\omega_{\mathrm{BSr}} + \omega_{p2} \rightarrow \omega_s + \omega_{p1}$, implying the creation of $p2$ and i_{BSr} photons and the annihilation of s and $p1$ photons. A similar relation holds for the blue-shifted idler i_{BSb} located at ω_{BSb}.

As established in earlier chapters, the generated idler at ω_{BSr} in the LP_{11} mode is phase-matched if the inverse group velocity (IGV) curves evaluated at the average frequency of the waves in the same mode are nearly equal for the two modes (see also Fig. 5.2) [46], [81]. In other words, for a small frequency detuning ($\Delta\omega_{pp} \approx 0$), phase matching is achieved if a horizontal line can be drawn in Fig. 5.2 to intersect the IGV curves of the two modes at the values corresponding to the mean frequencies of the waves in each mode. Furthermore, broadband phase matching for the BSr idler – i.e. phase-matching for large detuning $\Delta\omega_{pp}$ – is achieved when the IGV curves of the two modes are

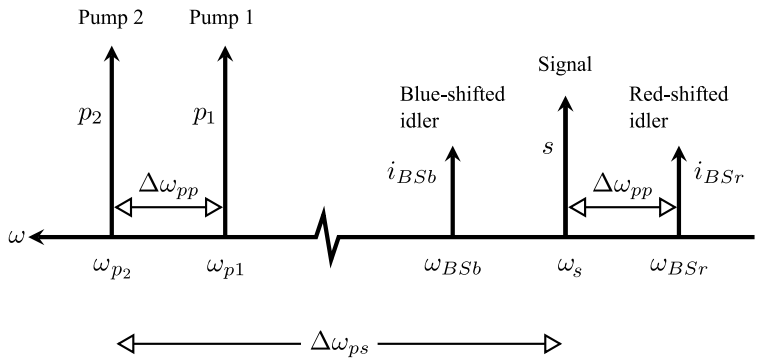

Figure 5.1. Frequency allocation in a FWM BS process.

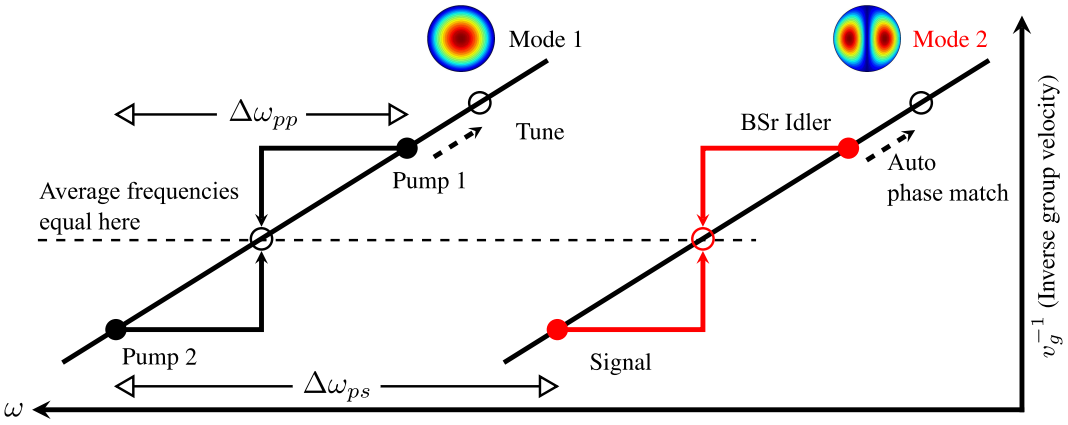

Figure 5.2. Illustration of the relationship between the inverse group velocity (IGV) curves of the participating modes. The IGV curves need to be parallel in order to satisfy phase matching for the BSr idler when Pump 1 is tuned.

horizontally shifted replicas of one another [48].

5.2 Fibre profile, fabrication and characterization

The index profile of a step index waveguide is particularly simple. Inside the core, the refractive index n_{core} is constant across the transverse dimensions. At the perimeter of the core, there is an abrupt (albeit small) index differential due to the lower index (n_{clad}) cladding region. It is well known that in MMFs, such an index profile results in large intermodal dispersion, i.e. the difference in group-velocity between different mode groups is high [56]. This is a significant factor in the type of IM FWM being considered here because the phase-matching condition is strongly dependent on the relative IGV between the modes: step-index waveguide modes will be phase-matched at large pump-to-signal wavelength separations ($\Delta\omega_{ps}$). This becomes an issue when the bandwidth of light-sources available is limited (our sources and amplifiers covered the C- and L- bands).

In this regard, GI fibres offer a useful platform for IM FWM involving LP_{01} and LP_{11} modes at wavelengths not too far apart, such as between the C- and L-bands. In contrast to a step-index fibre, a GI fibre features a gradually decreasing core index which becomes equal to the (constant) cladding index

n_{clad} at the perimeter of the core. If the maximum value of the core index is denoted by n_{core}, a GI profile $n(r)$ can be described by a power-law formula of the form

$$n(r) = \begin{cases} n_{\text{core}}\sqrt{1 - 2\Delta(r/R)^{\alpha}} & r \leq R \\ n_{\text{clad}} & r > R \end{cases}$$

where R is the core radius, r is radial distance from the centre, $\Delta = (n_{\text{core}}^2 - n_{\text{clad}}^2)/2n_{\text{core}}^2$, and α is a parameter that characterizes the abruptness of the transition between the core and cladding indices.

Fig. 5.3(a) shows power law profiles for three different values of α. While $\alpha = 1$ (a triangular profile) and $\alpha = \infty$ (which coincides with a step-index design) are extreme examples, the case of the parabolic profile $\alpha = 2$ is of particular utility in MMFs. This is because it corresponds to the profile that, to good approximation, minimizes intermodal group delay, therefore leading to very closely spaced RIGV curves [56].

Therefore, it can be shown (by simulation) that a fibre core based on a small deviation to the parabolic profile will result in nearly parallel IGV curves while providing the requisite separation between them in wavelength, i.e. sufficiently large $\Delta\lambda_{ps}$ for phase-matching between the C- and L-bands.

Fig. 5.3(b) shows the index profile of a preform that was fabricated by Sumitomo for the production of our fibres, and whose design was guided by the principles outlined above. The targeted profile is shown in red. With the exception of some fine ripples near the centre, the experimentally measured profile (solid black line) matched the targeted contour. The dispersion characteristics of fibres of varying diameter with the same profile as Fig. 5.3(b) were simulated.[1] This gave a sense of what diameters would be best suited for our experimental needs, i.e. achieving larger $\Delta\omega_{pp}$ bandwidths (for the BSr process) while keeping $\Delta\omega_{ps}$ small enough for IM FWM within the C- and L-bands. Thereafter, the preform was drawn to several fibres of length 100 m and with four core diameters ranging from 18.1 µm to 25.3 µm.

The FUTs were based on the same GI fibre core made of highly GeO_2-doped SiO_2 having a quasi-parabolic index profile (see Fig. 5.3(b)). The core had a peak index difference of 2.0% relative to the cladding and a fitted alpha-power

[1]Simulation work reported in this chapter was carried out by Prof. Horak and is published in [54].

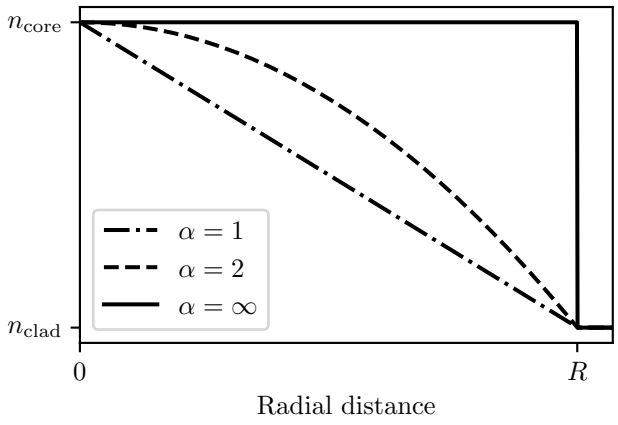

(a)

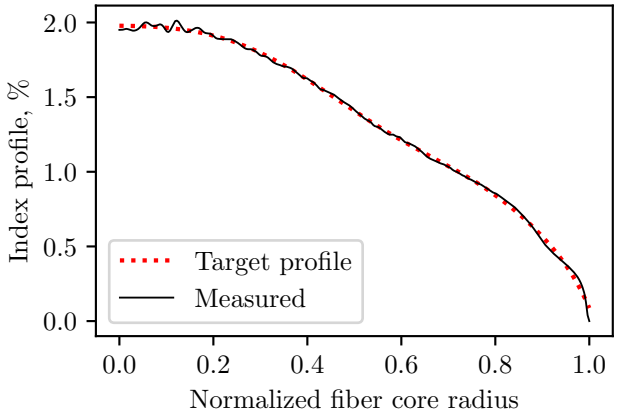

(b)

Figure 5.3. (a) Power-law index profiles for different values of parameter α. (b) Refractive index of the fabricated GI MMF preform (solid line) and the profile used for numerical optimization of the fibre design (dashed line).

of 2.1 in the range of radii up to 50% of the core radius where the majority of LP_{01} and LP_{11} modal power was concentrated. The core was surrounded by a pure SiO_2 cladding.

After the fibres were fabricated, we experimentally measured the IGV curves of the supported modes of all GI MMFs using the TOF method specified in Chapter 3. Fig. 5.4 shows experimentally measured relative IGVs for all measurable modes for each of the FUTs. IGV curves of the modes of interest, namely LP_{01} and LP_{11}, are shown in black.

Based on our TOF analysis, the total number of spatial modes supported

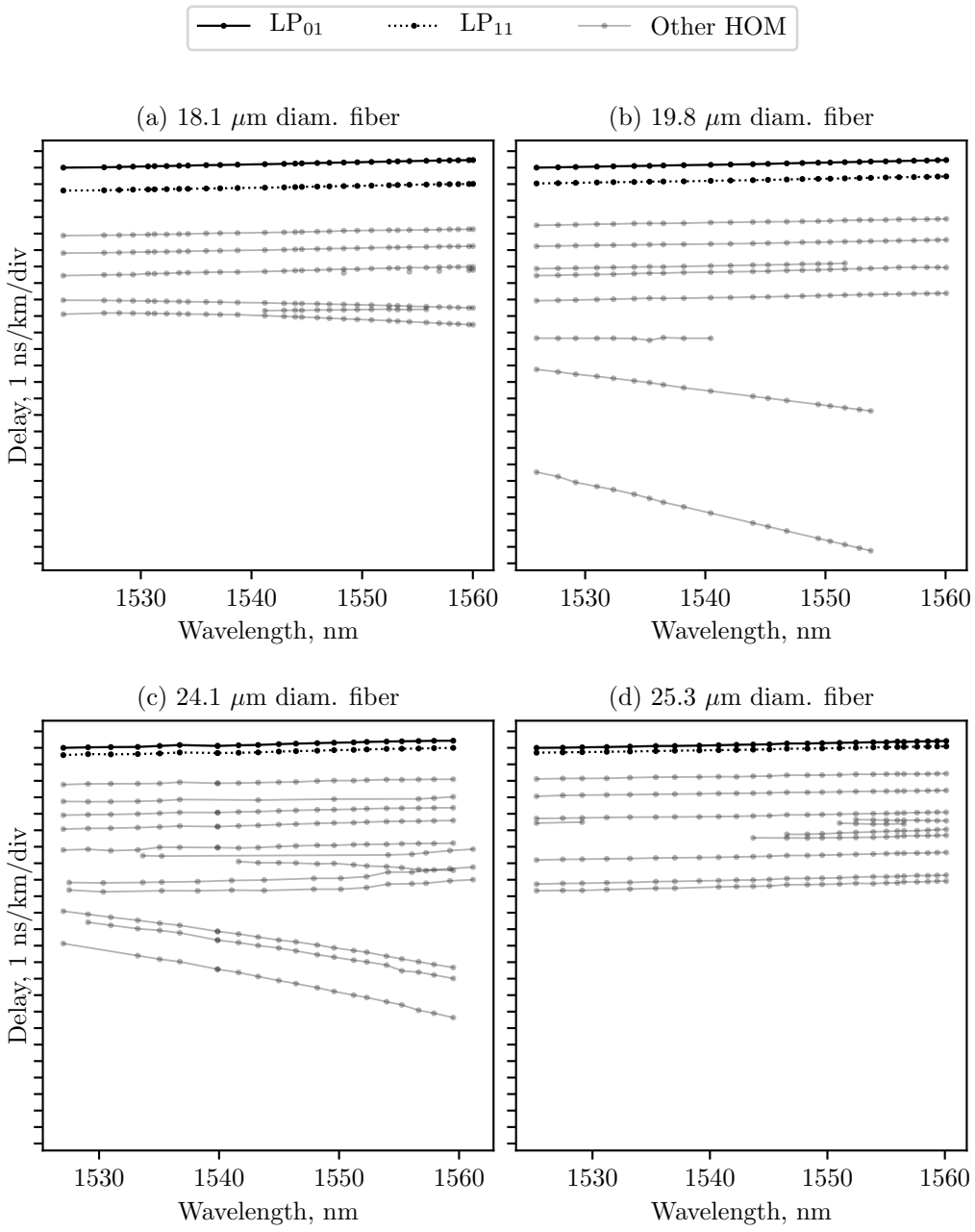

Figure 5.4. Measured RIGV curves for four fibres of varying diameter fabricated by Sumitomo. All modes resolvable using the time-of-flight method are shown.

by the fibres was typically greater than ten. The horizontal separation between any pair of IGV curves can be estimated by treating them as approximately linear. This value corresponds to the wavelength spacing $\Delta\lambda_{ps}$ necessary to achieve phase matching between the two modes. Therefore, in principle, dif-

ferent mode pairs among the ones shown in Fig. 5.4 could be used to achieve phase-matching in frequency bands further apart than those corresponding to the LP_{01}-LP_{11} mode pair.

It should be noted that mode characterization using the TOF method is limited by several factors including photodetector bandwidth, the length of the fibres, and the initial temporal pulse width of the optical source that was available for our experiments. Our characterization was done using a mode-locked fibre laser producing 0.5 ps pulses with a repetition rate of 20 MHz and 4 mW of average power. Each pulse experienced intermodal dispersion inside the FUTs, and the delays of the resulting modal components were measured on a 10 GHz oscilloscope. Based on these parameters, we could not precisely quantify IGV behaviour at points where the modal delays became too small (of the order of 50 ps over 100 m) which resulted in the partially completed IGV curves in Fig. 5.4.

The separation $\Delta\lambda_{ps}$ between the IGV curves of the LP_{01} and LP_{11} modes for all four fibres, as extracted from the plots in Fig. 5.4, is shown in Fig. 5.5. Note that in obtaining the measured (starred) values in Fig. 5.5, a linear regression for the IGV curves was used in order to extrapolate beyond the measured wavelength range. Simulations based on the refractive index profile of Fig. 5.3(b) predict the same trend as the measurements: an increase in core diameter of the GI MMF corresponds to a reduction of $\Delta\lambda_{ps}$.

For the 18.1 µm and 19.8 µm diameter fibres, $\Delta\lambda_{ps}$ was too large to enable IM FWM using the C- and L-band laser sources available at the time. It was therefore decided to limit our investigations to the 24.1 µm and 25.3 µm

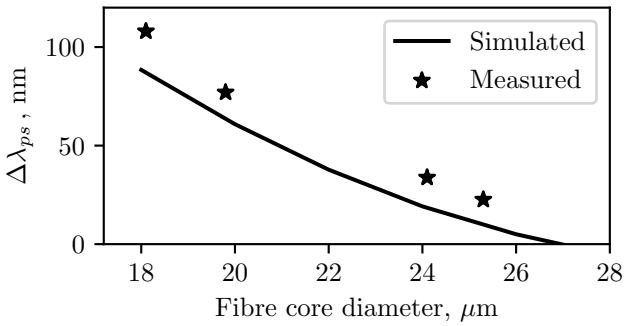

Figure 5.5. Simulated (line) and measured (stars) pump-to-signal wavelength detuning, $\Delta\lambda_{ps}$, as a function of the core diameter of the GI MMF.

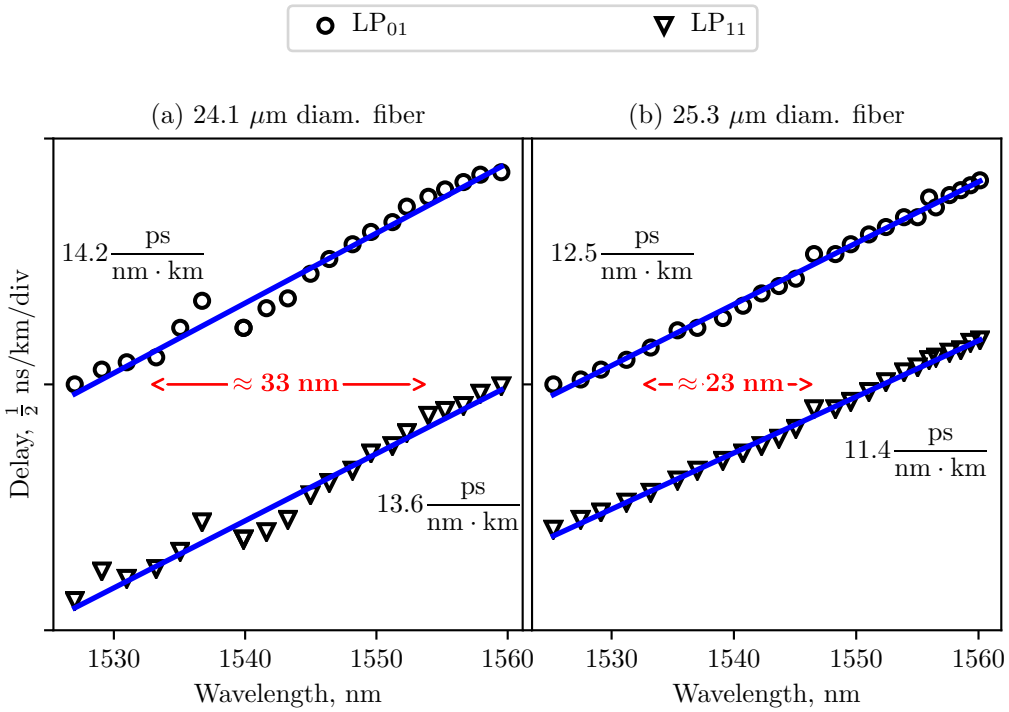

Figure 5.6. A closer look at the delay curves for the modes of interest for the two selected fibres.

diameter fibres, which could support a phase-matched interaction between the LP_{01} and LP_{11} modes, with wavelength spacings ($\Delta\lambda_{ps}$) of approximately 33 nm and 23 nm respectively.

Detailed IGV curves of the modes of interest (namely LP_{01} and LP_{11}) are shown for the 24.1 µm and 25.3 µm core diameter fibres in Fig. 5.6(a) and (b), respectively. The slope of an IGV curve evaluated at a particular wavelength gives the dispersion parameter (at that wavelength). Using the linearised IGV curves, we estimated chromatic dispersion values of 14.2 ps/(nm km) (12.5 ps/(nm km)) for the LP_{01} mode and 13.6 ps/(nm km) (11.4 ps/(nm km)) for the LP_{11} modes of the 24.1 µm (25.3 µm) diameter core fibres. Clearly, a large difference in the β_1 slopes between modes will lead to small $\Delta\lambda_{pp}$ bandwidths (also see Fig. 5.2). The effective areas for the 25.3 µm fibre were calculated to be 55.7 µm^2 (LP_{01}) and 75.6 µm^2 (LP_{11}). For the 24.1 µm fibre, the areas were 52.8 µm^2 (LP_{01}) and 72.4 µm^2 (LP_{11}).

5.3 Experimental set-up

Next, for our chosen fibres, we experimentally measured the CE bandwidths for the IM FWM configuration illustrated in Figs. 5.1 and 5.2.

The experimental set-up for IM FWM is shown in Fig. 5.7. Three CW laser sources were used to produce the applied optical beams (two pumps and a signal) at the fibre input. For each fibre, the total pump power was about 23.5 dBm, while the signal power was about 8.5 dBm. No SBS was experienced in these fibres at this level of input power. Therefore, in contrast to the previous chapter, no pulse carvers were used.

As per the configuration in Fig. 5.1, the pumps (signal) were launched into the fundamental (LP_{11}) mode. The inputs were coupled using a beam-splitter cube and their polarizations were aligned at the fibre input by a combination of polarization controllers and a (free-space) PBS. A two-mode fibre (TMF),[2] which made it easier to selectively launch the LP_{01} or LP_{11} mode for coupling into the FMF, was spliced to the input of our GI MMF to increase the modal purity inside the fibre. This was done because in order to efficiently excite the LP_{11} mode in the MMF, the launch beam had to closely resemble the LP_{11} mode profile in terms of phase and intensity. For the relatively simple launch method we were using, it was easier to excite mode LP_{11} selectively in a two-mode fibre (or three-mode fibre for that matter, as done in previous chapters) than in a fibre that supported many more modes. Thus we used the two-mode fibre to guide a LP_{11}-like beam profile to the input facet of the GI MMF; this

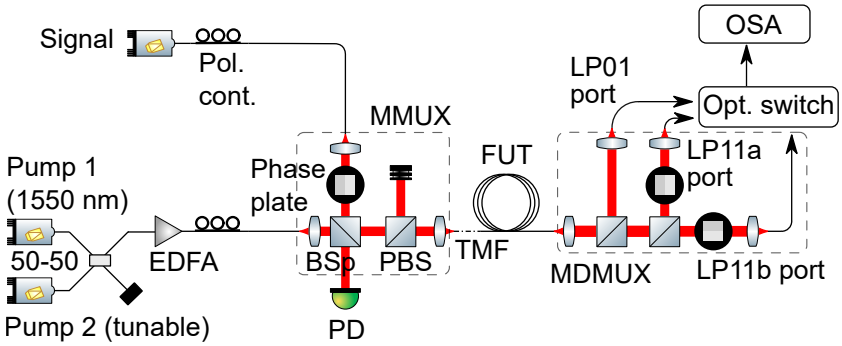

Figure 5.7. Experimental setup for inter-modal FWM using a set of graded-index multimode fibres.

[2]More precisely, a two-mode-group fibre.

was justified due to the significant overlap of the LP_{11} modes in the two fibres, and worked well in practice.

At the GI MMF output, a MDMUX identical to the one discussed in earlier chapters was used. It should be noted that even though the input beam shape is LP_{11a}-like, mode-mixing occurs during propagation in the GI MMF between the LP_{11a} and LP_{11b} modes and thus two orthogonally oriented PPs in the MDMUX are used to measure total output power. Both the MMUX and MDMUX gave mode extinction ratios of up to 20 dB.

5.4 Results

First, we experimentally verified that the estimated values of $\Delta\lambda_{ps}$ in Fig. 5.5 lead to efficient BSr idler generation. This was done by keeping the wavelengths of $p1$ and $p2$ constant at 1552.5 nm and 1550 nm, respectively, while scanning the signal wavelength around its predicted value. The measured BSr CE as a function of signal wavelength (or equivalently $\Delta\lambda_{ps}$) is plotted in Fig. 5.8 for both fibres. Idler generation was observed for a small range of signal wavelengths centred on 23 nm (35 nm) separation from pump $p1$ for the 25.3 µm (24.1 µm) core-diameter fibre. This shows good agreement with the results

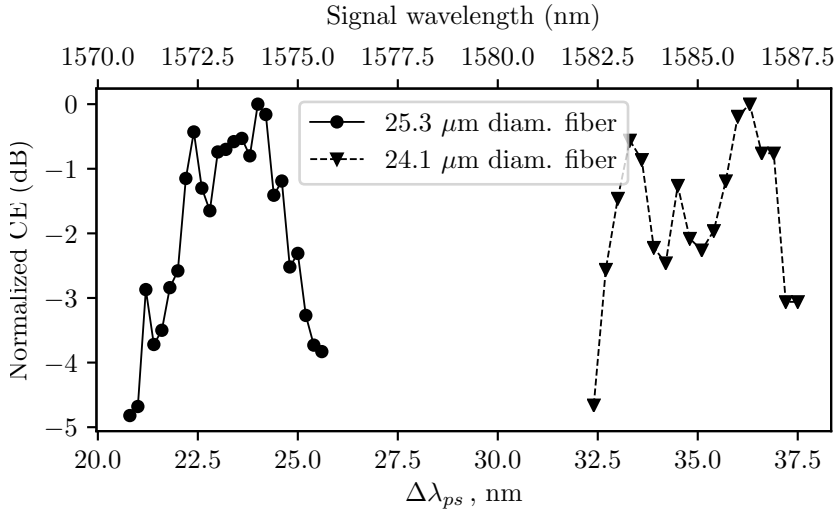

Figure 5.8. The variation of CE with signal detuning $\Delta\lambda_{ps}$ (from fixed pumps) for the two fibers. Pump wavelengths are $\lambda_{p1} = 1550$ nm and $\lambda_{p2} = 1552.5$ nm.

of the TOF characterization presented earlier in Fig. 5.6, which predicted phase matching at separations of 23 nm (33 nm) for the 25.3 µm (24.1 µm) core-diameter fibre.

We then characterized the CE behaviour of the BSb and BSr idlers as $\Delta\lambda_{pp}$ was varied. The signal wavelength was adjusted to achieve the broadest bandwidth. Fig. 5.9(a) shows typical IM FWM spectra obtained at the recombined LP_{01} MDMUX output port for two values of $\Delta\lambda_{pp}$ (0.5 nm and 3 nm) when using the 25.3 µm core diameter fiber (hence $\Delta\lambda_{ps} \approx 23$ nm). As expected, when $\Delta\lambda_{pp}$ increases from 0.5 nm to 3 nm the power of the phase matched BSr idler remains fairly constant, while the non-phase matched BSb idler vanishes for $\Delta\lambda_{pp} > 3$ nm. This provides more than 20 dB extinction between the desired (BSr) and the unwanted (BSb) idler. The optical signal to noise ratios of both BSr idlers are more than 20 dB, and the corresponding measured CEs are about −35 dB. The relatively low CE values are in part due to the large core diameters of the 100 m long fibres as well as the relatively low pump powers used, and could be improved by implementing more complex fibre designs with smaller cores or by utilizing materials with higher nonlinearity.

The normalized CE as a function of $\Delta\lambda_{pp}$ for the two fibres is shown in Fig. 5.9(b) and (c). For the 25.3 µm diameter fibre, a −3 dB half-bandwidth of about 6.5 nm (0.5 nm) was obtained for the BSr (BSb) idler. This result represents a bandwidth enhancement (for BSr) of 100% as compared to our previously reported work (see Chapter 4) in a fibre half the length of the fibre under investigation. This also highlights that it is possible to selectively phase match only the desired nonlinear process (BSr versus BSb) by properly engineering the spatial modes of the fibre. Note that this feature cannot be attained only by dispersion engineering a low-birefringence single mode fibre. This unidirectionality of FWM BS was also recently demonstrated by exploiting the polarization modes of a silicon waveguide [93]. For the 24.1 µm diameter fibre, the measured 3 dB half-bandwidth was reduced to 3.5 nm (0.5 nm) for the BSr (BSb) idler.

Simulations of IM FWM relating to the above fibre were also done by incorporating experimentally determined IGV data in the multi-mode generalized nonlinear Schrödinger equation developed originally in [90] by Prof. Horak. These predicted greater bandwidths than those measured above. For example, a maximum CE bandwidth of approximately 18 nm (24 nm) was expected for the 25.3 µm (24.1 µm) fibre. We attribute the discrepancy between the simu-

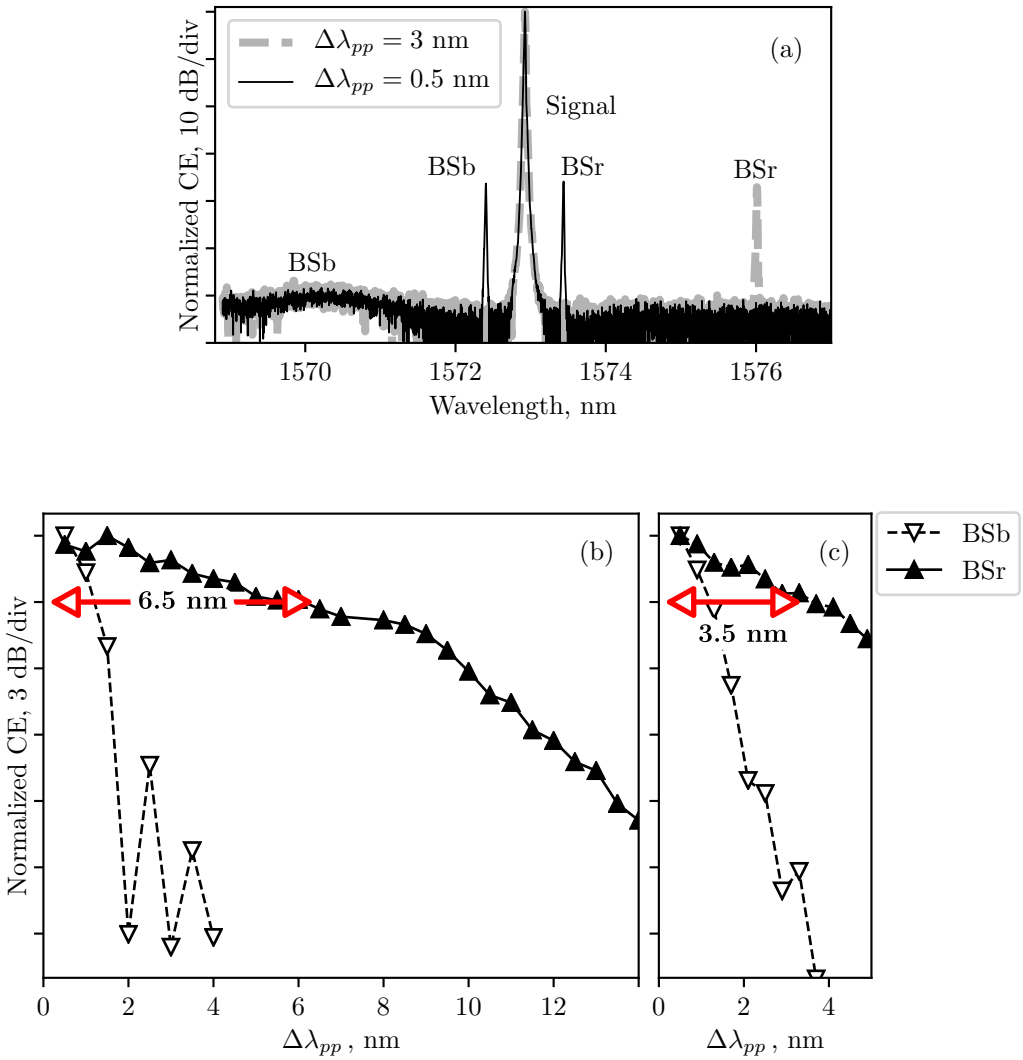

Figure 5.9. (a) Measured spectral traces for $\Delta\lambda_{pp}$ equal to 0.5 nm and 3 nm for the 25.3 µm fiber. (b) and (c) Normalized CEs of the BSb and BSr processes with respect to $\Delta\lambda_{pp}$ for the 25.3 µm and 24.1 µm core diameter GI MMFs respectively.

lated and experimental bandwidths to be firstly due to higher order dispersion terms, which were not included in the simulations, because they could not be derived with confidence from the IGV measurements over a limited wavelength range. These play a more critical role in the FWM process as $\Delta\omega_{ps}$ increases, i.e. in the 24.1 µm diameter fibre. To better appreciate the implications of higher order dispersion in simulations, the wavelength range of the measured IGV curves would have to be enlarged, which was not possible at the time.

Additionally, as discussed in the previous chapter, FWM is affected by

stochastic variations of key fibre parameters (e.g. core ellipticity, dispersion characteristics) which cannot be avoided. A detailed computational investigation into IM FWM in randomly birefringent fibres is reported in [87]. In short, it turns out that IM FWM (CE) bandwidths of the kind presented above can be strongly impaired by variations in *intergroup* parameters. That is, if the group-velocities ($\propto \beta_1^{-1}$) and chromatic dispersion (β_2) of mode-groups are z-dependent, a significant reduction in bandwidth occurs. This can happen even when the intergroup fluctuations result from variations in core-radius characterized by a standard deviation of as little as 0.5%,[3] with stronger impairment expected in fibres with smaller cores [87]. This is unsurprising, given that the phase matching condition for IM FWM involves the aforementioned parameters. On the contrary, variations in *intragroup* parameters relating to the quasi-degenerate modes – i.e. random fluctuations in beat lengths (see Section 4.3) and relative IGVs *within* mode-groups – have negligible bandwidth impairment and IM FWM is dependent only on their spatial average.

5.5 Broadband phase matching for the PC process

The IM FWM processes studied above have been of the Bragg scattering type, with the BSr process being phase matched for large $\Delta\omega_{pp}$ when the IGV profiles are parallel (as in Fig. 5.2).

One may ask if it is also possible to have an automatically phase matched IM FWM process of the Phase Conjugation type. It turns out that it may have the same attribute if one of the modes has an IGV curve whose gradient is equal in magnitude but opposite in sign. Such a scheme is depicted in Fig. 5.10.

The idler frequency in Fig. 5.10 may be written as $\omega_{\mathrm{PC}} = (\omega_{\mathrm{P1}} - \omega_s) + \omega_{\mathrm{P2}}$ (the frequencies of the pumps and signal are denoted in the usual manner) and the phase mismatch parameter can be expanded about a nearby frequency ω_0, just as was done in Chapter 3, to make the IGV dependence on phase matching clearer:

$$\Delta\beta = \beta^{(11a)}(\omega_{\mathrm{P2}}) + \beta^{(\mathrm{M1})}(\omega_{\mathrm{S}}) - \beta^{(\mathrm{M2})}(\omega_{\mathrm{PC}}) - \beta^{(\mathrm{M1})}(\omega_{\mathrm{P1}})$$

[3] That is, 0.5% of core-radius, with a correlation length L_C. A changing radius induces variations in intergroup parameters which can be computed by standard methods.

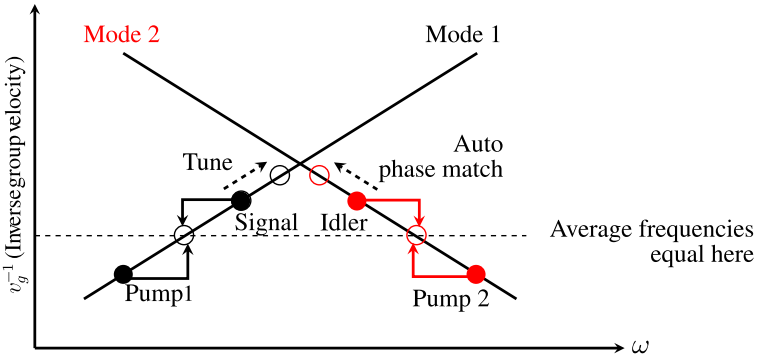

Figure 5.10. IGV curves needed for broadband phase matching for the IM FWM Phase Conjugation process. The curves are symmetrical about the frequency at which they intersect.

$$\approx \left[-\beta_2^{(\mathrm{M2})} \left(\frac{\omega_{\mathrm{PC}} + \omega_{\mathrm{P2}}}{2} - \omega_0 \right) - \beta_1^{(\mathrm{M2})}(\omega_0) \right.$$
$$\left. + \beta_2^{(\mathrm{M1})} \left(\frac{\omega_{\mathrm{P1}} + \omega_{\mathrm{S}}}{2} - \omega_0 \right) + \beta_1^{(\mathrm{M1})}(\omega_0) \right] \times (\omega_{\mathrm{P1}} - \omega_{\mathrm{S}}) \,, \qquad (5.1)$$

where $\beta_n^m(\omega_0)$ is the n-th derivative of the propagation constant of mode m evaluated at frequency ω_0.

The sum of the first two terms in square brackets is equal to the (negative of the) Mode 2 IGV evaluated at the average of the Pump 2 and idler frequencies. Similarly the last two terms equal the Mode 1 IGV evaluated at the average of the Pump 1 and signal frequencies. Clearly, phase matching may be achieved if these two sums are equal in magnitude, and this explains why dispersion characteristics of the kind shown in Fig. 5.10 may lead to broadband phase matching for the PC process.

The mirror symmetry between IGVs required for implementing the above concept is not out of reach. In fact, such dispersion characteristics can be realized practically by utilizing the LP_{02} mode of a dispersion engineered step-index fibre, and the design considerations involved are covered in detail in [47]. The TOF characterization of one such fibre fabricated for this purpose is shown in Fig. 5.11(a). Inter-modal phase matching between the LP_{02} and LP_{11} modes was expected in the L-band.

While it was possible to identify the other higher-order modes in the given fibre by examining their intensity profiles at the fibre output, such direct visual evidence of the LP_{02} mode was elusive. Because of difficulty in its selective

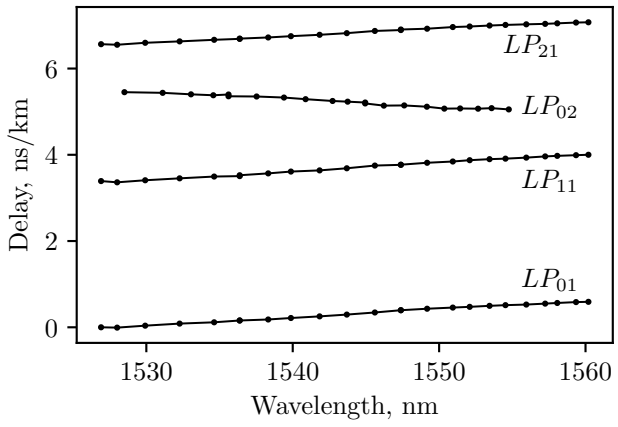

(a)

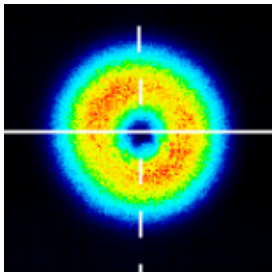

(b) LP_{11}.

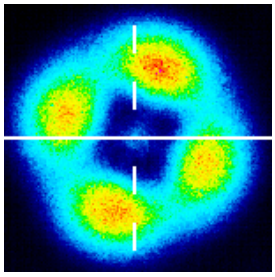

(c) LP_{21}.

Figure 5.11. (a) RIGV curves for the modes of an experimental fibre. (b) and (c) CCD profiles of some higher-order modes for a step-index fibre designed for broadband phase-matching for the phase-conjugation process.

excitation by means of the LP_{02} PP available, high modal purity could not be achieved. Mode images of the HOMs identified are shown in Fig. 5.11(b) and (c). The problem of mode excitation was compounded by the high bending loss experienced by mode LP_{02}, given that it was fairly close to its cut-off wavelength in the C-band. Due to these reasons, it was decided to halt work on this fibre.

5.6 Conclusion

In space division multiplexed networks designed to overcome the 'capacity crunch' of SMF based systems, the broadband operation of inline amplifiers and wavelength (or mode) converters is a practical requirement. In this chapter, we have reported on the design, fabrication and characterization of graded index multi-mode fibres with the aim of obtaining improved bandwidth for the

inter-modal Bragg Scattering FWM process. In our proof-of-principle experiments, we measured bandwidths of up to 6.5 nm in a 100 m fibre, which are about twice those obtained in the previous chapter for a fibre half this length.

Following this work, the principles described here have been successfully adapted for IM FWM in silicon-rich silicon nitride waveguides as reported in [94]. This material platform allows fine control of the refractive index by tuning its stoichiometry [95], which together with adjustment of structural geometry enables dispersion engineering of the waveguide modes. Moreover, by carefully balancing its composition, its properties can also be tuned for low linear and nonlinear losses in the telecom bands while having high nonlinearity [94], [96] (two orders of magnitude higher than silica). These properties, combined with the relatively short length of the waveguide used in [94] (4 cm) resulted in a CE bandwidth greater than 40 nm for the BSr process.

Therefore, we can conclude based on the above that while IM FWM in MMFs for broadband applications can certainly benefit from dispersion engineering, the results obtained are likely to fall short of predictions based on models that do not take into account the randomness of the fibre's dispersion parameters. Nevertheless, the principle of using IM FWM for achieving enhanced CE bandwidth is one that holds significant potential, as evidenced by impressive results in the area of silicon photonics [94].

Chapter 6

Selective wavelength conversion in a few-mode fibre

The last three chapters have focused mainly on the basic principles of IM FWM in FMFs. Topics such as the role of input SOPs, dispersion of modes and their relation to conversion efficiency bandwidth were considered. It should be kept in mind, however, that these principles are ultimately to be used as a means for the processing (frequency conversion, phase conjugation, amplification) of a data-carrying signal. Indeed, one of the most attractive features of nonlinear optical signal processing is transparency to the modulation format employed to encode data.

So far, our experiments have made use of a CW signal, i.e. no modulation. In view of the above, it is therefore imperative that we test the ability of IM FWM as a method for carrying out signal processing tasks. To this end, the first section of this chapter is devoted to a demonstration of stable and error-free wavelength conversion of an intensity modulated signal.

A further interesting and potentially useful aspect of IM FWM is the possibility to provide localized parametric gain, i.e. to selectively implement a signal processing functionality on just one of a number of signals closely spaced in frequency (a typical application area of this could be wavelength division multiplexed networks, in which channel spacings are of the order of 10 GHz to 100 GHz). This aspect will be considered in the latter sections of this chapter.

6.1 Demodulation of wavelength converted 10 GHz inter-modal Bragg scattering idler

We now demonstrate the recovery of data from an optical field that has been converted in wavelength using IM FWM. This will consist of a bit error rate test (BERT) of an idler field that is coupled nonlinearly to a data modulated signal.

In order to do wavelength conversion, we employed the same 25.3 µm diameter, 100 m long graded-index FMF used for inter-modal Bragg scattering in the previous chapter, albeit in a different input configuration. The requisite experimental set-up is shown in Fig. 6.1. It can be inferred from this setup that, in contrast to the input configuration in Chapter 5, the pumps are in the LP_{11} mode and the signal is in the fundamental mode. In other words, the modes of the signal and pumps have been exchanged. This choice was made to simplify the collection of the (LP_{01}) idler field at the output of the fibre.

The pumps were amplified and launched into the LP_{11} mode of the GI FMF using a free-space PP. The signal was modulated with an on/off keying (OOK) data stream at 10 Gb/s and amplified. Broadband ASE from the EDFA was rejected using a 1.8 nm filter to prevent the OSNR of the idler from being

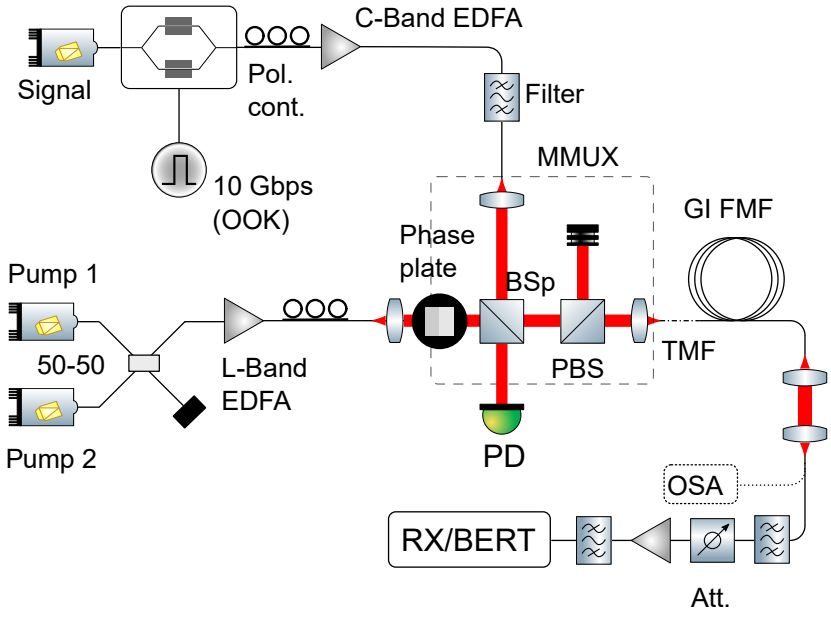

Figure 6.1. Experimental setup for bit error rate test (BERT) of IMFWM.

compromised by noise. The signal and pumps were coupled to the two modes of the FMF using a free-space BS and their polarizations were aligned at the fibre input by a combination of polarization controllers and a (free-space) PBS. As before, a short length of TMF (~1 m) was spliced to the input of our GI FMF to improve modal excitation. At the FMF input the total pump power was estimated as 23.5 dBm. The signal power was 18 dBm at the same point, and was limited by the maximum input power supported by the wavelength filter.

The wavelength separation of the LP_{01} and LP_{11} inputs, determined by earlier characterization of the IGV curves, was $\Delta\lambda_{ps} \approx 22.8$ nm. The two CW pumps were therefore placed in the L-band, while the signal was in the vicinity of 1550 nm. This also meant that the signal was amplified by a C-band EDFA whereas an L-band EDFA was used for the pumps. Pump to pump detuning ($\Delta\lambda_{pp}$) was chosen to be 7 nm (this will prove to be useful once multiple signals are used later on in the chapter), with $\lambda_{p1} = 1570$ nm. Given the constraint $\Delta\lambda_{ps} \approx 22.8$ nm, the signal wavelength was set to 1547.2 nm.

At the FMF output, the LP_{01} content was simply extracted by coupling the output light into a SMF (the pumps, being in a higher order mode, experienced much greater coupling losses). A filter and amplifier arrangement was used thereafter to extract the (data-carrying) idler and feed it to the receiver. An optical attenuator was used in order to obtain bit error rates (BERs) for varying values of idler OSNR.

The spectral content of light at different points after exiting the FMF is shown in Fig. 6.2. Each trace shown is normalized to its dominant tone. Fig. 6.2 (a) shows a spectral trace measured at the SMF right after the FMF. Some pump power leaked into the SMF (shown as 'LP_{11} leakage'); this was filtered away first (the passband was centred at the idler), leaving the signal and idler as the more prominent tones as shown in part (b).

The idler power was still relatively weak at this stage, however, with the signal 4 dB higher and even the LP_{11} pumps fairly close. This situation was partly remedied by passing the output represented in Fig. 6.2 (b) through a C-band EDFA. Only the idler and signal were appreciably amplified due to low gain at the pump frequencies, as shown in part (c). The output of the EDFA was passed through a another filter to extract the idler, which is shown in part (d). The idler, whose power at this point exceeded that of the signal by 48 dB, was then passed on to a BERT.

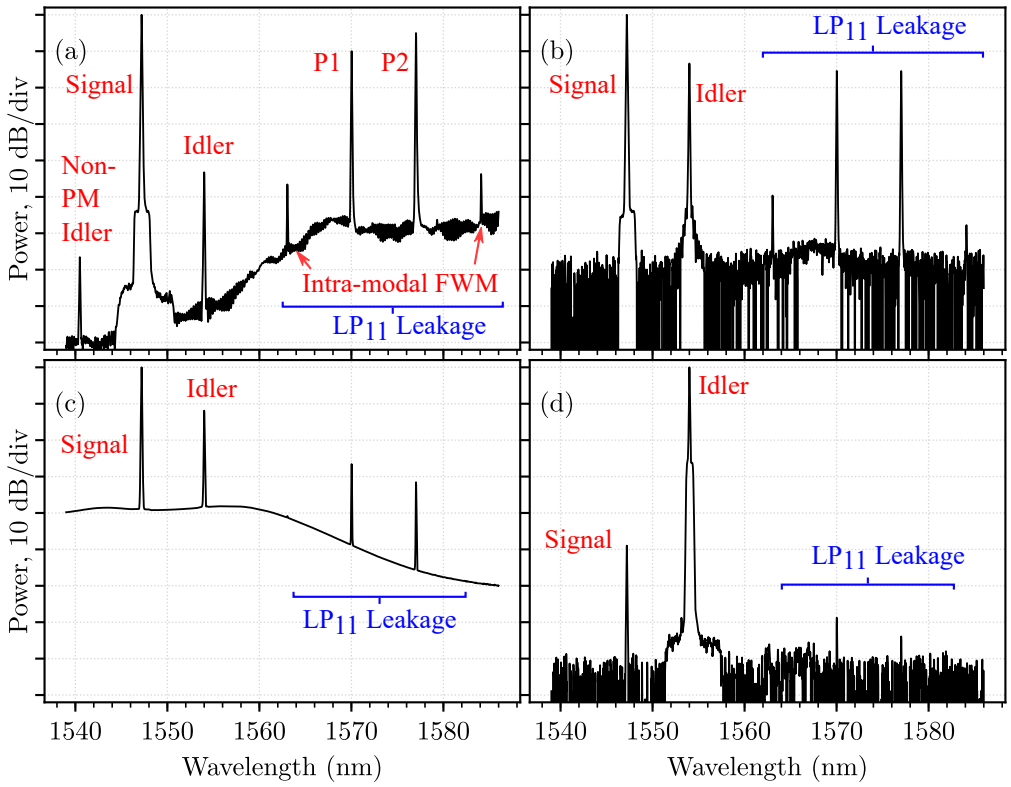

Figure 6.2. (a) to (d) show output spectra (each normalized to its dominant tone) at different stages of the setup. (a) Output spectrum at LP01 port. (b) Spectrum after passing through a low-loss filter. (c) After passing through C-Band EDFA. (d) After passing through the second filter.

The setup was able to provide and sustain error-free idler demodulation. Fig. 6.3 shows BER curves with and without the converter in place. The back-to-back (B2B) reference curve shows BER values obtained when the modulated signal was sent directly to the receiver and BERT. The IM FWM curve shows the same metrics for the (converted) idler field. The wavelength conversion causes a power penalty of 2 dB for a BER of $\approx 10^{-6}$, with no error floor being witnessed down to a BER of $\approx 10^{-11}$ (the lowest BER measured) despite the successive filtering stages that were used. While we have used single-channel OOK in this work, WDM transmission using IM FWM schemes that employ advanced modulation formats has also been successfully demonstrated recently [49], [97].

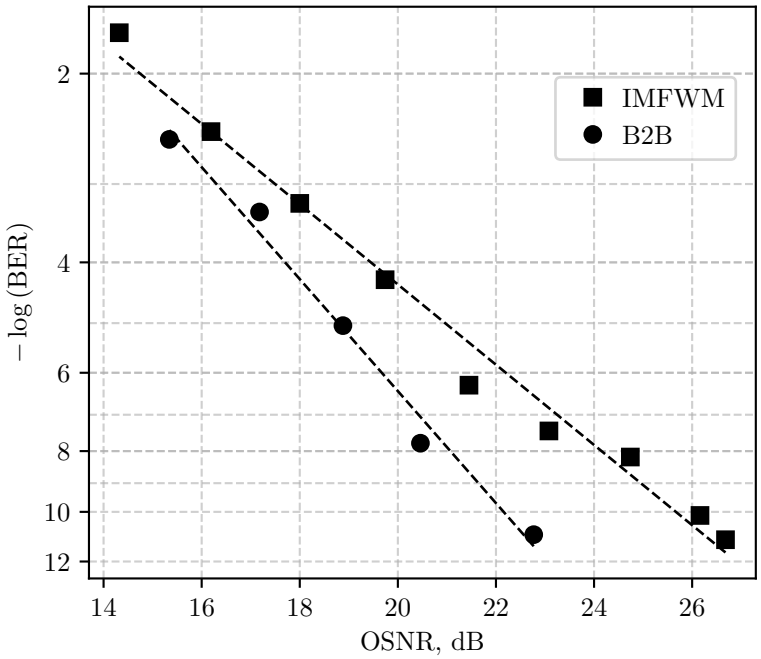

Figure 6.3. BER curve for the IM-FWM idler.

6.2 Selective Inter-modal Bragg Scattering

It has already been stated earlier in this work that in single mode devices efficient generation of parametric effects over broad spectral ranges is possible through sophisticated dispersion engineering that places constraints over the ZDW and necessitates a low dispersion parameter. However, if the objective were to act on a specific signal wavelength (such as for amplification or wavelength conversion), then accurate control over fourth-order dispersion (β_4) is needed [98], which is a non-trivial task because of the associated design and fabrication challenges.

Comparatively, we will see that IM FWM offers a more 'intrinsic' approach in achieving such selectivity. Our goal is to exploit IM FWM to obtain the selective conversion of a given signal from among a collection of signals on a frequency grid. In the next few sections, we investigate aspects that lead to a better understanding of how this can be experimentally realized.

6.2.1 BER sensitivity to signal wavelength

We start by measuring the sensitivity of BER to changes in signal wavelength. For the input configuration of the previous section/chapter, it is known that phase-matching is achieved for a relatively narrow band of signal wavelengths. This was demonstrated, for example, in Fig. 5.8, where appreciable CE was obtained for a limited range of values of signal-to-pump detuning $\Delta\lambda_{ps}$.

Therefore we should also expect to see a deterioration in BER as λ_s is moved away from the optimum. Fig. 6.4 shows the results of one such measurement. Here the optimal signal was located at 1550.9 nm (the pumps were situated so as to maintain $\Delta\lambda_{ps} \approx 22.8$ nm, pump to pump detuning was kept at 5.2 nm in this particular instance). As expected, it shows that the IM FWM idler BER is highly sensitive to changes in the phase-matched configuration, with transmission going from error-free to unreadable with as little as 30 GHz detuning of the signal from its optimum position.

While the sensitivity of BER to signal wavelength is not surprising - especially given the characterization carried out in the previous chapter - it points to the possibility that if this were a WDM experiment, very little idler generation would be observed for signals detuned from the current one (located at 193.3 THz) by 30 GHz or more. This is in contrast to, for example, a single

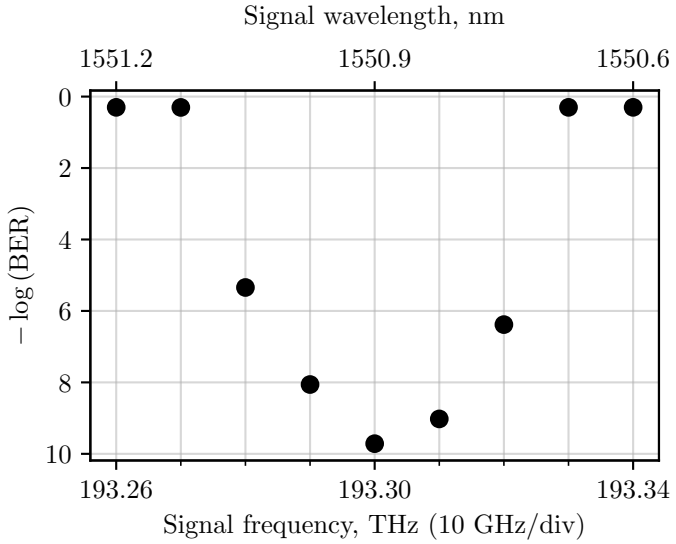

Figure 6.4. Variation of IM FWM BER with signal wavelength, with the optimum signal location at 1550.9 nm (193.3 THz).

mode wavelength converter, which is likely to accommodate a whole band of WDM signals at once [99].

An important fact relating to the above results must also be mentioned at this point: while idler generation was stable if the fibre was left unperturbed, it was sensitive to physical disturbances. That is, CE could be diminished if one were to appreciably displace the fibre from a position that resulted in efficient idler generation. This phenomenon has also been observed in very similar experiments elsewhere [86], and also points to a polarization dependence of the results.

It turns out, as we shall see later in this chapter, that the selective nature of IM FWM as well as the sensitivity of CE to fibre placement are both connected, and that selectivity involves more than just a consideration of the effects of changes in signal wavelength.

6.2.2 Scheme for selective inter-modal Bragg scattering

While we know that an idler experiences substantial gain inside a limited wavelength range, we have yet to describe how to switch conversion from one signal to another when there are multiple signals. We now describe how this is achieved.

Fig. 6.5 illustrates the principle of IM FWM Bragg-scattering in the configuration that has also been employed in the previous section, now with the addition of a second signal. The pumps (in mode LP_{11}) are at frequencies ω_{p1} and ω_{p2}, while the first of the two signals (in mode LP_{01}) lies at ω_s. As seen in the top part of Fig. 6.5, a Bragg Scattering idler, whose frequency is determined by energy conservation, emerges at $\omega_{\mathrm{BSr}} = \omega_s + \omega_{p2} - \omega_{p1}$ (see the wave marked as 'PM Idler' in the figure).

The (relative) IGV curves of the two participating modes are shown at the bottom of Fig. 6.5. Maximum idler generation at ω_{BSr} occurs when the signal is placed at a separation $\Delta\omega_{ps}$ from the pumps. Efficient conversion is not expected for additional signals present in its vicinity, such as the second signal shown in red in the Fig. 6.5,

It can also be inferred from this illustration that the higher the dispersion (or IGV slopes), the faster the 'average' IGVs get displaced from each other, and the narrower the bandwidth of signal frequencies over which idler gain is available.

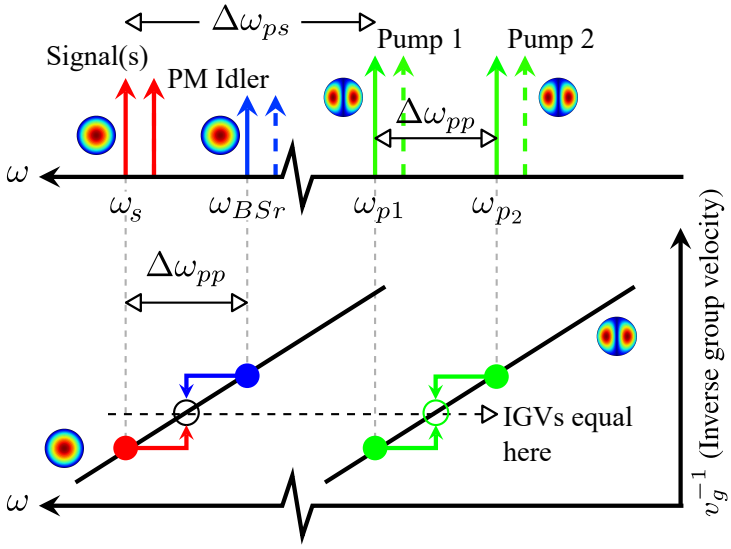

Figure 6.5. The wave configuration used in the experiment in which the pumps are in a higher order mode and the signal is in the fundamental mode. The modes and wavelengths are shown at the top, whereas the inverse group velocity curves and their relationship with phase matching are shown at the bottom.

However, we can select the signal to be converted by shifting the pump frequencies, given that the IGV curves in Fig. 6.5 are parallel. For example, in order to convert the second signal (shown to the right of ω_s) in Fig. 6.5, the pump frequencies need to be shifted to those given by the dashed green lines. This will result in idler generation at the dashed blue line being phase-matched (values of v_g^{-1} at the new average frequencies will match), whereas the first idler should now be far from phase-matching (provided that the dispersion is high enough).

6.2.3 Idler gain profile and pump polarization

The experimental set-up for investigating selective IM FWM is shown in Fig. 6.6, and is essentially a simplified version of the one presented in Fig. 6.1. All equipment required for (de)modulation was removed, and the (amplified) pump light successively went through a polarization controller, a polarizing beam splitter (PBS) and a rotating $\lambda/2$ plate in order to obtain linearly polarized light whose angle could be varied. The (LP_{01}) signal beam did not require amplification and went straight through to the fibre.

To gain insight into how the converter might behave in the case of multiple

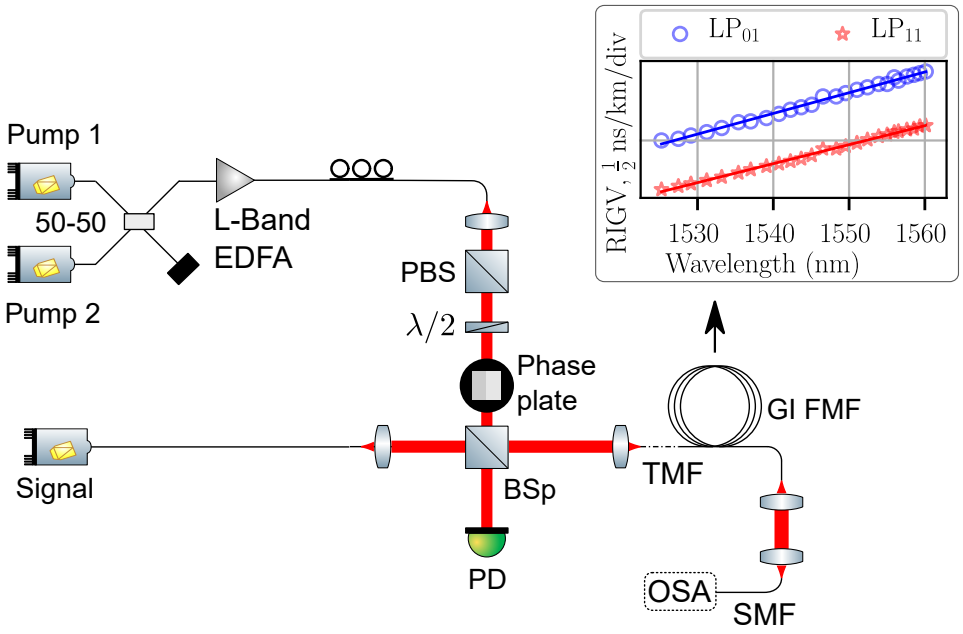

Figure 6.6. Experimental setup of the wavelength converter. Also shown are the relative inverse group velocity (or relative β_1) curves of modes LP_{01} and LP_{11} of the few-mode fiber.

channels, we first used a single signal using the Bragg scattering scheme of Fig. 6.5 and investigated the efficiency of idler generation around the optimum signal wavelength region (determined by the pump-signal spacing $\Delta\lambda_{ps}$). We set $\lambda_{p1} = 1570\,\text{nm}$ and $\lambda_{p2} = 1574\,\text{nm}$ (i.e. $\Delta\lambda_{pp} = 4\,\text{nm}$), and varied the (CW) signal wavelength around the phase-matched location. The combined pump power was estimated at 23.5 dBm at the input of the FMF; the input signal power was approximately 8.5 dBm. The pumps were linearly co-polarized, and their angle of polarization (with respect to a fixed direction orthogonal to the path of the beam) could be varied through the combination of a polarizer and $\lambda/2$ wave-plate. The state of polarization at the signal was not controlled or varied. The idler power as a function of signal wavelength was recorded for a number of different pump polarization angles, and a selection of such measurements for polarization angle increments of 45° is shown in Figs. 6.7 (a)-(c).

These results indicate that for a pair of pumps set at given wavelengths, the optimal signal separation $\Delta\omega_{ps}$ (and hence $\Delta\lambda_s$) is not strictly defined, and the idler gain does not always exhibit a global maximum at a single value of $\Delta\omega_{ps}$ (compare, for instance, Figs. 6.7(b) and 6.7(c)).

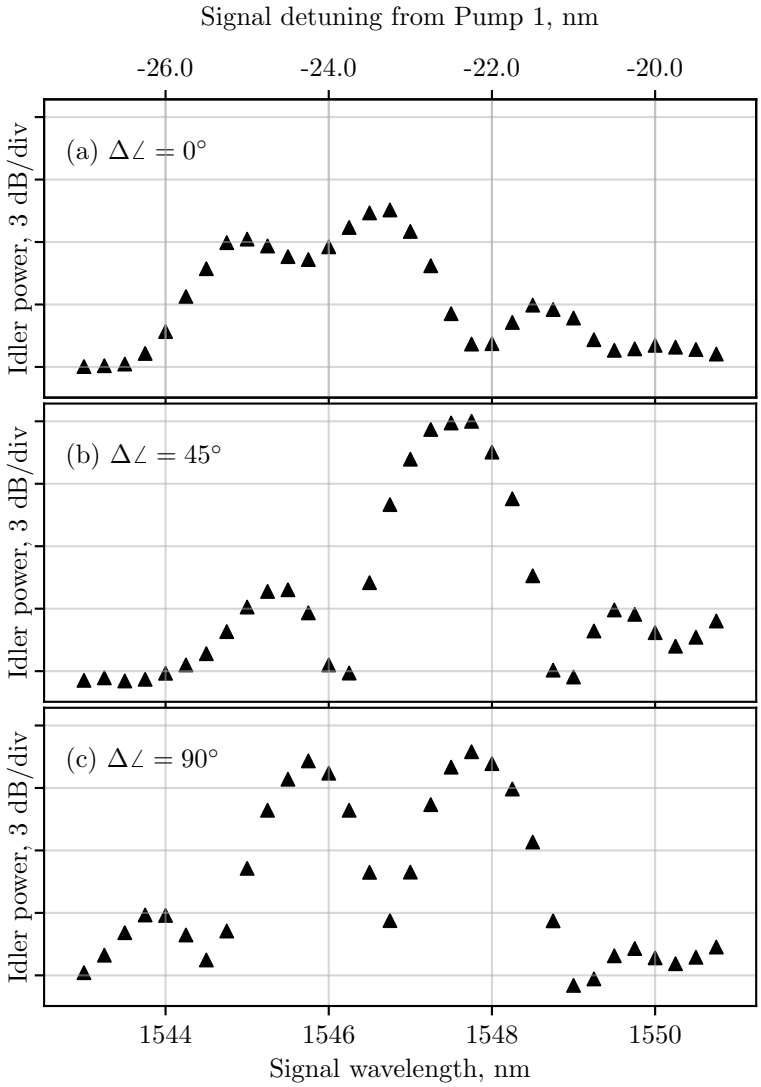

Figure 6.7. Dependence of gain profile on input polarization angle.

While the above results were obtained with linearly polarized pumps, it was seen that by changing the pump SOP arbitrarily (i.e. by removing the PBS and adjusting the polarization controller so that the state was no longer linear), it was possible to obtain gain profiles exhibiting narrower peaks. One such example is shown in Fig. 6.8 ($\Delta\lambda_{pp} = 5\,\text{nm}$ here). The local minima adjacent to the global peak at 1547 nm are each located about 100 GHz away from it, and the 3-dB bandwidth of the central peak is 0.74 nm (approximately 90 GHz). These results were stable over long periods of time and repeatable, provided that the fibre was not deliberately perturbed.

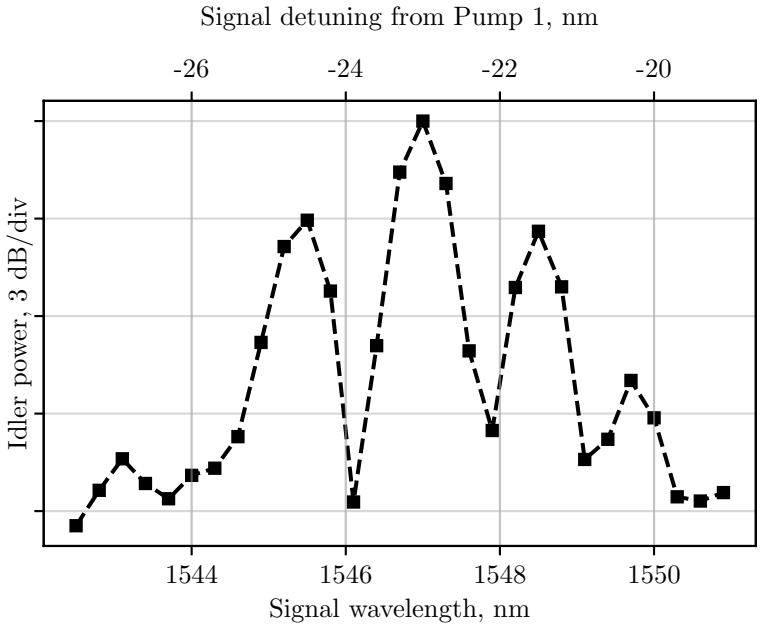

Figure 6.8. Variation of (normalized) idler power with signal wavelength in the case when pump polarization is chosen to give narrow bandwidth peaks.

6.3 Analysis

In order to explain the variation of idler gain observed above, we begin with a reminder that optical fibres are subject to manufacturing imperfections, environmental variations and local mechanical stress that induce random perturbations in the fibre structure. As explained in earlier chapters, this breaks the degeneracy of modes in the same group, which separate into a distinct set of quasi-degenerate modes. Differently from degenerate modes, all of which possess the same effective index n, quasi-degenerate modes are characterized by distinct indices that are slightly different. We indicate the difference $n_j - n_k$ between the effective indexes n_j and n_k of the LP modes j and k with $\Delta n_{j,k}$.

Based on the above paragraph, we may reason that the IM FWM gain curves measured earlier cannot be explained only by specifying the overall mode group(s) involved, rather this will also require a consideration of the *intra*-group parameters. In order to do the above, we first present a summary of a computational investigation into the topic by Dr. Guasoni [55]. This will be followed by an experimental test of our hypothesis.

6.3.1 Computational study

In telecom SMFs, the fundamental mode has been widely studied; it is well known that $\Delta n_{01x,01y}$ (i.e. the effective index difference between the two polarization modes) is of the order of 10^{-8} - 10^{-7} [89]. On the other hand, measurements of the index difference among polarization modes of the LP_{11} group have not been widely reported. Finite-element-method simulations to compute the modes of group LP_{11} and their effective indices in the presence of weak perturbations of the fibre structure (such as might result from a slight ellipticity of the transverse section) reveal that $\Delta n_{11ax,11ay}$ and $\Delta n_{11bx,11by}$ are also of the order of 10^{-8} - 10^{-7} [55]. However, the index difference between one mode of subgroup LP_{11a} and one mode of subgroup LP_{11b}, as for example $\Delta n_{11ax,11bx}$ or $\Delta n_{11ax,11by}$, is typically two orders of magnitude larger.[1] Associated with the effective index difference between subgroups LP_{11a} and LP_{11b} is a group delay. This implies that the phase matching condition for both of these modes is not the same.

In practice, this means that two distinct IM FWM processes are possible, each involving mode LP_{01} and one of the LP_{11a} and LP_{11b} modes. Simulations in [55], based on the same principles of random birefringence described in Chapter 4, show that in the hypothetical case when all the pump energy is confined in either the LP_{11a} or LP_{11b} modes, the respective (calculated) gain curves are as shown in Figure 6.9(a). The idler gain is maximized at distinctly different wavelengths for the two curves.

However, when the input pumps are coupled to subgroups LP_{11a} and LP_{11b}, both are simultaneously involved in the IM FWM process. Now, the gain curve depends on the specific amount of power coupled into the two subgroups, and can take a form that is a composite of the two curves presented in Fig. 6.9(a). Some examples of this are presented in Fig. 6.9(b). In broad terms, the composite gain is a combination of the LP_{11a}- and LP_{11b}-only gain curves and may exhibit multiple peaks whose wavelengths may not coincide with those observed in Fig. 6.9(a).

There is good agreement between the computed results in Fig. 6.9 and the measured data presented earlier in Fig. 6.7. The situation can therefore be described as follows: by varying the polarization angle of the pump beam at

[1] This substantial difference can be attributed to the differing spatial distributions of modes in subgroups LP_{11a} and LP_{11b} [55].

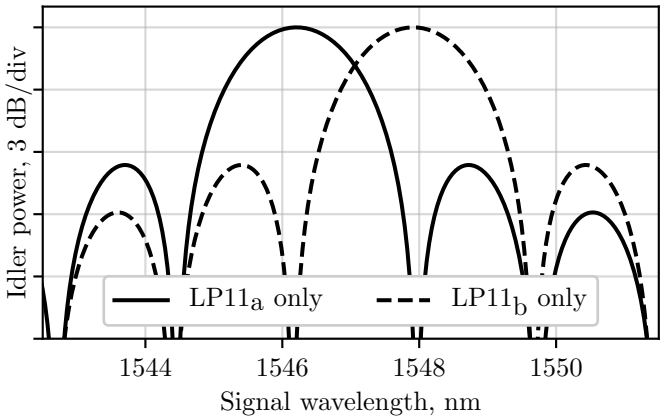

(a)

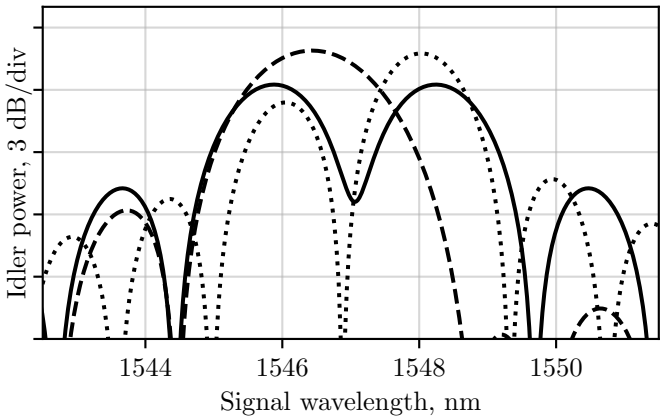

(b)

Figure 6.9. (a) Gain profiles in which pump energy is contained exclusively in either LP_{11a} or LP_{11b}. (b) gain profiles in which pump energy is coupled to both subgroups [55].

the fibre input, we effectively change the amount of pump power coupled to subgroups LP_{11a} and LP_{11b} into the fibre. Specifically, the LP_{11} pump at ω_{p1} experiences a change in the distribution of power between subgroups LP_{11a} and LP_{11b} (ditto for the pump at ω_{p2}). Hence, following the reasoning given in the preceding paragraphs, this results in a change in the shape of the gain profile.

6.3.2 Experimental verification

We now demonstrate an experimental test of the effect of the quasi-degeneracy of the LP_{11} group. Based on our postulate that this HOM degeneracy is the underlying reason for the variation in the gain curves, we should expect that if the input configuration is changed to one in which the pumps are in the fundamental (LP_{01}) mode group and the signal is in LP_{11}, there should be minimal impact of pump polarization on idler gain. This is because when we vary the polarization of the pump beams so as to change the amount of pump power coupled to the LP_{01x} and LP_{01y} modes, the differential group velocity among them (LP_{01x} and LP_{01y}) is extremely small when compared to the previous case, which results in a (computed) range of tunability of peak gain as small as 0.1 nm. Since this range is much smaller than the gain bandwidth, in practice we should not observe any difference in the gain profile, regardless of the input polarization of the pumps.

This was experimentally realised by switching the pumps to LP_{01} and letting $\lambda_{p1} = 1550\,\text{nm}$ and $\lambda_{p2} = 1554\,\text{nm}$, while varying the LP_{11} signal around

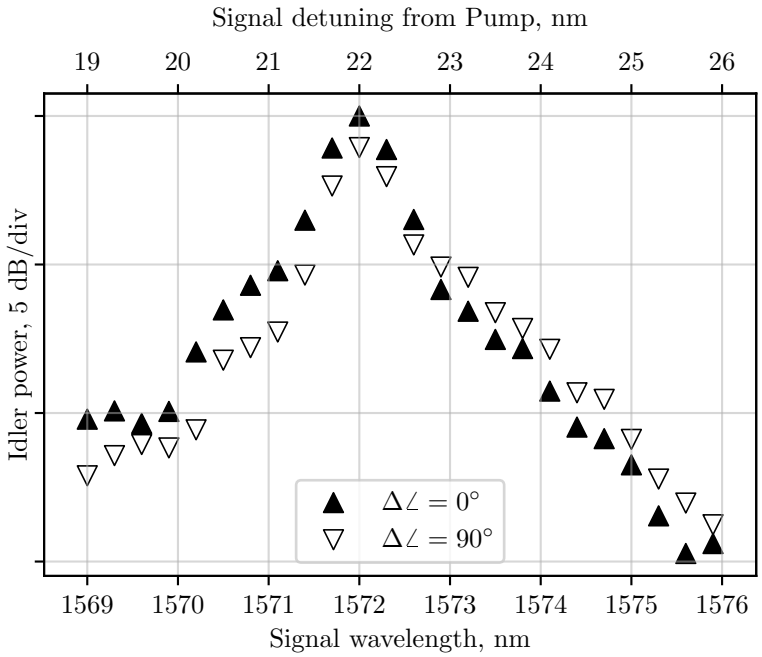

Figure 6.10. Change in idler power profile when the mode configuration is switched to having the pumps in the fundamental mode and the signal in the higher order mode.

the optimum offset ($\Delta\lambda_{ps} \approx 22.8\,\text{nm}$). A mode demultiplexer was set up to accept the LP_{11} fields. The idler gain profile is shown in Fig. 6.10. As expected, in this modified configuration, it was observed that changing the pump polarization has a minor impact on the overall shape of the profile (compare with Fig. 6.7).

6.4 Selective channel conversion

With the details relating to pump-polarization and gain spectra analysed above, we are now in a position to present the case in which multiple signal channels are launched into the wavelength converter, with the objective of converting each of them selectively.

The input configuration shown in Fig. 6.5 was employed, now with three signal inputs with equal powers. The experimental setup was thus very similar to the one shown in Fig. 6.1. Three signal channels centred at 193.3 THz ($\approx$ 1550.9 nm) and separated by 100 GHz ($\approx$ 0.8 nm) were amplified and launched into the LP_{01} mode with a total power of 18 dBm into the fibre. After signal amplification, any ASE from the EDFA outside the band of the signals was filtered away to preserve the OSNR of the generated IM FWM idlers. The polarization of the input signals was kept linear and co-polarized to one another.

The spectra in Figs. 6.11(a)-(c) show experimental results obtained as the two pumps were tuned in increments of 100 GHz. The signals are denoted by $\lambda_i\,(i = 1, 2, 3)$ and the corresponding IM FWM idlers are labelled λ_i'. The pumps are labelled as P1 and P2, and $\Delta\lambda_{ps}$ was kept equal to 22.8 nm at all times, i.e. the wavelength separation between the signal of interest and the pumps was kept at this fixed value. To keep the idlers well separated in wavelength from the signals, $\Delta\lambda_{pp}$ was maintained at 5.15 nm. The sharp drop in power around the spectral region of the signals is due to the filtering mentioned above. Also visible are idler peaks resulting from intra-modal FWM among the signals in LP_{01}, at either side of the signal wavelengths.

Once the pump wavelengths had been tuned appropriately for conversion of a given channel, a polarization controller was used to adjust pump polarization (not necessarily linear) to further enhance idler selectivity. Fig. 6.11(a) shows Pump 1 (P1) and signal λ_1 separated by about 22.8 nm from each other. Clearly, out of the three signals, λ_1 is converted most efficiently to the idler

denoted by λ_1', with an extinction ratio of about 16 dB relative to the other idlers. Next, by tuning the pumps to achieve a separation of 22.8 nm with signal λ_2, and subsequently adjusting (pump) polarization to optimize idler generation at λ_2' results in the situation in Fig. 6.11(b). Similarly, Fig. 6.11(c) shows the case for the selective generation of idler λ_3'. In all cases, extinction ratios in excess of 10.0 dB were achieved.

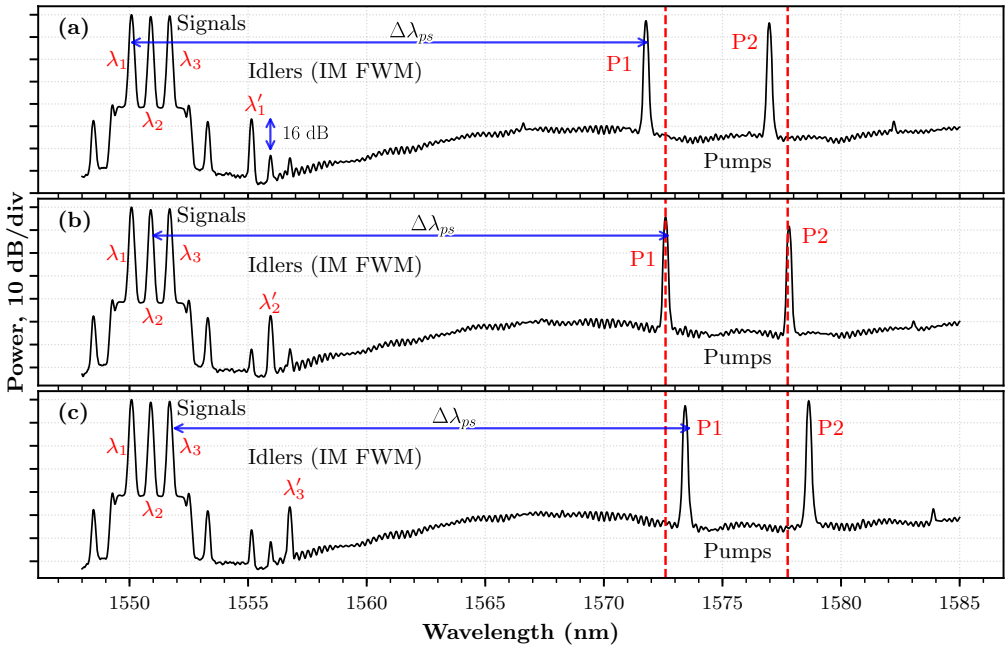

Figure 6.11. (a)-(c) Spectra at the LP_{01} port when the pumps are scanned in increments of 100 GHz for conversion to idlers λ_1', λ_2' and λ_3' respectively.

6.5 Conclusions

The viability of IM FWM for accomplishing a range of signal processing functionalities rests on its ability to provide stable results with acceptable OSNR penalties. In this chapter we have shown that, for an intensity modulated signal, this goal is reachable provided that external mechanical influences on the setup can be kept in check. Waveguides design and materials which may provide higher gain should only improve upon the results presented, and continuing research on the subject utilizing advanced modulation formats has also shown promising results [49].

It was stated at the outset of this work that FMFs offer additional degrees of freedom in the implementation of certain nonlinear signal processes. One demonstration of this was made in this chapter by the selective conversion of (any) one out of three signal channels with adjacent-channel spacing of 100 GHz. This was achieved by using pump wavelength in conjunction with (pump) polarization – which effectively controlled coupling to the individual spatial modes within the LP_{11} mode group – to tune the idler gain profile. Power extinction between the channel of interest and the other wavelength channels ranged from 10 dB to 16 dB. Finer and stronger selectivity should be achievable by dispersion engineering of the modes, with constraints on dispersion properties less stringent than in schemes meant for SMFs [98].

Chapter 7

Summary and outlook

7.1 Synopsis

The topics investigated in this thesis were motivated by the potential of multimode nonlinear optical processes for a variety of applications, including optical signal processing (OSP). This potential stems from the fact that multimode waveguides offer means for the phase matching of FWM processes with enhanced flexibility (compared with single mode devices), and in conjunction with advancements in the area of spatially multiplexed optical communications has driven the need for further study of their efficiency, limitations and practicality. As a prelude to the subject of inter-modal interactions, the thesis began (Chapter 2) with an investigation into the nature of linear propagation (of mode LP_{11}) in a birefringent higher-order mode (HOM) fibre, studying the influence of input polarization on its spatial output. Using this fibre, it was shown that it is possible to optimally modulate the output beam shape by changing input polarization given a particular combination of a) input beam orientation and b) propagation distance.

Chapters 3 to 6 studied various aspects of inter-modal nonlinearities. In Chapter 3, the phase matching considerations for efficient intra- and inter-modal FWM interactions were juxtaposed. The conversion efficiency (CE) bandwidth of intra-modal FWM was dependent on the absolute value of group velocity dispersion; on the other hand the scheme presented for inter-modal four-wave mixing (IM FWM) relied on having a constant differential mode delay (between the participating modes) with respect to wavelength, regardless of its actual value. IM FWM CE (and its bandwidth) for the three-mode

fibre employed in our experiments fell short of the figures obtained for the single-mode fibres tested (an explanation for this had to wait until Chapter 5). Chapter 4 took a deeper look at the dependence of idler generation on the states of polarization (SOPs) of the applied inputs, and a configuration yielding polarization insensitive wavelength conversion was identified. This effect was explained by consideration of the residual birefringence of the fibre under investigation. Moreover, the relative pump polarization was found to be a significant factor for CE overall. The scheme we employed (constant modal delay) presented the tempting opportunity to exploit IM FWM for large CE bandwidths by tailoring the modes of a few-mode fibre (FMF) to have parallel inverse group velocity (IGV) curves. A number of fibres were fabricated for this purpose in collaboration with Sumitomo (Japan). While they gave much improved results compared with those obtained for the three-mode fibre explored earlier, the potential of this technique was compromised by the effects of fibre randomness. The idea however, was seized by our colleagues in silicon photonics and employed with remarkable success in silicon-nitride planar waveguides. In Chapter 6, the same dispersion characteristics were used for achieving the selective conversion of a chosen signal from within a set of wavelength multiplexed signals. Here, a dependence of the idler gain profile on pump polarization was observed, and a complete explanation of this involved consideration of the intra-group parameters of the modes involved; theoretical and experimental validation of our assertions was provided. Stable and error free idler demodulation was also demonstrated in this chapter.

7.2 Future directions

When viewed in the context of nonlinear signal processing, inter-modal processes firstly offer ways to replicate much of the functionality that has been implemented in single-mode devices, but with greater flexibility afforded by the additional spatial degree of freedom. Secondly, they present opportunities for extending the range of processing capabilities of the latter. Additionally, they possess the advantage of being closely compatible with future communications systems that may employ spatial multiplexing. However, given that single-mode devices have been under research and development for much longer, further work will need to be done in order to catch up and to fully bring the potential advantages of multimode nonlinearities to fruition.

One direction of future research is to further extend the range of frequencies and modes over which we have operated. In order to focus on fundamental properties, and being limited by the laser sources available, we chose to investigate inter-modal interactions between the LP_{01} and LP_{11} modes with frequencies in the C- and L-bands. However, the same method(s) can be applied to higher-order modes and frequencies beyond those mentioned. This would be a means of simultaneously converting (or amplifying) signals in different and widely separated spectral regions by individually addressing the phase matching characteristics (and therefore dispersion) of different modes of one single fibre. This concept is illustrated in Fig. 7.1.

This and similar applications of IM FWM based on the configuration illustrated here would require refinements in waveguide design (dispersion engineering) in order to a) phase-match the interaction for all modes and b) support the broadband conversion of (multiple) signals in each mode. Another consideration would be nonlinear limits to input power. This would require an investigation of inter-modal (plus intra-modal) cross-talk between the various signals/modes and the extent of their impairment on transmission quality. Efficient ways to multiplex and demultiplex the different modes will also be required: given that the use of beam-splitters rapidly diminishes available OSNR, holographic approaches are being considered for this purpose [38]. Moreover, IM FWM also relies on the degree of spatial overlap between modes, therefore not all pairs of modes (especially higher-order modes) will be equal in terms of IM FWM efficiency. Inevitably, constraints relating to the optimiza-

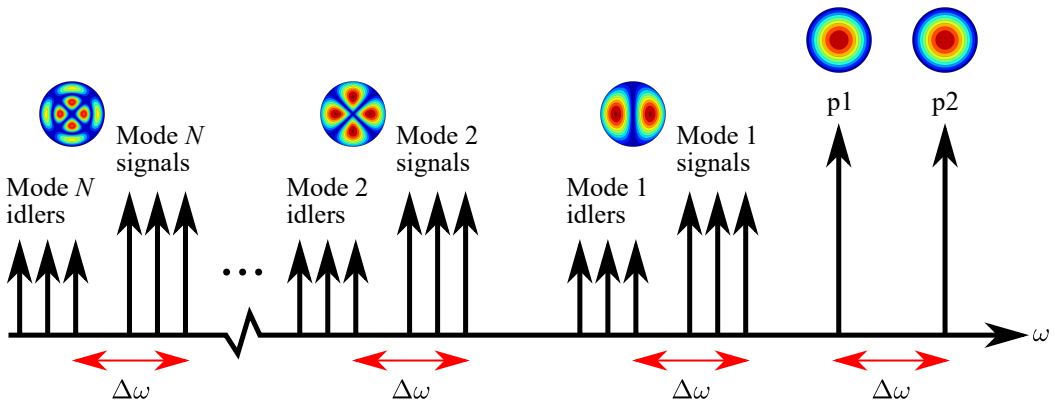

Figure 7.1. A scheme for simultaneous conversion of signals in multiple frequency bands spanning multiple spatial modes. This exploits the red-shifted Bragg scattering idler, as discussed in Chapter 5.

tion of all of these factors will exist, and further theoretical and experimental work can help specify them. In addition to the scheme presented in Fig. 7.1, configurations employing pumps in different spatial modes may also be considered (these will be similar to the configuration tested in Chapter 3) depending on the particular application.

Given that parametric interactions are particularly susceptible to random fluctuations in fibre parameters that inevitably result from mechanical stimuli, it appears that for broadband operation, the short lengths and higher nonlinearity of silicon based waveguides make them an attractive alternative. The best IM FWM CE bandwidths obtained in our labs for Si_xN_y (silicon nitride) waveguides exceed those for MMFs investigated in this thesis by a factor of 4 or higher [94].

IM FWM can be investigated in tandem with research on new materials for nonlinear photonics. One example are chalcogenide glasses, which have been found to possess Kerr nonlinearities higher by three orders of magnitude as compared to silica, and have attractive transmission properties in the mid-infrared [100]–[102].

Moreover, as suggested earlier, IM FWM processes and techniques can be used to enhance the operation of devices that may be limited by single-moded operation in a large number of nonlinear applications. IM FWM has recently been used in silicon waveguides to generate idlers far from pump wavelengths (and hence also the associated noise) to obtain broadband generation of heralded single photons in the mid-infrared, without the need for spectral filtering [103]. Advantages of using IM FWM processes in high power fibre lasers and resonant ring structures can be explored likewise.

In this concluding section, and in places elsewhere in this thesis, an attempt has been made to point toward and/or demonstrate aspects of intermodal parametric interactions that are enabled by distinctly different designs as compared with those of single-mode waveguides, and have potential (proven in some cases) for overcoming the shortcomings of the latter. In light of these examples, further research into multi-mode nonlinearities promises to be a rewarding endeavour rich in interdisciplinary connections.

Bibliography

[1] R. H. Stolen, J. E. Bjorkholm, and A. Ashkin, "Phase-matched three-wave mixing in silica fiber optical waveguides," *Applied Physics Letters*, vol. 24, no. 7, pp. 308–310, 1974.

[2] P. Thomas, N. Rowell, H. Van Driel, and G. Stegeman, "Normal acoustic modes and brillouin scattering in single-mode optical fibers," *Physical review B*, vol. 19, no. 10, p. 4986, 1979.

[3] R. H. Stolen, E. Ippen, and A. Tynes, "Raman oscillation in glass optical waveguide," *Applied Physics Letters*, vol. 20, no. 2, pp. 62–64, 1972.

[4] R. Essiambre, G. Kramer, P. J. Winzer, G. J. Foschini, and B. Goebel, "Capacity limits of optical fiber networks," *Journal of Lightwave Technology*, vol. 28, no. 4, pp. 662–701, 2010.

[5] P. P. Mitra and J. B. Stark, "Nonlinear limits to the information capacity of optical fibre communications," *Nature*, vol. 411, no. 6841, pp. 1027–1030, 2001.

[6] G. Kaiser, *Optical Fiber Communications*. McGraw-Hill, 2013.

[7] A. E. Willner, S. Khaleghi, M. R. Chitgarha, and O. F. Yilmaz, "All-optical signal processing," *Journal of Lightwave Technology*, vol. 32, no. 4, pp. 660–680, 2013.

[8] P. Winzer and R.-J. Essiambre, "Advanced optical modulation formats," *Proceedings of the IEEE*, vol. 94, no. 5, May 2006.

[9] Y. Aoki, "Properties of fiber raman amplifiers and their applicability to digital optical communication systems," *Journal of Lightwave Technology*, vol. 6, no. 7, pp. 1225–1239, 1988.

[10] A. Hasegawa and F. Tappert, "Transmission of stationary nonlinear optical pulses in dispersive dielectric fibers. i. anomalous dispersion," *Applied Physics Letters*, vol. 23, no. 3, pp. 142–144, 1973.

[11] W. Tomlinson, R. Stolen, and C. Shank, "Compression of optical pulses chirped by self-phase modulation in fibers," *JOSA B*, vol. 1, no. 2, pp. 139–149, 1984.

[12] D. F. Grosz, A. Agarwal, S. Banerjee, D. N. Maywar, and A. P. Kung, "All-raman ultralong-haul single-wideband dwdm transmission systems with oadm capability," *Journal of Lightwave Technology*, vol. 22, no. 2, pp. 423–432, 2004.

[13] A. Chong, W. H. Renninger, and F. W. Wise, "All-normal-dispersion femtosecond fiber laser with pulse energy above 20nj," *Optics letters*, vol. 32, no. 16, pp. 2408–2410, 2007.

[14] B. R. Washburn, S. A. Diddams, N. R. Newbury, J. W. Nicholson, M. F. Yan, and C. G. Jørgensen, "Phase-locked, erbium-fiber-laser-based frequency comb in the near infrared," *Optics letters*, vol. 29, no. 3, pp. 250–252, 2004.

[15] R. Slavík, F. Parmigiani, J. Kakande, C. Lundström, M. Sjödin, P. A. Andrekson, R. Weerasuriya, S. Sygletos, A. D. Ellis, L. Grüner-Nielsen, *et al.*, "All-optical phase and amplitude regenerator for next-generation telecommunications systems," *Nature Photonics*, vol. 4, no. 10, pp. 690–695, 2010.

[16] N. Shibata, R. Braun, and R. Waarts, "Phase-mismatch dependence of efficiency of wave generation through four-wave mixing in a single-mode optical fiber," *IEEE Journal of Quantum Electronics*, vol. 23, no. 7, pp. 1205–1210, 1987.

[17] F. Yaman, Q. Lin, S. Radic, and G. P. Agrawal, "Impact of dispersion fluctuations on dual-pump fiber-optic parametric amplifiers," *IEEE Photonics Technology Letters*, vol. 16, no. 5, pp. 1292–1294, May 2004, ISSN: 1941-0174.

[18] M. E. Marhic, N. Kagi, T.-K. Chiang, and L. G. Kazovsky, "Broadband fiber optical parametric amplifiers," *Opt. Lett.*, vol. 21, no. 8, pp. 573–575, Apr. 1996.

[19] M. A. Foster, A. C. Turner, J. E. Sharping, B. S. Schmidt, M. Lipson, and A. L. Gaeta, "Broad-band optical parametric gain on a silicon photonic chip," *Nature*, vol. 441, no. 7096, pp. 960–963, 2006.

[20] G. Kalogerakis, M. E. Marhic, K. K. Y. Wong, and L. G. Kazovsky, "Transmission of optical communication signals by distributed parametric amplification," *Journal of Lightwave Technology*, vol. 23, no. 10, pp. 2945–2953, Oct. 2005, ISSN: 0733-8724.

[21] J. Hansryd, P. A. Andrekson, M. Westlund, J. Li, and P. O. Hedekvist, "Fiber-based optical parametric amplifiers and their applications," *IEEE Journal of Selected Topics in Quantum Electronics*, vol. 8, no. 3, pp. 506–520, 2002.

[22] F. G. Omenetto, A. J. Taylor, M. D. Moores, J. Arriaga, J. C. Knight, W. J. Wadsworth, and P. S. J. Russell, "Simultaneous generation of spectrally distinct third harmonics in a photonic crystal fiber," *Opt. Lett.*, vol. 26, no. 15, pp. 1158–1160, Aug. 2001.

[23] S. Berdagué and P. Facq, "Mode division multiplexing in optical fibers," *Applied optics*, vol. 21, no. 11, pp. 1950–1955, 1982.

[24] W. Thornburg, B. Corrado, and X. Zhu, "Selective launching of higher-order modes into an optical fiber with an optical phase shifter," *Optics letters*, vol. 19, no. 7, pp. 454–456, 1994.

[25] F. Yaman, N. Bai, B. Zhu, T. Wang, and G. Li, "Long distance transmission in few-mode fibers," *Optics Express*, vol. 18, no. 12, pp. 13 250–13 257, 2010.

[26] R. Ryf, S. Randel, A. H. Gnauck, C. Bolle, A. Sierra, S. Mumtaz, M. Esmaeelpour, E. C. Burrows, R. Essiambre, P. J. Winzer, D. W. Peckham, A. H. McCurdy, and R. Lingle, "Mode-division multiplexing over 96 km of few-mode fiber using coherent 6 $\times$ 6 mimo processing," *Journal of Lightwave Technology*, vol. 30, no. 4, pp. 521–531, 2012.

[27] C. Koebele, M. Salsi, D. Sperti, P. Tran, P. Brindel, H. Mardoyan, S. Bigo, A. Boutin, F. Verluise, P. Sillard, *et al.*, "Two mode transmission at 2x100gb/s, over 40km-long prototype few-mode fiber, using lcos-based programmable mode multiplexer and demultiplexer," *Optics express*, vol. 19, no. 17, pp. 16 593–16 600, 2011.

[28] S. Randel, R. Ryf, A. Sierra, P. J. Winzer, A. H. Gnauck, C. A. Bolle, R.-J. Essiambre, D. W. Peckham, A. McCurdy, and R. Lingle, "6$\times$56-gb/s mode-division multiplexed transmission over 33-km few-mode fiber

enabled by 6×6 mimo equalization," *Opt. Express*, vol. 19, no. 17, pp. 16 697–16 707, Aug. 2011.

[29] R. Di Leonardo and S. Bianchi, "Hologram transmission through multi-mode optical fibers," *Optics express*, vol. 19, no. 1, pp. 247–254, 2011.

[30] G. Stepniak, L. Maksymiuk, and J. Siuzdak, "Binary-phase spatial light filters for mode-selective excitation of multimode fibers," *Journal of lightwave technology*, vol. 29, no. 13, pp. 1980–1987, 2011.

[31] J. Carpenter and T. D. Wilkinson, "All optical mode-multiplexing using holography and multimode fiber couplers," *Journal of Lightwave Technology*, vol. 30, no. 12, pp. 1978–1984, 2012.

[32] D. Flamm, D. Naidoo, C. Schulze, A. Forbes, and M. Duparré, "Mode analysis with a spatial light modulator as a correlation filter," *Optics letters*, vol. 37, no. 13, pp. 2478–2480, 2012.

[33] M. Mazur, N. K. Fontaine, R. Ryf, H. Chen, D. T. Neilson, M. Bigot-Astruc, F. Achten, P. Sillard, A. Amezcua-Correa, J. Schröder, *et al.*, "Characterization of long multi-mode fiber links using digital holography," in *Optical Fiber Communication Conference*, Optical Society of America, 2019, W4C–5.

[34] W. S. Mohammed, M. Pitchumani, A. A. Mehta, and E. G. Johnson, "Selective excitation of the LP11 mode in step index fiber using a phase mask," *Optical Engineering*, vol. 45, no. 7, pp. 1–7, 2006.

[35] R. Ryf, C. Bolle, and J. von Hoyningen-Huene, "Optical coupling components for spatial multiplexing in multi-mode fibers," in *European Conference and Exposition on Optical Communications*, Optical Society of America, 2011, Th–12.

[36] K. Igarashi, D. Souma, T. Tsuritani, and I. Morita, "Performance evaluation of selective mode conversion based on phase plates for a 10-mode fiber," *Opt. Express*, vol. 22, no. 17, pp. 20 881–20 893, Aug. 2014.

[37] S. Bade, B. Denolle, G. Trunet, N. Riguet, P. Jian, O. Pinel, and G. Labroille, "Fabrication and characterization of a mode-selective 45-mode spatial multiplexer based on multi-plane light conversion," in *2018 Optical Fiber Communications Conference and Exposition (OFC)*, IEEE, 2018, pp. 1–3.

[38] N. K. Fontaine, R. Ryf, H. Chen, D. T. Neilson, K. Kim, and J. Carpenter, "Laguerre-gaussian mode sorter," *Nature communications*, vol. 10, no. 1, pp. 1–7, 2019.

[39] S. G. Leon-Saval, N. K. Fontaine, J. R. Salazar-Gil, B. Ercan, R. Ryf, and J. Bland-Hawthorn, "Mode-selective photonic lanterns for space-division multiplexing," *Opt. Express*, vol. 22, no. 1, pp. 1036–1044, Jan. 2014.

[40] N. Riesen, S. Gross, J. D. Love, and M. J. Withford, "Femtosecond direct-written integrated mode couplers," *Optics express*, vol. 22, no. 24, pp. 29 855–29 861, 2014.

[41] L. G. Wright, Z. M. Ziegler, P. M. Lushnikov, Z. Zhu, M. A. Eftekhar, D. N. Christodoulides, and F. W. Wise, "Multimode nonlinear fiber optics: Massively parallel numerical solver, tutorial, and outlook," *IEEE Journal of Selected Topics in Quantum Electronics*, vol. 24, no. 3, pp. 1–16, 2018.

[42] J. Cheng, M. E. V. Pedersen, K. Charan, K. Wang, C. Xu, L. Grüner-Nielsen, and D. Jakobsen, "Intermodal Čerenkov radiation in a higher-order-mode fiber," *Opt. Lett.*, vol. 37, no. 21, pp. 4410–4412, Nov. 2012.

[43] M. A. Eftekhar, L. G. Wright, M. S. Mills, M. Kolesik, R. A. Correa, F. W. Wise, and D. N. Christodoulides, "Versatile supercontinuum generation in parabolic multimode optical fibers," *Opt. Express*, vol. 25, no. 8, pp. 9078–9087, Apr. 2017.

[44] F. Poletti and P. Horak, "Dynamics of femtosecond supercontinuum generation in multimode fibers," *Opt. Express*, vol. 17, no. 8, pp. 6134–6147, Apr. 2009.

[45] R. J. Essiambre, M. A. Mestre, R. Ryf, A. H. Gnauck, R. W. Tkach, A. R. Chraplyvy, Y. Sun, X. Jiang, and R. Lingle, "Experimental investigation of inter-modal four-wave mixing in few-mode fibers," *IEEE Photonics Technology Letters*, vol. 25, no. 6, pp. 539–542, Mar. 2013, ISSN: 1041-1135.

[46] R. J. Essiambre, M. A. Mestre, R. Ryf, A. H. Gnauck, R. W. Tkach, A. R. Chraplyvy, Y. Sun, X. Jiang, and R. Lingle, "Experimental observation of inter-modal cross-phase modulation in few-mode fibers," *IEEE Photonics Technology Letters*, vol. 25, no. 6, pp. 535–538, Mar. 2013, ISSN: 1041-1135.

[47] M. Guasoni, F. Parmigiani, P. Horak, and D. J. Richardson, "Novel fiber design for wideband conversion and amplification in multimode fibers," in *2017 European Conference on Optical Communication (ECOC)*, 2017, pp. 1–3.

[48] F. Parmigiani, P. Horak, Y. Jung, L. Grüner-Nielsen, T. Geisler, P. Petropoulos, and D. J. Richardson, "All-optical mode and wavelength converter based on parametric processes in a three-mode fiber," *Opt. Express*, vol. 25, no. 26, pp. 33 602–33 609, Dec. 2017.

[49] G. Rademacher, R. S. Luís, B. J. Puttnam, Y. Awaji, M. Suzuki, T. Hasegawa, and N. Wada, "Wide-band intermodal wavelength conversion in a dispersion engineered highly nonlinear fmf," in *2019 Optical Fiber Communications Conference and Exhibition (OFC)*, Mar. 2019.

[50] T. Čižmár and K. Dholakia, "Shaping the light transmission through a multimode optical fibre: Complex transformation analysis and applications in biophotonics," *Optics Express*, vol. 19, no. 20, pp. 18 871–18 884, 2011.

[51] J. Carpenter, B. J. Eggleton, and J. Schröder, "Maximally efficient imaging through multimode fiber," in *2014 Conference on Lasers and Electro-Optics (CLEO) - Laser Science to Photonic Applications*, 2014, pp. 1–2.

[52] O. F. Anjum, M. Guasoni, and P. Petropoulos, "All-optical control of spatial beam intensity in multimode fibers by polarization modulation," *To be submitted*, 2020.

[53] O. F. Anjum, M. Guasoni, P. Horak, Y. Jung, P. Petropoulos, D. J. Richardson, and F. Parmigiani, "Polarization insensitive four wave mixing based wavelength conversion in few-mode optical fibers," *Journal of Lightwave Technology*, vol. 36, no. 17, pp. 3678–3683, 2018.

[54] O. F. Anjum, P. Horak, Y. Jung, M. Suzuki, Y. Yamamoto, T. Hasegawa, P. Petropoulos, D. J. Richardson, and F. Parmigiani, "Bandwidth enhancement of inter-modal four wave mixing bragg scattering by means of dispersion engineering," *APL Photonics*, vol. 4, no. 2, p. 022 902, 2019.

[55] O. F. Anjum, M. Guasoni, P. Horak, Y. Jung, M. Suzuki, T. Hasegawa, K. Bottrill, D. J. Richardson, F. Parmigiani, and P. Petropoulos, "Selective wavelength conversion in a few-mode fiber," *Opt. Express*, vol. 27, no. 17, pp. 24 072–24 081, Aug. 2019.

[56] K. Okamoto, *Fundamentals of optical waveguides*. Academic press, 2006.

[57] C. R. Pollock, "Fundamentals of optoelectronics," 1995.

[58] L. Palmieri and A. Galtarossa, "Coupling effects among degenerate modes in multimode optical fibers," *IEEE Photonics Journal*, vol. 6, no. 6, pp. 1–8, 2014, ISSN: 1943-0655.

[59] A. A. Juarez, E. Krune, S. Warm, C. A. Bunge, and K. Petermann, "Modeling of mode coupling in multimode fibers with respect to bandwidth and loss," *Journal of lightwave technology*, vol. 32, no. 8, pp. 1549–1558, 2014.

[60] C. Antonelli, A. Mecozzi, M. Shtaif, and P. J. Winzer, "Modeling and performance metrics of mimo-sdm systems with different amplification schemes in the presence of mode-dependent loss," *Optics Express*, vol. 23, no. 3, pp. 2203–2219, 2015.

[61] M. B. Shemirani, W. Mao, R. A. Panicker, and J. M. Kahn, "Principal modes in graded-index multimode fiber in presence of spatial- and polarization-mode coupling," *Journal of Lightwave Technology*, vol. 27, no. 10, pp. 1248–1261, 2009.

[62] J. Carpenter, B. J. Eggleton, and J. Schröder, "Comparison of principal modes and spatial eigenmodes in multimode optical fibre," *Laser & Photonics Reviews*, vol. 11, no. 1, p. 1 600 259, 2017.

[63] M. Plöschner, T. Tyc, and T. Čižmár, "Seeing through chaos in multimode fibres," *Nature Photonics*, vol. 9, no. 8, p. 529, 2015.

[64] R. Brüning, D. Flamm, S. S. Ngcobo, A. Forbes, and M. Duparré, "Rapid measurement of the fiber's transmission matrix," in *Next-Generation Optical Communication: Components, Sub-Systems, and Systems IV*, International Society for Optics and Photonics, vol. 9389, 2015, 93890N.

[65] J. Carpenter, B. J. Eggleton, and J. Schröder, "110x110 optical mode transfer matrix inversion," *Optics express*, vol. 22, no. 1, pp. 96–101, 2014.

[66] W. Xiong, C. W. Hsu, Y. Bromberg, J. E. Antonio-Lopez, R. Amezcua Correa, and H. Cao, "Complete polarization control in multimode fibers with polarization and mode coupling," *Light: Science & Applications*, vol. 7, no. 1, p. 54, Aug. 2018, ISSN: 2047-7538.

[67] R. D. Niederriter, M. E. Siemens, and J. T. Gopinath, "Continuously tunable orbital angular momentum generation using a polarization-maintaining fiber," *Opt. Lett.*, vol. 41, no. 14, pp. 3213–3216, Jul. 2016.

[68] S. N. Khan, S. K. Chatterjee, and P. R. Chaudhuri, "Polarization and propagation characteristics of switchable first-order azimuthally asymmetric beam generated in dual-mode fiber," *Appl. Opt.*, vol. 54, no. 6, pp. 1528–1542, Feb. 2015.

[69] M. Guasoni, "Generalized modulational instability in multimode fibers: Wideband multimode parametric amplification," *Phys. Rev. A*, vol. 92, p. 033 849, 3 Sep. 2015.

[70] C. D. Poole and D. L. Favin, "Polarization-mode dispersion measurements based on transmission spectra through a polarizer," *Journal of Lightwave Technology*, vol. 12, no. 6, pp. 917–929, 1994.

[71] J. N. Damask, *Polarization optics in telecommunications*. Springer Science & Business Media, 2004.

[72] L. Grüner-Nielsen, Y. Sun, J. W. Nicholson, D. Jakobsen, K. G. Jespersen, R. Lingle Jr, and B. Pálsdóttir, "Few mode transmission fiber with low dgd, low mode coupling, and low loss," *Journal of Lightwave Technology*, vol. 30, no. 23, pp. 3693–3698, 2012.

[73] F. Parmigiani, Y. Jung, L. Grüner-Nielsen, T. Geisler, P. Petropoulos, and D. J. Richardson, "Elliptical core few mode fibers for multiple-input multiple output-free space division multiplexing transmission," *IEEE Photon. Technol. Lett.*, vol. 29, no. 21, pp. 1764–1767, 2017.

[74] J. Cheng, M. E. V. Pedersen, K. Wang, C. Xu, L. Grüner-Nielsen, and D. Jakobsen, "Time-domain multimode dispersion measurement in a higher-order-mode fiber," *Opt. Lett.*, vol. 37, no. 3, pp. 347–349, Feb. 2012.

[75] Y.-R. Shen, *The principles of nonlinear optics*. Wiley, 1984.

[76] P. E. Powers, *Fundamentals of Nonlinear Optics*. CRC Press, 2011.

[77] G. Agrawal, *Nonlinear Fiber Optics*, 5th. John Wiley & Sons, 2013.

[78] R. W. Boyd, *Nonlinear optics*. Academic press, 2019.

[79] L. Rishøj, "Four wave mixing using intermodal nonlinearities," Ph.D. dissertation, Citeseer, 2012.

[80] A. Trichili, M. Zghal, L. Palmieri, and M. Santagiustina, "Phase-sensitive mode conversion and equalization in a few mode fiber through parametric interactions," *IEEE Photonics Journal*, vol. 9, no. 1, pp. 1–10, 2016.

[81] S. M. M. Friis, I. Begleris, Y. Jung, K. Rottwitt, P. Petropoulos, D. J. Richardson, P. Horak, and F. Parmigiani, "Inter-modal four-wave mixing study in a two-mode fiber," *Opt. Express*, vol. 24, no. 26, pp. 30 338–30 349, Dec. 2016.

[82] Y. Xiao, R.-J. Essiambre, M. Desgroseilliers, A. M. Tulino, R. Ryf, S. Mumtaz, and G. P. Agrawal, "Theory of intermodal four-wave mixing with random linear mode coupling in few-mode fibers," *Optics express*, vol. 22, no. 26, pp. 32 039–32 059, 2014.

[83] J. Laegsgaard, "Mode profile dispersion in the generalized nonlinear schrödinger equation," *Optics express*, vol. 15, no. 24, pp. 16 110–16 123, 2007.

[84] S. Mumtaz, R.-J. Essiambre, and G. P. Agrawal, "Nonlinear propagation in multimode and multicore fibers: Generalization of the manakov equations," *J. Lightwave Technol.*, vol. 31, no. 3, pp. 398–406, Feb. 2013.

[85] C. J. McKinstrie, J. D. Harvey, S. Radic, and M. G. Raymer, "Translation of quantum states by four-wave mixing in fibers," *Opt. Express*, vol. 13, no. 22, pp. 9131–9142, Oct. 2005.

[86] M. Esmaeelpour, R.-J. Essiambre, N. K. Fontaine, R. Ryf, J. Toulouse, Y. Sun, and R. Lingle, "Power fluctuations of intermodal four-wave mixing in few-mode fibers," *J. Lightwave Technol.*, vol. 35, no. 12, pp. 2429–2435, Jun. 2017.

[87] M. Guasoni, F. Parmigiani, P. Horak, J. Fatome, and D. J. Richardson, "Intermodal four-wave-mixing and parametric amplification in km-long multi-mode fibers," *Journal of Lightwave Technology*, vol. 35, no. 24, pp. 5296–5305, 2017.

[88] C. R. Menyuk and P. Wai, "Polarization evolution and dispersion in fibers with spatially varying birefringence," *JOSA B*, vol. 11, no. 7, pp. 1288–1296, 1994.

[89] I. Kaminow and T. Li, *Optical fiber telecommunications IV-B: systems and impairments*. Elsevier, 2002, vol. 2.

[90] F. Poletti and P. Horak, "Description of ultrashort pulse propagation in multimode optical fibers," *J. Opt. Soc. Am. B*, vol. 25, no. 10, pp. 1645–1654, Oct. 2008.

[91] S. Mumtaz, R. J. Essiambre, and G. P. Agrawal, "Birefringence effects in space-division multiplexed fiber transmission systems: Generalization of manakov equation," in *2012 IEEE Photonics Society Summer Topical Meeting Series*, Jul. 2012, pp. 179–180.

[92] C. J. McKinstrie, S. Radic, and A. R. Chraplyvy, "Parametric amplifiers driven by two pump waves," *IEEE Journal of Selected Topics in Quantum Electronics*, vol. 8, no. 3, pp. 538–547, May 2002, ISSN: 1077-260X.

[93] B. A. Bell, C. Xiong, D. Marpaung, C. J. McKinstrie, and B. J. Eggleton, "Uni-directional wavelength conversion in silicon using four-wave mixing driven by cross-polarized pumps," *Opt. Lett.*, vol. 42, no. 9, pp. 1668–1671, May 2017.

[94] C. Lacava, T. D. Bucio, A. Z. Khokhar, P. Horak, Y. Jung, F. Y. Gardes, D. J. Richardson, P. Petropoulos, and F. Parmigiani, "Intermodal frequency generation in silicon-rich silicon nitride waveguides," *Photon. Res.*, vol. 7, no. 6, pp. 615–621, Jun. 2019.

[95] V. Torres-Company, C. J. Krückel, A. Fülöp, and P. A. Andrekson, "Silicon-rich nitride waveguides for broadband nonlinear signal processing," in *2017 Conference on Lasers and Electro-Optics Pacific Rim (CLEO-PR)*, 2017, pp. 1–3.

[96] C. Lacava, S. Stankovic, A. Z. Khokhar, T. D. Bucio, F. Gardes, G. T. Reed, D. J. Richardson, and P. Petropoulos, "Si-rich silicon nitride for nonlinear signal processing applications," *Scientific reports*, vol. 7, no. 1, pp. 1–13, 2017.

[97] G. Rademacher, R. Ryf, N. K. Fontaine, H. Chen, R. M. Jopson, R. Essiambre, B. J. Puttnam, R. S. Luís, Y. Awaji, N. Wada, S. Gross, N. Riesen, M. Withford, Y. Sun, and R. Lingle, "Experimental investigation of parametric mode and wavelength conversion in a 4.7 km few-mode fiber," in *2018 European Conference on Optical Communication (ECOC)*, Sep. 2018.

[98] M. Hirano, T. Nakanishi, T. Okuno, and M. Onishi, "Selective fwm-based wavelength conversion realized by highly nonlinear fiber," in *2006 European Conference on Optical Communications*, Sep. 2006, pp. 1–2.

[99] T. Torounidis, H. Sunnerud, P. O. Hedekvist, and P. A. Andrekson, "Amplification of wdm signals in fiber-based optical parametric amplifiers," *IEEE Photonics Technology Letters*, vol. 15, no. 8, pp. 1061–1063, 2003.

[100] M. Grayson, M. Zohrabi, K. Bae, J. Zhu, J. T. Gopinath, and W. Park, "Enhancement of third-order nonlinearity of thermally evaporated gesbse waveguides through annealing," *Optics Express*, vol. 27, no. 23, pp. 33 606–33 620, 2019.

[101] B. Qiao, S. Dai, Y. Xu, P. Zhang, X. Shen, T. Xu, Q. Nie, W. Ji, and F. Chen, "Third-order optical nonlinearities of chalcogenide glasses within ge-sn-se ternary system at a mid-infrared window," *Optical Materials Express*, vol. 5, no. 10, pp. 2359–2365, 2015.

[102] B. J. Eggleton, B. Luther-Davies, and K. Richardson, "Chalcogenide photonics," *Nature photonics*, vol. 5, no. 3, p. 141, 2011.

[103] S. Signorini, M. Finazzer, M. Bernard, M. Ghulinyan, G. Pucker, and L. Pavesi, "Silicon photonics chip for inter-modal four wave mixing on a broad wavelength range," *Frontiers in Physics*, vol. 7, p. 128, 2019.